Search and discovery with the resonant $\gamma\gamma$ final state at ATLAS

by

Andrew Straiton Hard

A dissertation submitted in partial fulfillment

of the requirements for the degree of

Doctor of Philosophy

(Physics)

at the

University of Wisconsin–Madison

2016

CERN-THESIS-2016-200
02/12/2016

Date of final oral examination: December 2, 2016

The dissertation is approved by the following members of the Final Oral Committee:

Yang Bai, Assistant Professor, Physics

Sridhara Dasu, Professor, Physics

Lisa Everett, Professor, Physics

Michael Winokur, Professor, Physics

Sau Lau Wu, Professor, Physics

© Copyright by Andrew Hard 2016

All Rights Reserved

For those whom I love.

Acknowledgments

Above all others, I must thank Deb and Straiton for giving me life. I think that has worked out brilliantly. I am indebted to you and to my amazing step-parents, Deirdre and Jim, for a wonderful upbringing. I was not always the easy-going, charming person I am today, and I really appreciate the love you have shown me.

I am full of gratitude and respect for my advisor, Sau Lan Wu. She recruited me for the University of Wisconsin ATLAS Group to search for the Higgs boson. Sau Lan inspired me to be a better researcher and always reminded me of my debt to society. I always knew she had the best interests of her students and the group in mind.

Mariana, you have enriched my life and have made me happy. Hope for a future with you has motivated me to graduate. I'm thrilled and nervous about finding out what happens next in our adventure!

Thank you to all of my friends and colleagues at CERN, particularly Chris Meyer, Sam Meehan, Haichen Wang, Hongtao Yang, Laser Kaplan, and Xiangyang Ju. Graduate student life can be lonely, but I was fortunate to be surrounded by intelligent and funny people. Some of them were even both!

In order to avoid an acknowledgment section as long as the ATLAS author list, I will conclude by thanking Jim Pilcher, Junichi Tanaka, Marc Escalier, John Parsons, Maurice Garcia-Sciveres, Ed Blucher, Celeste Shibata, and Ben Szapiro. Each of them assisted me during a critical step in my scientific career.

My labor and my identity are reflections of the people in my life. Everyone has contributed something to this effort. For the 99% of you who were not explicitly mentioned, please forgive me! I'm rushing to make a deadline.

Contents

List of Tables

List of Figures

Search and discovery with the resonant $\gamma\gamma$ final state at ATLAS

Andrew Straiton Hard

Under the supervision of Professor Sau Lan Wu

At the University of Wisconsin–Madison

Abstract

A search for the Standard Model Higgs boson was conducted with the ATLAS Experiment at the LHC using the two-photon decay channel. Datasets with integrated luminosities of 4.8 fb^{-1} and 5.9 fb^{-1} were collected in 2011 and 2012 for pp collisions with center-of-mass energies of $\sqrt{s} = 7$ TeV and 8 TeV, respectively. A statistically significant excess of events above the background-only expectation in the $\gamma\gamma$ decay channel of 4.5 standard deviations was observed. Combined with excesses in the WW^* and ZZ^* decays, this observation led to the discovery of a Higgs boson with a significance of 5.9 standard deviations at a mass of 126.0 ± 0.4 (stat) ± 0.4 (sys) GeV.

Searches for diphoton resonances during 2015 and 2016 with LHC data were motivated by extensions to the Standard Model that predict additional scalar particles. Data were analyzed from $\sqrt{s} = 13$ TeV pp collisions, corresponding to an integrated luminosity of 15.4 fb^{-1}, and no significant deviations from the Standard Model hypothesis were observed. 95% CL limits on the production cross-section times branching ratio to $\gamma\gamma$ were calculated for scalar models with masses between 200 GeV and 2.4 TeV and widths ranging from 4 MeV to 10% of the scalar mass.

Chapter 1

Introduction

The Standard Model (SM) of particle physics provides an experimentally tested framework for describing high-energy particle interactions [3–6]. The Englert-Brout-Higgs mechanism, which was introduced into the theory order to accommodate massive $W^{\pm}$ and Z gauge bosons, predicts the existence of a massive scalar boson - the Higgs particle [7–12]. While many properties of the scalar are well defined by theory, including the couplings and decay rates, the mass m_H is unconstrained in the model. The task of searching for the Higgs boson and excluding possible Higgs boson masses occupied experimentalist physicists for decades.

Direct and indirect experimental searches for the Higgs boson were conducted using the Large Electron Positron (LEP) e^+e^- collider at CERN and the Tevatron $p\bar{p}$ collider at Fermilab prior to the start of the Large Hadron Collider (LHC) physics program. Though neither found evidence for the particle, each managed to constrain the range of possible values of m_H. The LEP Experiments, including ALEPH, DELPHI, L3, and OPAL, used data from center-of-mass energies between 189 GeV and 209 GeV to rule out the existence of Standard Model Higgs bosons with masses below

$m_H = 114.4$ GeV at 95% confidence level (CL) [13]. Direct searches with the CDF and D0 detectors at the Tevatron with center-of-mass collision energies of $\sqrt{s} = 1.96$ TeV were also used to exclude the higher-mass range 162 GeV $\leq m_H \leq$ 166 GeV at the 95% CL [14]. Additionally, indirect experimental limits on m_H were made using measurements of electroweak parameters that, due to radiative corrections, depend logarithmically on m_H [15]. A best-fit mass of $m_H = 89^{+35}_{-26}$ GeV was found, and a 95% CL upper bound of 158 GeV was set on the Standard Model Higgs boson mass.

The Large Hadron Collider (LHC) [16] was constructed at CERN for the purpose of elucidating the electroweak symmetry-breaking mechanism, among other phenomena. The 27 km circumference circular machine was designed to accelerate two beams of protons in opposite directions at energies of 7 TeV for the purpose of producing pp collisions at a center-of-mass energy of $\sqrt{s} = 14$ TeV with an instantaneous luminosity of 10^{34} cm^{-2}s^{-1}. Two multipurpose particle detectors, ATLAS [1] and CMS [17], surround intersection points of the two LHC beams and record momentum and energy measurements for reconstructed decay products of pp collisions. Each was designed with discovery or exclusion of the Englert-Brout-Higgs hypothesis in mind.

The first analysis presented is the search for the Standard Model Higgs boson in the resonant $\gamma\gamma$ final state with ATLAS [18]. The analysis was performed using a 4.8 fb^{-1} integrated luminosity dataset collected with $\sqrt{s} = 7$ TeV along with a 5.9 fb^{-1} integrated luminosity dataset collected with $\sqrt{s} = 8$ TeV. An excess of events above the background-only expectation was observed for a hypothesized Higgs boson mass of approximately $m_H = 126.5$ GeV with a statistical significance of 4.5 standard deviations. When combined with the $H \to ZZ^* \to 4l$ and $H \to WW^* \to l\nu l\nu$ channels, the statistical significance of the observation reached 5.9 standard deviations.

A discovery was announced by ATLAS and CMS jointly in July, 2012 [19, 20].

The discovery of the Higgs boson initiated a number of measurements of the new particle's properties, including its mass [21], spin [22], and production and decay rates [23], using the full $\sqrt{s} = 7$ TeV and $\sqrt{s} = 8$ TeV datasets. These measurements have been continued with the $\sqrt{s} = 13$ TeV dataset, and have been in excellent agreement with the Standard Model predictions to date. At the same time, numerous theoretical extensions to the Standard Model have motivated new searches for additional scalar particles [24–30].

The second analysis presented in this dissertation is the search for new scalar particles with the resonant high-mass diphoton final state with ATLAS. The search benefitted from the upgraded $\sqrt{s} = 13$ TeV center-of-mass energy of the LHC in Run 2, which boosted theoretical signal cross-sections significantly with respect to $\sqrt{s} = 8$ TeV. With a 15.4 fb^{-1} integrated luminosity dataset collected during 2015 and the first half of 2016, no statistically significant evidence for additional scalar states was found. The observations were used to set limits on the production cross-section times branching ratio to $\gamma\gamma$ for scalar particles with masses between 200 GeV and 2.4 TeV. A version of this analysis with 2015 data was published by the ATLAS Collaboration in June, 2016 [31], and an update with the first 12.2 fb^{-1} of 2016 data was presented at the 2016 ICHEP Conference [32].

This dissertation describes the methodology and results of the search and discovery of the Higgs boson in Run I of the LHC (between 2010 and 2012), as well as the search for high-mass diphoton resonances during the start of LHC Run II (including 2015 and the first half of 2016). The analyses use similar strategies and are described in parallel throughout the text. Chapter 2 introduces the theoretical moti-

vation for each search and describes the Higgs boson phenomenology. The components of the ATLAS Experiment are described in Chapter 3. The collision data samples and Monte Carlo simulations used to construct and optimize the analyses are the subject of Chapter 4. Reconstruction algorithms for photons and jets are described in Chapter 5. The selection of collision events containing two photons is covered in Chapter 6. Modeling strategies for the signal and background are discussed in Chapter 7. The likelihood model and statistical tests used to quantify agreement between data and hypotheses are described in Chapter 8. A discussion of the experimental results is provided in Chapter 9, while some concluding thoughts are given in Chapter 10. Finally, Appendix A discusses methods that were developed for measuring the global significance of a deviation from the background-only hypothesis in a search over a large, multi-dimensional signal space.

Chapter 2

Theory

2.1 The Standard Model

The Standard Model of particle physics is a mathematical framework that describes the interactions of elementary particles at high energies through the strong, weak, and electromagnetic forces. Spin-$\frac{1}{2}$ elementary particles comprise the visible matter in the universe. These fermions include the charged leptons (e, μ, τ), the corresponding neutral neutrinos (ν_e, ν_μ, ν_τ), the quarks (u, d, c, s, t, b), and the antiparticles of each of the leptons and quarks. Interactions between the particles are mediated by spin-1 gauge bosons: the γ, $W^{\pm}$, and Z bosons for the electroweak force, and the gluons g for the strong force. A summary of the Standard Model particle content is provided in Figure 2.1 [33].

The Standard Model is a renormalizable [6], locally invariant gauge theory [34] based on an $SU(3)_C \otimes SU(2)_L \otimes U(1)_Y$ symmetry group. Work by Glashow [3], Weinberg [4], and Salam [5] during the 1960s led to the unification of the electromagnetic and weak forces in a local gauge theory of electroweak interactions based on the

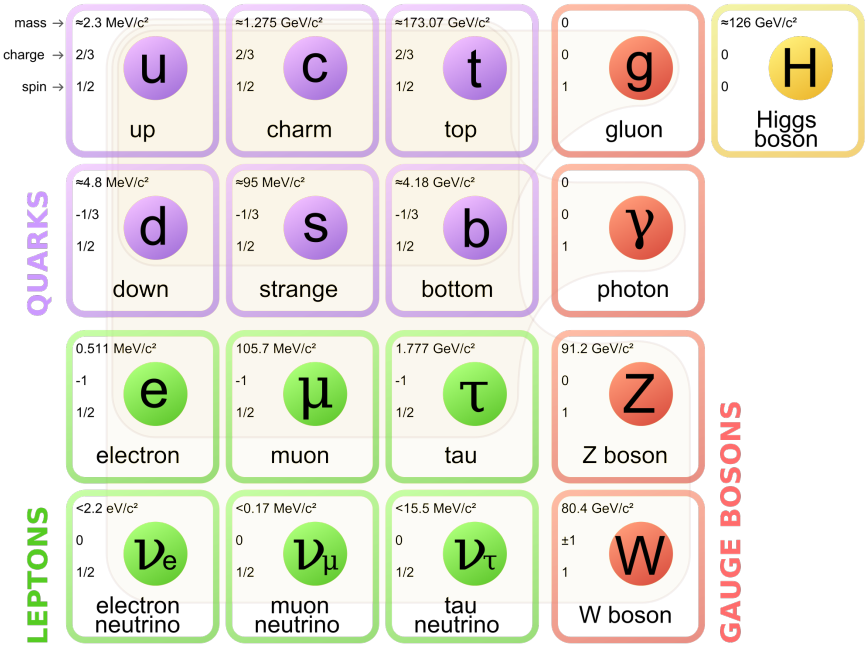

Figure 2.1: The particle content of the Standard Model, including the fermions (quarks and leptons), the gauge bosons, and the Higgs boson.

$SU(2)_L \otimes U(1)_Y$ symmetry group. The quantum chromodynamics (QCD) model of the strong force was also developed during that time based on the $SU(3)_C$ symmetry group [35,36]. The 8 generators of this group correspond to the 8 color quantum states of the gluon.

The GWS electroweak theory predicts the existence of massive, charged vector boson mediators for the weak interaction (the $W^{\pm}$), along with a neutral weak boson (Z^0). Data from weak interactions such as beta decays had previously hinted at the existence of a massive charged vector boson like the $W^{\pm}$ [37,38]. The extremely short range of weak interactions also suggested that the W and Z should be massive. Strong experimental support for the electroweak model was provided by the discoveries of the $W^{\pm}$ [39,40] and Z boson [41,42] in 1983 using the Super Proton Synchrotron at CERN.

2.2 The Higgs Mechanism

The Higgs mechanism solves a problem posed by the massive weak gauge bosons. Naive mass terms for the W and Z of the form $\frac{1}{2}M^2 W_\mu W^\mu$ end up violating the gauge invariance of the Lagrangian. Research into the spontaneous symmetry-breaking of a global symmetry hinted at a solution. A symmetry breaking mechanism could generate weak boson masses, but it also generated (unobserved) mass-less Goldstone bosons [43–45].

Starting in 1964, a series of papers by Brout and Englert [7], Higgs [8–10], and others [11, 12], demonstrated that spontaneous symmetry breaking of a *local* gauge symmetry could explain the massive bosons. In the simplest case, the Lagrangian is extended by adding a scalar field $\phi \equiv \begin{pmatrix} \phi^+ \\ \phi^0 \end{pmatrix}$ via a complex $SU(2)$ doublet with 4 degrees of freedom and a potential energy term $V(\phi)$:

$$V(\phi) = \mu^2 \phi^\dagger \phi + \frac{\lambda}{2}(\phi^\dagger \phi)^2. \tag{2.1}$$

When $\mu^2 < 0$ and $\lambda > 0$, spontaneous symmetry breaking leads to a vacuum expectation value for ϕ: $v = \sqrt{2}|\mu|/\lambda = 2M_W/g$. The vacuum expectation value is related to the mass of the W boson and the weak gauge coupling g, and has been measured experimentally to be $v \approx 246$ GeV [46].

The symmetry breaking $SU(2)_L \otimes U(1)_Y \to U(1)_{EM}$ creates one massive boson – the Higgs particle – and three mass-less Goldstone bosons that are absorbed by the longitudinal polarizations of the $W^\pm$ and Z bosons. The model provides a mass-less description of the γ, preserves the renormalizability of the theory, and preserves the Lagrangian's gauge symmetry. Masses for the fermions can also be generated by

Vertex	Coupling Strength
$Hf\bar{f}$	M_f/v
HW^+W^-	$2M_W^2/v$
HZ^0Z^0	M_Z^2/v
HHW^+W^-	M_W^2/v^2
HHZ^0Z^0	$M_Z^2/2v^2$
HHH	$M_H^2/2v$
$HHHH$	$M_H^2/8v^2$

Table 2.1: Higgs boson couplings to fermions (f), gauge bosons (W,Z), and self (H).

the electroweak symmetry-breaking (EWSB) mechanism through Yukawa interactions with the Higgs field.

The Higgs boson mass, $m_H = \lambda v$, is a free parameter in the Higgs mechanism. Once it is known, the entire phenomenological profile of the particle, including production cross-sections and decay branching ratios, is determined by the theory. Table 2.1 lists the couplings of the Higgs boson to the Standard Model particles.

2.3 SM Higgs boson production at the LHC

There are four dominant production modes for the SM Higgs boson at the LHC: gluon fusion (ggH), vector boson fusion (VBF), associated production with vector bosons (WH and ZH), and production in association with top quarks ($t\bar{t}H$). The cross-sections for these production modes as a function of m_H are shown in Figures 2.2a and 2.2b for pp center-of-mass energies of $\sqrt{s} = 7$ TeV and $\sqrt{s} = 8$ TeV, respectively [47–50]. Cross-section calculations for the ggH, VBF, VH, and $t\bar{t}H$ Higgs production modes are summarized in Table 2.2, assuming a Higgs boson mass of 125 GeV [50]. The total cross-section for the Higgs boson at that mass was also calculated to be 17.5 pb for pp collisions at $\sqrt{s} = 7$ TeV, and 22.3 pb for collisions at $\sqrt{s} = 8$ TeV [47, 48].

Process	**Cross-section [pb]**	
	$\sqrt{s} = 7$ TeV	$\sqrt{s} = 8$ TeV
ggH	15.3 ± 2.3	19.5 ± 2.9
VBF	1.21 ± 0.032	1.55 ± 0.043
WH	0.573 ± 0.025	0.697 ± 0.029
ZH	0.316 ± 0.016	0.394 ± 0.020
$t\bar{t}H$	0.0863 ± 0.015	0.130 ± 0.022
Total	17.5 ± 2.4	22.3 ± 3.0

Table 2.2: Cross-sections for the dominant production modes of the SM Higgs boson for various LHC center-of-mass energies, assuming $m_H = 125$ GeV. QCD scale and PDF+α_s uncertainties are added in quadrature.

Gluon fusion is the largest production mechanism for Higgs bosons at the LHC, as a result of the fact that the LHC is primarily a gluon collider [51]. Gluons are mass-less and do not couple directly to the Higgs, so the generation of a Higgs boson proceeds through a loop containing massive particles with color charge (such as the b and t). The largest contribution to the ggH cross-section comes from the t-quark loop in the Standard Model. Figure 2.3a shows the leading-order (LO) Feynman diagram for the ggH process [47]. The ggH cross-section was calculated with next-to-next-to-leading-order (NNLO) QCD corrections [52–58] and next-to-leading-order (NLO) EW corrections [59, 60]. The gluon fusion process is sensitive to soft QCD radiation, and QCD soft-gluon resummations were calculated at next-to-next-to-leading-log order (NNLL) [61]. The complete cross-section calculation is described in References [62–65].

Vector boson fusion is the second most prominent Higgs production mode at the LHC. A Feynman diagram for VBF at LO in the t-channel is shown in Figure 2.3b. For the VBF production cross-section calculation, QCD and EW corrections were calculated up to NLO [66–69]. NNLO QCD correction approximations [70] were also

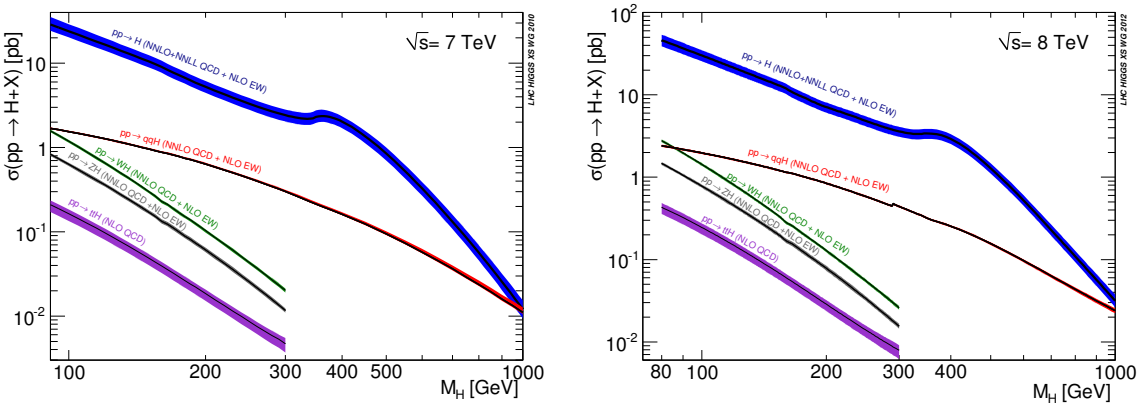

(a) $\sqrt{s} = 7$ TeV (b) $\sqrt{s} = 8$ TeV

Figure 2.2: Cross-sections for dominant production modes and branching ratios of the Standard Model Higgs boson as a function of Higgs mass.

used to calculate the cross-section. Two forward quark jets in the final state provide a useful signature for *VBF* identification. Since the Higgs directly couples to the W and Z in *VBF*, evidence for this process would confirm the role of the Higgs in EWSB.

Standard Model Higgs bosons can also be produced at the LHC in association with vector bosons. Associated production of a W boson and a Higgs proceeds from $q\bar{q}'$ annihilation (Figure 2.4a), while associated production of a Z and a Higgs boson can proceed through $q\bar{q}'$ and gg collisions (Figures 2.4a, 2.4b, and 2.4c). The associated production cross-sections were calculated with NNLO QCD corrections [71–73] and NLO EW corrections [74].

The presence of a W or Z in the event also provides useful information that can be used for event selection. For instance, two quark jets can be used to identify *VH* events where the W or Z decay hadronically. A dilepton requirement can select for leptonic *ZH* decays, while a lepton and E_T^{miss} requirement can be used to find leptonic *WH* events.

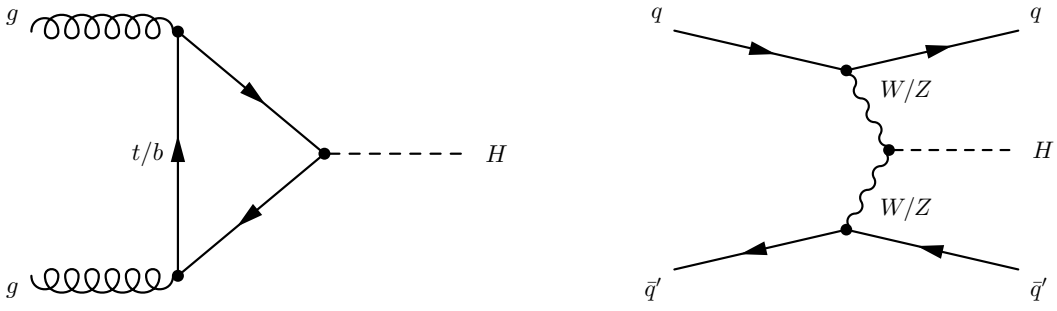

(a) $gg \to H$ (b) $q\bar{q} \to q\bar{q}H$

Figure 2.3: Example Feynman diagrams for the production of a Higgs boson through gluon fusion (2.3a) and vector boson fusion (2.3b) at leading-order.

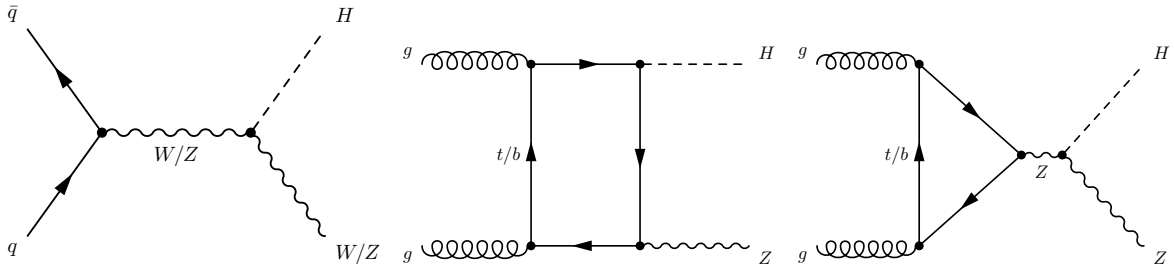

(a) $q\bar{q} \to WH, ZH$ (b) $gg \to ZH$ (c) $gg \to ZH$

Figure 2.4: Example Feynman diagrams for Higgs boson production associated with a vector boson at leading-order (2.4a), and at NLO for $gg \to ZH$ (2.4b and 2.4c).

As a result of the Yukawa coupling between the Higgs boson and fermions, the SM Higgs boson can also be produced in association with top quarks. Figure 2.5 shows the Feynman diagrams at LO for the production of a Higgs boson in association with a top quark ($gg \to t\bar{t}H$ process). The $t\bar{t}H$ process cross-section was estimated to NLO in QCD [75–79].

There is also interference between the Higgs production process $gg \to H \to \gamma\gamma$ and the continuum background $gg \to \gamma\gamma$ process [80]. The interference is destructive, and is on the order of 5% of the cross-section times branching ratio for $H \to \gamma\gamma$.

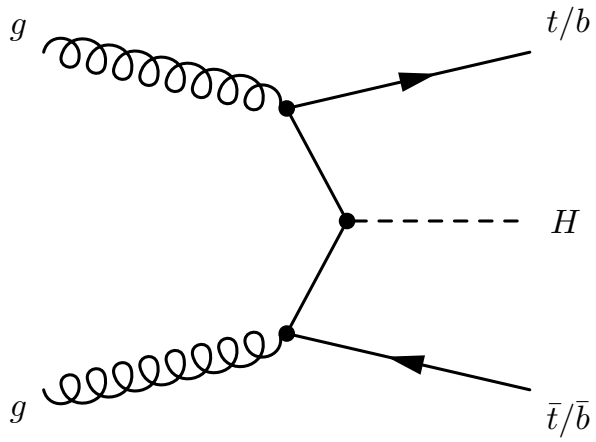

Figure 2.5: Example Feynman diagram at LO for the $gg \to t\bar{t}H, b\bar{b}H$ production of the SM Higgs boson.

2.4 Decays of the SM Higgs boson

The total width, as well as the branching fractions for the decay of the Standard Model Higgs boson are shown as a function of m_H in Figures 2.6a and 2.6b. Example branching fractions are also provided in Table 2.3 for a Higgs mass of 125 GeV [49]. Branching fractions for the Standard Model Higgs boson were calculated as a function of m_H using HDECAY [81]. Figures 2.7a and 2.7b show the leading order Feynman diagrams for Higgs decays to vector boson or fermion pairs.

The $b\bar{b}$ decay mode would be dominant for a low-mass Higgs (e.g. $m_H = 125$ GeV), where the WW, ZZ, and $t\bar{t}$ decays are off-shell. The WW and ZZ modes would account for the majority of Higgs decays for large masses ($m_H > 2m_V$). This would even be true after $H \to t\bar{t}$ is on-shell, as a result of the fact that $\Gamma(H \to VV) \propto m_H^3$ while $\Gamma(H \to f\bar{f}) \propto m_H$ [82–84]. Decays of the Higgs boson to quark pairs are enhanced by a factor of three with respect to lepton pairs due to the color quantum number, while decays to W boson pairs are enhanced by a factor of two with respect

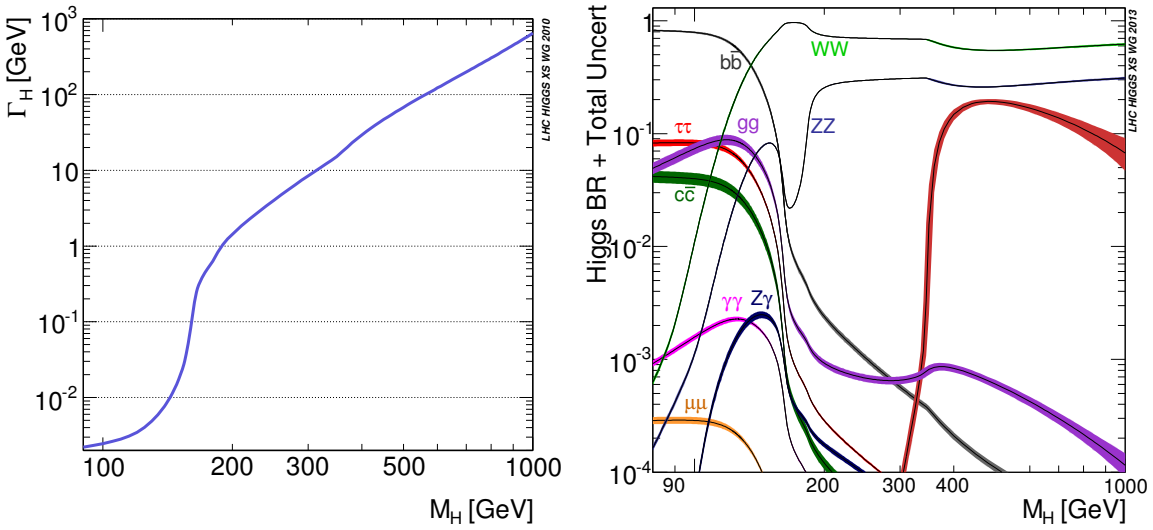

(a) (b)

Figure 2.6: The total width (2.6a) and the decay branching fractions (2.6b) for the Standard Model Higgs boson as a function of m_H.

to Z boson pairs as a result of the electromagnetic charge quantum number [82].

Despite the fact that the γ and g are mass-less, $H \to \gamma\gamma$, $H \to Z\gamma$, and $H \to gg$ are decay paths for the Higgs boson. As shown in Figure 2.8, the $\gamma\gamma$ and $Z\gamma$ decays are made possible by loop diagrams containing massive charged particles like $W^{\pm}$, b, and t. The W loop provides the single largest contribution to the diphoton decay rate in the SM. The gg decay mode is also enabled by loops that contain massive particles with color charge. These loop diagrams are sensitive to the existence of new charged, massive particles. Measurements of the $\gamma\gamma$ decay rate are therefore useful probes of physics beyond the Standard Model (BSM).

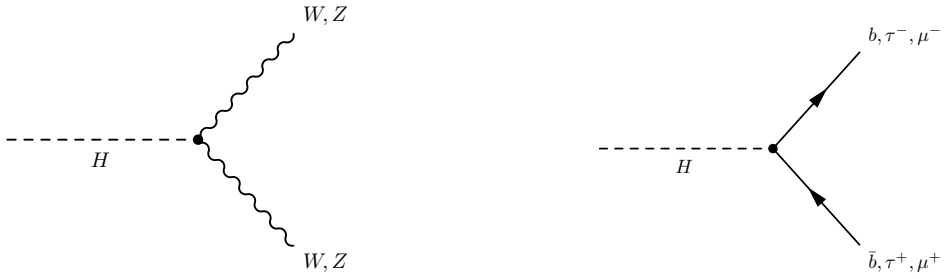

(a) $H \to VV$ (b) $H \to f\bar{f}$

Figure 2.7: Feynman diagrams for the decay of a Higgs boson to a pair of vector bosons (2.7a) or a pair of fermions (2.7b).

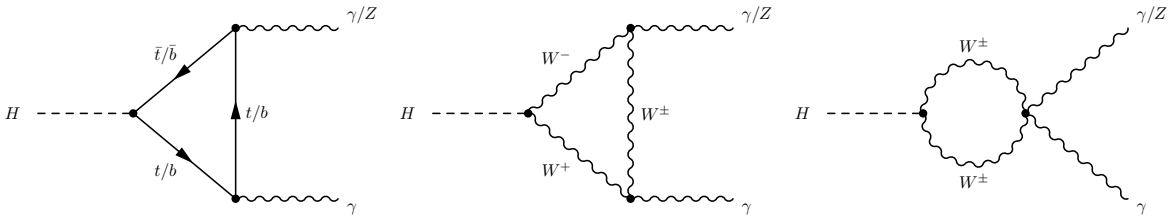

Figure 2.8: Feynman diagrams at LO for the decay of a Higgs boson to $\gamma\gamma$ and $Z\gamma$.

2.5 Extensions to the Standard Model

The Standard Model is an incomplete theory. Dark Matter, inflation, and gravity are just a few examples of observed phenomena which are not described by the model and lack field-theory descriptions. Many extensions to the Standard Model have been proposed to explain these phenomena. Some of the models predict additional scalar particles like the Higgs, including new heavy scalar singlets [24, 25, 29], hidden sector models [26–28], and spontaneous T-violation models [30].

2.6 Standard Model background processes

Several Standard Model processes that do not involve the Higgs boson can produce photon pairs from pp collisions at the LHC. They are referred to as *irreducible*

Decay	**Branching fraction** [%]
$b\bar{b}$	57.7 ± 1.9
WW^*	21.5 ± 0.9
gg	8.57 ± 0.87
$\tau^+\tau^-$	6.32 ± 0.36
$c\bar{c}$	2.91 ± 0.35
ZZ^*	2.64 ± 0.11
$\gamma\gamma$	0.228 ± 0.011
$Z\gamma$	0.154 ± 0.014
$\mu^+\mu^-$	0.0219 ± 0.0013

Table 2.3: Prominent branching fractions and uncertainties for the Standard Model Higgs boson, assuming $m_H = 125$ GeV.

backgrounds, due to the fact that they contain true photons and cannot be excluded from the data sample using photon-identification criteria.

Diphoton events are produced via the Born process $q\bar{q} \to \gamma\gamma$, as shown in Figure 2.9, with NLO contributions in α_s (the QCD coupling) from the $q\bar{q} \to \gamma\gamma g$ and $gq \to \gamma\gamma q$ (Bremsstrahlung) subprocesses [85]. Diphoton production in which one or two photons are produced by quark fragmentation are also significant contributions (Figures 2.10 and 2.11, respectively). Despite being NNLO, the "Box" diphoton process is also prominent at the LHC because of the large gg luminosity relative to $q\bar{q}$. The $\mathcal{O}(\alpha_s^2)$ Feynman diagram for the Box process is shown in Figure 2.12 [85]. Recently, a full NNLO calculation for diphoton production at the LHC has become available [86].

Standard Model processes involving single photons and jets or multiple jets are also relevant to searches for $\gamma\gamma$ resonances. They are referred to as *reducible* backgrounds, because they can be excluded from the final data sample by optimizing the γ selection criteria. Nevertheless, there will always be some contamination from these

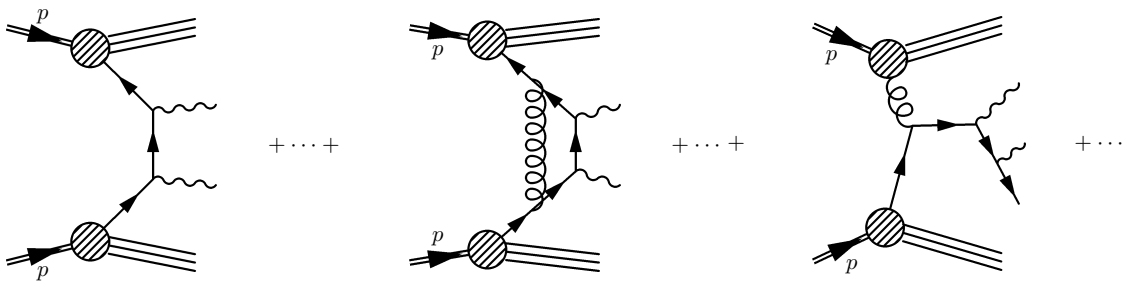

Figure 2.9: Feynman diagrams for the LO contribution to diphoton processes from the Born process $q\bar{q} \to \gamma\gamma$, and NLO contributions from the subprocesses $q\bar{q} \to \gamma\gamma g$, $gq \to \gamma\gamma q$, and associated virtual corrections.

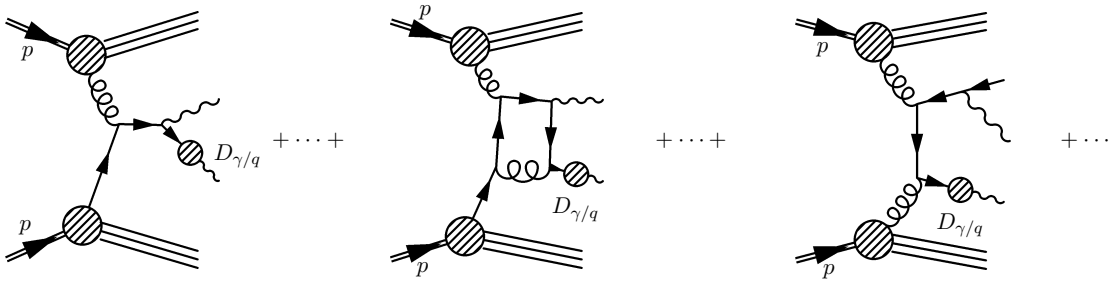

Figure 2.10: Feynman diagrams for diphoton production in which one of the photons is produced through quark fragmentation.

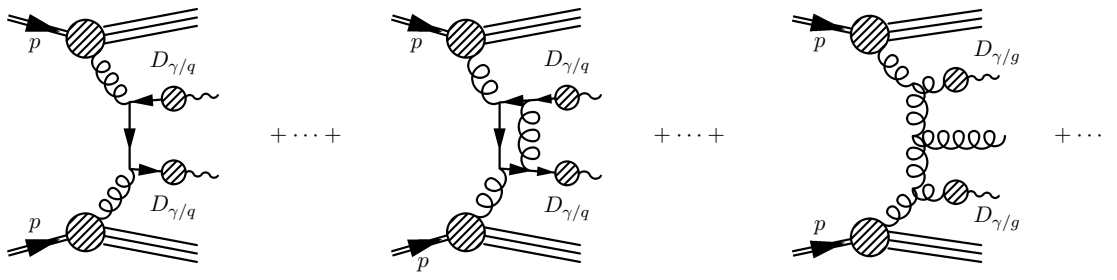

Figure 2.11: Feynman diagrams for diphoton production processes in which both photons are produced through quark fragmentation.

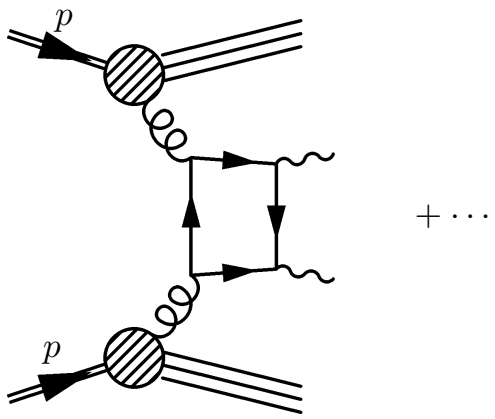

Figure 2.12: Feynman diagram for the $\gamma\gamma$ "Box" production process at $\mathcal{O}(\alpha_s^2)$.

"fake" photon backgrounds. Drell-Yan, $W\gamma$, $Z\gamma$, and other SM processes also have a negligible impact on diphoton searches, and only become prominent when events are categorized in order to select particular event topologies.

The cross-sections of the dominant $\gamma\gamma$, γ-jet, and multi-jet processes are provided in Table 2.4. The $\gamma\gamma$ cross-section is calculated by DIPHOX [85, 87, 88] at NLO and includes contributions from the Born and Box processes. PYTHIA [89] is used to compute the γ-jet and multi-jet cross-sections at LO.

A comparison of Tables 2.2 and 2.4 shows that cross-sections for the background processes are several orders of magnitude larger than that for Higgs boson production and decay to $\gamma\gamma$. The search would not be feasible except for the fact that the backgrounds are non-resonant whereas the signal is resonant. A detector with excellent energy resolution for electromagnetic radiation and the ability to discriminate between true photons and jets is necessary for this search.

Process	**Cross-section [pb]**	
	$\sqrt{s} = 8$ TeV	$\sqrt{s} = 14$ TeV
$\gamma\gamma$	12.13	21.72
γ+jet	4.4×10^4	8.9×10^4
multi-jet	1.5×10^8	3.7×10^8

Table 2.4: Example cross-sections for the $\gamma\gamma$, γ-jet, and multi-jet Standard Model processes at the LHC for *pp* center-of-mass collision energies of 8 TeV and 14 TeV. The Born and Box processes contribute to the $\gamma\gamma$ cross section as calculated by DIPHOX at NLO. PYTHIA is used to calculate the γ-jet and multi-jet cross-sections at LO.

Chapter 3

ATLAS Experiment

3.1 Introduction

This section describes the design of the ATLAS Experiment (A Toroidal Lhc ApparatuS) [1]. As illustrated in Figure 3.1, ATLAS is a multi-purpose particle detector with a cylindrical geometry and forward-backward symmetry that surrounds one of the collision points for the LHC [16] with solid angle coverage near 4π. The coordinate system used by ATLAS is right-handed with the origin at the nominal LHC beam interaction point at the center of the detector. The z-axis is tangential to the beam pipe at the interaction point, the x-axis points from the interaction point towards the center of the LHC ring, and the y-axis points vertically. In the transverse plane, cylindrical (r, ϕ) coordinates are used in which ϕ is the azimuthal angle around the beam pipe. The pseudo-rapidity is often used instead of the polar angle θ, and is defined as $\eta = -\ln(\tan(\theta/2))$.

ATLAS is composed of multiple sub-systems including superconducting magnets that bend charged particle tracks and assist in particle identification, tracking

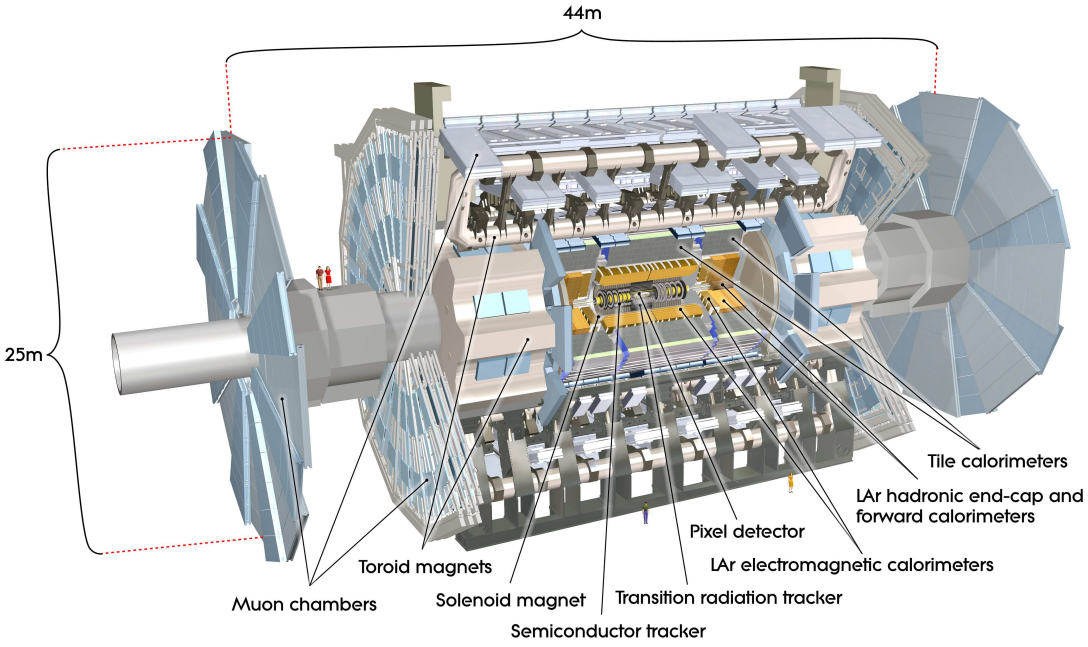

Figure 3.1: An overview of the components of the ATLAS detector, including the tracking system, calorimeters, muon system, and magnets [1].

detectors for momentum measurements of charged particles, calorimeters for energy measurements of electromagnetic and hadronic radiation, and a system for measuring the momentum of muons from collisions. The detector components and their design resolutions for momentum and energy measurements are listed in Table 3.1. All together, ATLAS is 44 m long, has a diameter of 25 m, and weighs 7,000 tonnes. A multi-tiered trigger system is used to search through collisions for interesting events and reduce the event rate to a level that can be written to disk.

3.2 Magnet system

The superconducting magnets are essential to particle identification in ATLAS because they bend the tracks of charged particles according to the charge-to-mass

Component	**η coverage**	**Resolution**
Tracker	± 2.5	$\sigma_{p_T}/p_T = 0.05\% \cdot p_T \oplus 1\%$
EM calorimeter	± 3.2	$\sigma_E/E = 10\%/\sqrt{E} \oplus 0.7\%$
Hadron calorimeter:		
barrel & end-cap,	± 3.2	$\sigma_E/E = 50\%/\sqrt{E} \oplus 3\%$
forward	$3.1 < \lvert\eta\rvert < 4.9$	$\sigma_E/E = 100\%/\sqrt{E} \oplus 10\%$
μ spectrometer	± 2.7	$\sigma_{p_T}/p_T = 10\%$ at $p_T = 1$ TeV

Table 3.1: The pseudorapidity coverage and energy or momentum resolution performance goal for each ATLAS detector component [1].

ratio q/m. Three toroids and one solenoid comprise the ATLAS magnet system [90].

A superconducting solenoid magnet capable of generating a 2 T axial magnetic field is aligned with the beam axis (z-axis) and encompasses the inner tracking detector [91]. It was designed to minimize the material in front of the calorimeter systems, and has a radiation length (X_0) of approximately 0.66 at normal incidence. It has an inner diameter of 2.46 m, an outer diameter of 2.56 m, and an axial length of 5.8 m.

A cylindrical superconducting barrel toroid magnet surrounds the calorimeters as well as the two end-cap toroid magnets [92]. It is made of 8 coils that are held in long rectangular vacuum vessels with a length of 25.3 m, an inner diameter of 9.4 m, and an outer diameter of 20.1 m. The purpose of the barrel toroid is to maximize the bending power in the barrel region of the muon spectrometer system. The two end-cap toroids, on the other hand, are designed to maximize the bending power in the end-cap region [93]. Each end-cap toroid consists of a single cold mass composed of 8 rectangular coils and 8 keystone wedges. Together, the barrel and end-cap toroid magnets produce a toroidal magnetic field for the muon spectrometer of 0.5 T in the central region and 1 T in the end-cap region.

3.3 Inner tracking detector

Immediately surrounding the interaction point are three tracking detectors: the Pixel detector, the Semiconductor Tracker, and the Transition Radiation Tracker. These systems measure the momenta associated with charged particles using the track curvature induced by the solenoid's axial magnetic field. The inner detector also measures primary and secondary vertices for tracks. These utilities are essential for separating distinct collision events in the high-pileup environment of the LHC and also for identifying long-lived particles from the decay such as b-quarks. An illustration of the tracking system is show in Figure 3.2. Radiation lengths for the inner detector components were estimated using Monte Carlo, and vary as a function of η from 0.5 in the central region to 2.5 in the forward region (Figure 3.2).

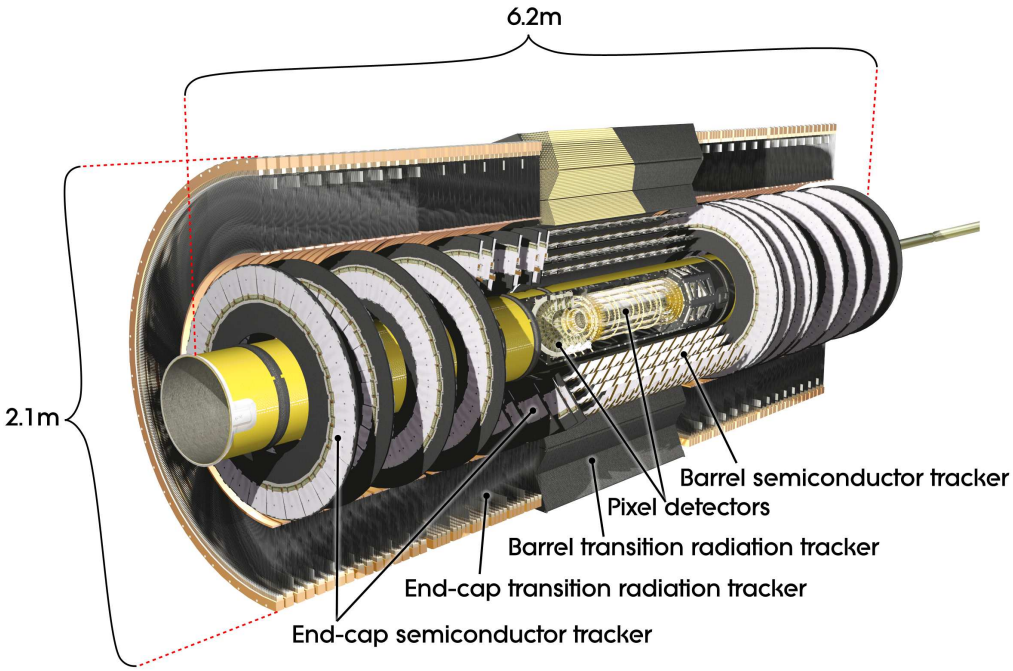

Figure 3.2: The inner tracking detectors for ATLAS [1].

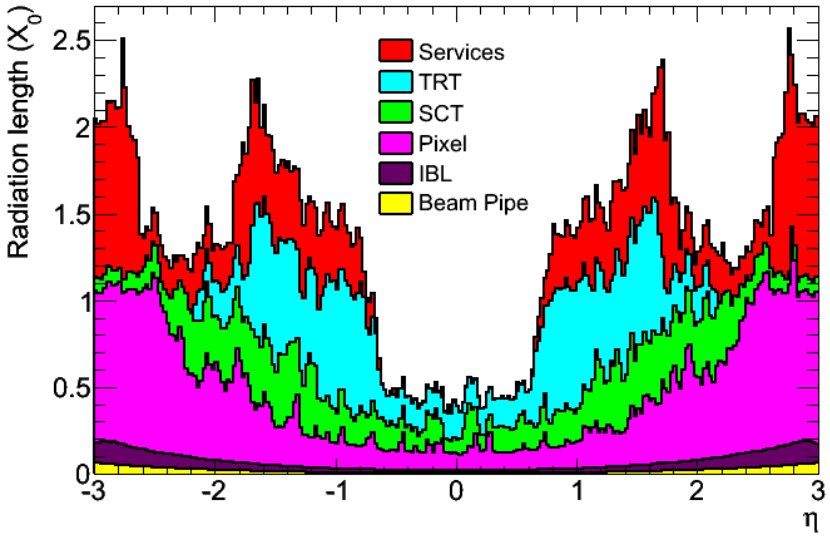

Figure 3.3: Radiation length for the ATLAS inner detector as a function of η, including the IBL upgrade for Run II [2].

3.3.1 The Pixel detector and Insertable B-Layer

The ATLAS Pixel detector [94] is the the closest detector component to the collision point and covers the pseudorapidity range $|\eta| < 2.5$. The layout consists of 3 concentric cylindric barrel layers surrounding the beam pipe at radii of 5 cm, 9 cm, and 12 cm. There are also 3 disks that are normal to the beam axis in each end-cap. In total, there are 8×10^7 pixel readout channels, with pixel areas of 50×400 μm^2. Each track typically intersects 3 layers of the Pixel detector. The tracker is segmented in R-phi and Z, and has accuracies of 115 μm in z and 10 μm in $R - \phi$.

During the long LHC shutdown from 2012 to 2015 the Insertable B-Layer (IBL), was installed [2]. The IBL reduced the distance of the closest pixel detector layer to the interaction point from 5.05 cm to 3.27 cm. A new beam pipe with a radius of 25 mm, down from 29 mm, also had to be installed to accommodate the IBL. It provides

an additional tracking measurement even closer to the collision point, enhancing the b-tagging capabilities of the experiment in Run II.

3.3.2 Semiconductor Tracker

The ATLAS Semiconductor Tracker (SCT) consists of 8 layers of silicon microstrip detectors that are located between radii of 0.3 m and 0.5 m from the beam [95]. Like Pixel, the SCT measures the$r$-θ-ϕ coordinates of charged tracks: it has accuracies of 17 μm for $R-\phi$ and 580 μm in z. The detector components are 6.36×6.40 cm^2, with 780 readout strips. There are 6.3 million readout channels in total for the SCT. Each track typically crosses eight strip layers.

3.3.3 Transition Radiation Tracker

The ATLAS Transition Radiation Tracker (TRT) is primarily used for discriminating electrons and pions and for improving the measurements of charged particle tracks [96]. It occupies the radial range 0.56 m - 1.07 m with respect to the beam axis and detects tracks from collisions by measuring x-rays that are produced by relativistic particles crossing between materials with different refraction indices. The barrel TRT component is made of 4 mm diameter straw detectors reaching up to 1.44 m in length that run parallel to the beam axis. Each straw detector contains a 30 μm diameter gold-plated Tungsten-Rhenium sensor wire inside a small, individual Xe gas compartment. Each straw is divided in half and read out at the ends. The end-caps are made of 18 wheels containing radially-oriented straws. TRT provides $R-\phi$ information only, and the drift time measurement gives a 130 μm spatial resolution per straw. The 351,000 TRT readout channels typically provide 36 hits per track.

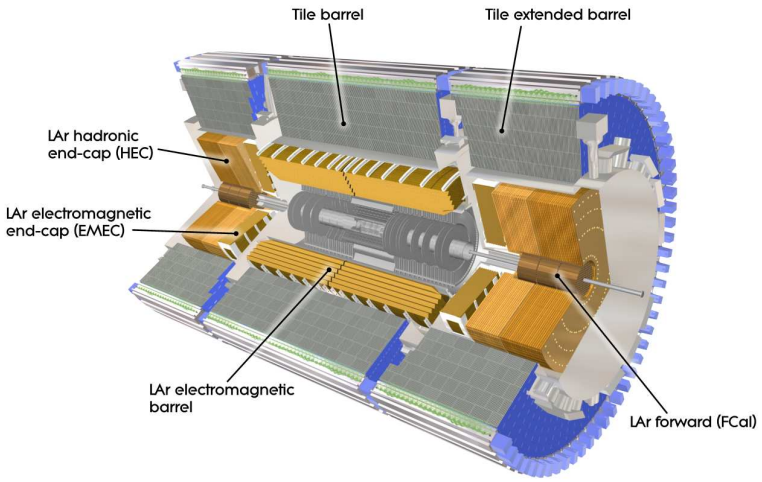

Figure 3.4: The electromagnetic liquid argon calorimeter and the hadronic tile calorimeter in ATLAS [1].

3.4 Calorimetry

Surrounding the inner tracking detectors and the solenoid magnet are the electromagnetic calorimeter and hadronic calorimeter, which measure the energies of electromagnetically interacting particles (e.g. e, γ) and hadronic particles (e.g. baryons, mesons) produced in pp collisions. Two forward calorimeters, the liquid-argon hadronic end-cap calorimeter (HEC), and the liquid-argon forward calorimeter (FCAL), also measure energy depositions at high pseudorapidities with less precision. Figure 3.4 shows the layout of the ATLAS calorimeter system. Together, the systems cover a pseudorapidity range of $|\eta| < 4.9$.

3.4.1 Electromagnetic calorimeter

The liquid argon (LAr) calorimeter is a high-granularity electromagnetic calorimeter that sits just outside the solenoid magnet [97]. It is designed to make precision measurements of electrons and photons, which lose energy through *Bremsstrahlung*

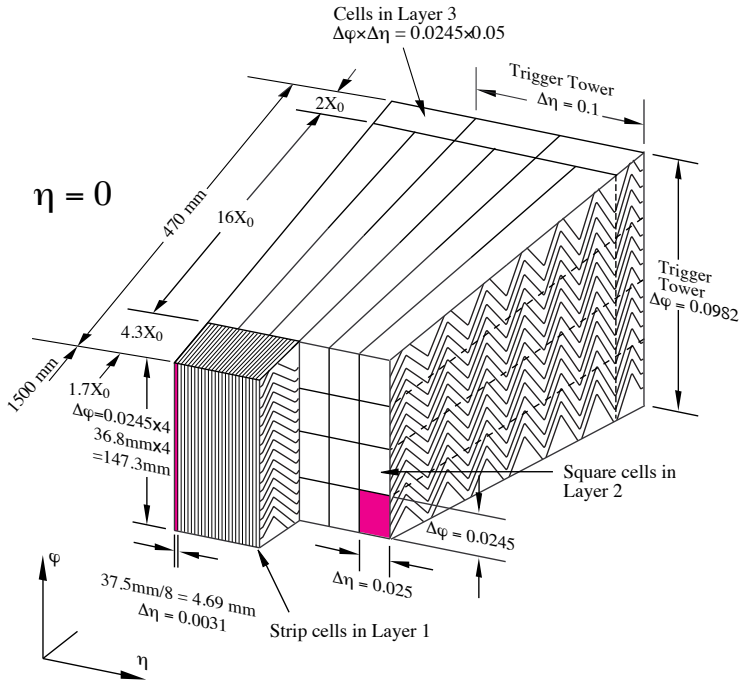

Figure 3.5: A barrel module of the liquid argon EM calorimeter in ATLAS [1].

radiation and e^+e^- pair production, respectively. The active calorimeter volume provides radiation lengths of $X_0 > 22$ in the barrel region and $X_0 > 24$ in the end-cap region.

Particles ionize the liquid Argon as they pass through the calorimeter. Lead absorber plates and kapton electrodes in the calorimeter have an accordion geometry that enables gapless coverage in ϕ. The barrel component of the calorimeter covers $|\eta| < 1.475$, while the two end-cap components cover $1.375 < |\eta| < 3.2$.

The first sampling layer is segmented in η with a granularity of 0.003 to 0.006 in $\Delta\eta$ to allow precision position measurements and to distinguish π^0 decays from single photons. EM showers deposit most of their energy in the second calorimeter layer, which has a granularity of $\Delta\eta \times \Delta\phi = 0.025 \times 0.025$. The third layer measures

leakage of showers into the hadronic calorimeter. Figure 3.5 shows the configuration of a 3-layer barrel module for the EM calorimeter. Additionally, the region $|\eta| < 1.8$ has a LAr pre-sampling layer that corrects for energy lost by particles prior to entering the calorimeters.

3.4.2 Hadronic calorimeter

The tile calorimeter (TileCal) is a coarse-granularity hadronic calorimeter that surrounds the EM calorimeter and measures jet energy and E_T^{miss} [98]. The active calorimeter volume consists of 3 layers that provide 9.7 interaction lengths (λ) in the barrel and 10 in the end-cap region. Slices of steel absorbers are interspersed with tile scintillator samplers in each calorimeter cell. The central barrel component covers $|\eta| < 1.0$, while the extended-barrels cover $0.80 < |\eta| < 1.7$. TileCal extends from a radius of 2.28 m to 4.25 m and has a length of 12 m.

3.5 Muon system

The muon spectrometer provides precision momentum measurement and triggering capabilities for muons that are deflected by the toroid magnets [99]. Three cylindrical layers of muon chambers surround the calorimeters in the barrel, while three circular planes of chambers that are normal to the beam axis are stationed on the end-caps. Precision measurements of the transverse momentum are provided by the Monitored Drift Tube (MDT) chambers for $|\eta| < 2.7$ and an innermost layer of Cathode-Strip Chambers (CSC) for the forward region $2 < |\eta| < 2.7$. Two separate systems, the Resistive Plate Chambers (RPC) and Thin Gap Chambers (TGC), enable fast triggering on μ tracks in the barrel region ($|\eta| < 1.05$) and end-cap region

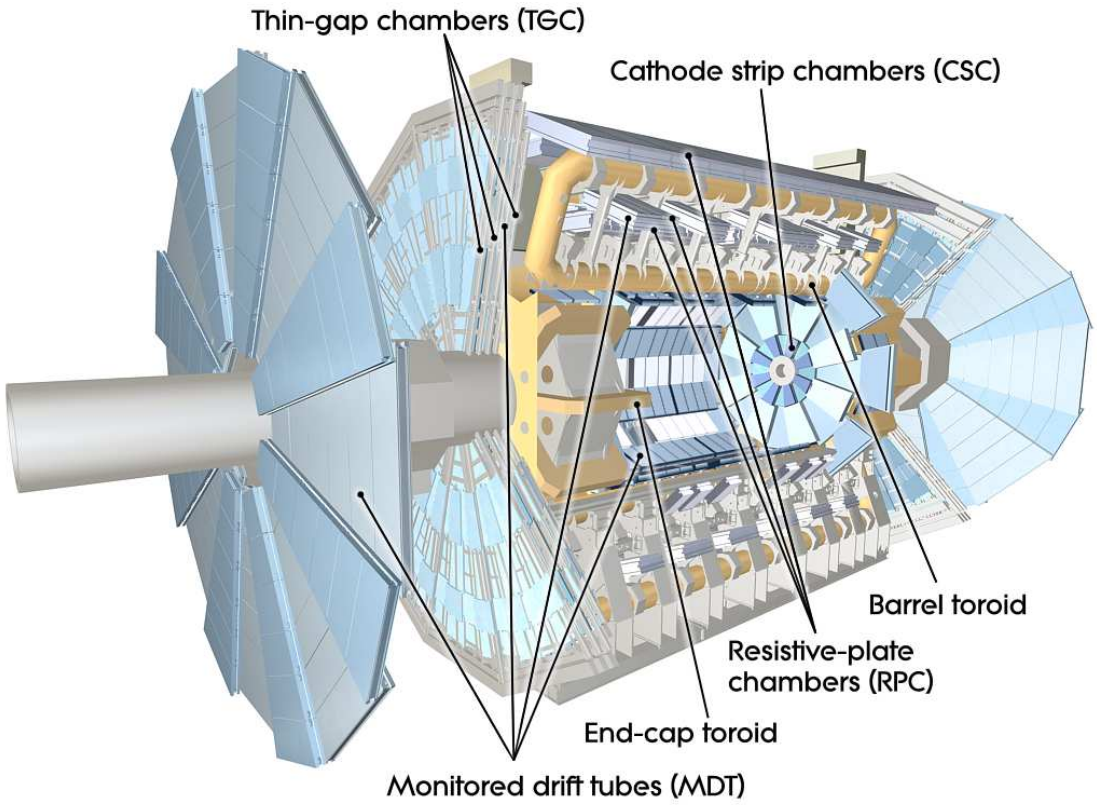

Figure 3.6: An overview of the ATLAS muon system [1].

($1.05 < |\eta| < 2.4$), respectively. The full muon spectrometer system is illustrated in Figure 3.6.

3.6 Trigger system

A three-tiered trigger system reduces the data rate to a level which can be written to disk. The LHC is capable of generating events at a 1 gHz frequency, and each event in ATLAS generates 25 MB of raw data (1.5 MB after zero-suppression). The Level 1 (L1) Trigger searches through collisions for high-p_T objects or large E_T^{miss} using information from the calorimeters and the RPC and TGC muon sub-systems. The output rate of the L1 Trigger is 100 kHz with a 2 μs latency. The Level 2 (L2)

Trigger further reduces the event rate by searching for interesting events using the full calorimeter and tracker granularities in regions of interest (RoI) in η and ϕ identified by the L1 Trigger. The L2 output rate is 1 kHz and has a latency of up to 10 ms. Finally, the event filter selected events for physics analysis using offline algorithms with processing times of a few seconds. The EF output rate is approximately 200 Hz.

The ATLAS trigger system was updated to a two-tiered structure for Run II of the LHC. It consists of an L1 Trigger and a High-Level Trigger (HLT). The HLT essentially replaced the L2 and EF tiers from the Run I trigger system. The output rate for the HLT is approximately 1 kHz.

Chapter 4

Data and simulations

This chapter summarizes the data and simulation samples that were analyzed in the search for the Standard Model Higgs boson and the search for high-mass scalar particles in the $\gamma\gamma$ final state. Sections 4.1.1 and 4.1.2 describe the LHC collision data that were analyzed for the two searches. Sections 4.2.1 and 4.2.2 describe the Monte Carlo simulations of the Higgs boson signal and high-mass scalar signal that were used for optimization and modeling studies. Simulations of the dominant $\gamma\gamma$, γ-jet, and dijet backgrounds are described in Section 4.2.3.

4.1 Data samples

4.1.1 Data for the Standard Model Higgs boson search

The search for the Standard Model Higgs boson was conducted using pp collision data from the LHC collected during 2011 at a center-of-mass energy of $\sqrt{s} = 7$ TeV and during 2012 prior to June 2012 at a center-of-mass energy of $\sqrt{s} = 8$ TeV. The average number of interactions per bunch crossing, μ, was 9.1 for $\sqrt{s} = 7$ TeV data and

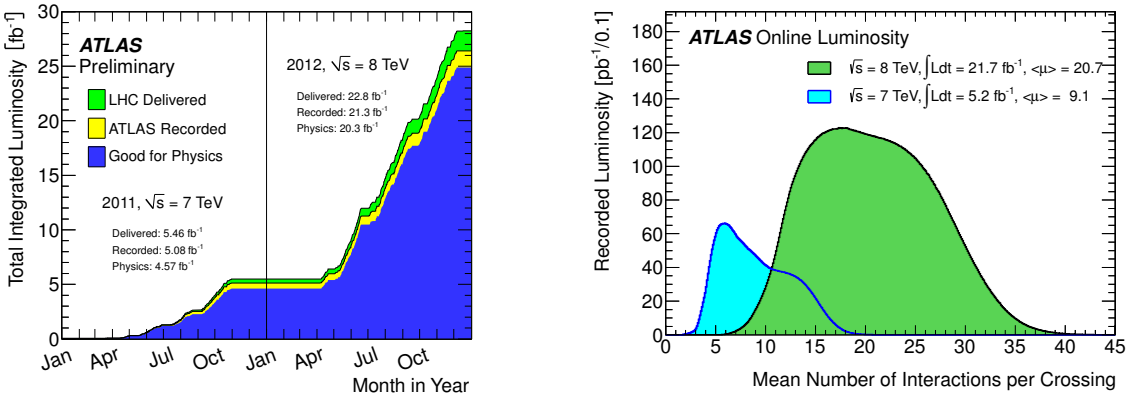

(a) (b)

Figure 4.1: The integrated luminosity (4.1a) and average interactions per bunch crossing (4.1b) for the $\sqrt{s} = 7$ TeV and $\sqrt{s} = 8$ TeV data samples.

19.5 for $\sqrt{s} = 8$ TeV data with a proton bunch spacing of 50 ns. The instantaneous luminosity peaked at 3.65×10^{33} cm^{-2}s^{-1} in 2011 and at 6.8×10^{33} cm^{-2}s^{-1} in 2012.

Figure 4.1 shows the integrated luminosity as a function of time as well as the mean number of interactions per bunch crossing for the full 2011 and 2012 data samples. In order to be considered for analysis, the data were required to pass quality requirements including stable beam conditions, fully operational tracking detectors and calorimeters, and a working trigger system. ATLAS was able to record LHC-delivered collisions in 2011 and 2012 with a 93% efficiency. The data quality selection had a 94% efficiency during this same period. The $\sqrt{s} = 7$ TeV and $\sqrt{s} = 8$ TeV data corresponded to integrated luminosities of 4.8 fb^{-1} with an uncertainty of 1.8% and 5.9 fb^{-1} with an uncertainty of 3.6%, respectively. Ref. [100] describes the luminosity calibration methodology as well as the evaluation of the systematic uncertainties.

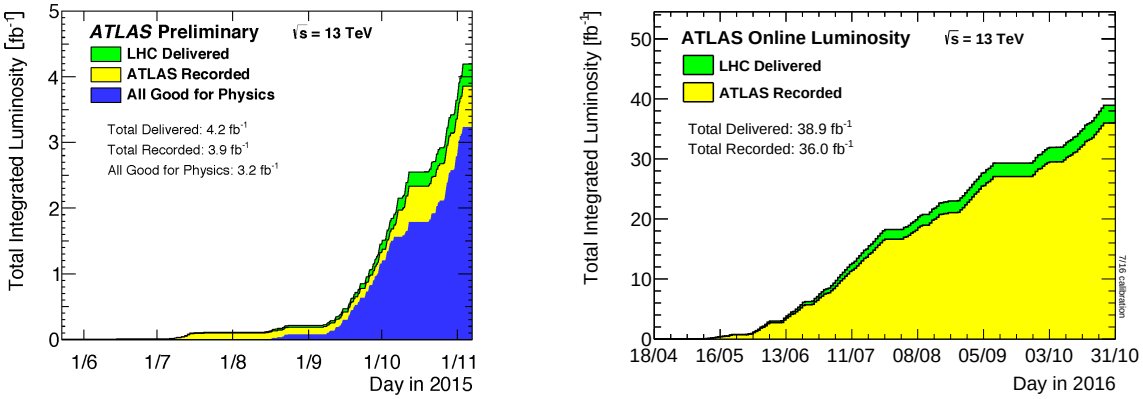

(a) 2015 data.

(b) 2016 data.

Figure 4.2: The integrated luminosities of the 2015 and 2016 data samples.

4.1.2 Data for the high-mass scalar search

The search for high-mass scalar particles was conducted using pp collision data from the LHC collected during 2015 and the first half of 2016 at a center-of-mass energy of $\sqrt{s} = 13$ TeV. Collisions occurred with a 25 ns proton bunch spacing, and the average number of interactions per bunch crossing was 13 in 2015 data and 22 in 2016 data. A peak instantaneous luminosity of 1.0×10^{34} cm^{-2}s^{-1} was achieved during this time.

Figure 4.2 shows the integrated luminosity delivered by the LHC and recorded by ATLAS as a function of time during 2015 and 2016. ATLAS was able to record collisions delivered by the LHC with an efficiency of 93%, and ATLAS-recorded data passed the data quality requirements with an 82% efficiency during 2015. The data samples corresponded to integrated luminosities of 3.2 fb^{-1} with an error of $\pm 2.1\%$ for 2015 and 12.2 fb^{-1} with an error of $\pm 3.7\%$ for 2016. Combined, the data correspond to an integrated luminosity of 15.4 fb^{-1} with an error of $\pm 2.9\%$.

4.2 Simulated samples

4.2.1 Standard Model Higgs boson signal simulations

Monte Carlo simulations of the Higgs boson signal decaying to $\gamma\gamma$ were used to optimize the analysis selection and to develop models of the $m_{\gamma\gamma}$ observable in the search for the Standard Model Higgs boson. The five dominant Higgs production modes described in Section 2.3 were simulated separately. POWHEG was used to generate the hard-scattering process for *ggH* [101] and *VBF* [102]. Parton showering, hadronization, and the underlying event were simulated with PYTHIA6 [89] in $\sqrt{s} = 7$ TeV simulations and PYTHIA8 [103] in $\sqrt{s} = 8$ TeV simulations. The *WH*, *ZH*, and $t\bar{t}H$ hard-scattering processes were also simulated with PYTHIA6 for $\sqrt{s} = 7$ TeV and PYTHIA8 for $\sqrt{s} = 8$ TeV. Signal normalizations were calculated according to the prescriptions in Section 2.3. Simulation samples were produced for each signal production mode in a range of hypothetical Higgs boson masses between 100 GeV and 150 GeV in steps of 5 GeV.

GEANT4 [104] was used to fully simulate the ATLAS detector geometry and material distribution [105]. Pileup conditions for the detector were also included in the simulation. Simulated events were weighted to match the average number of interactions per bunch crossing in data and the z-vertex distribution of collisions. The same reconstruction and selection algorithms used for data were applied to the simulated samples in order to measure the expected acceptance and efficiency for the Higgs boson signal.

4.2.2 High-mass scalar signal simulations

Monte Carlo simulations of high-mass scalar particles decaying to $\gamma\gamma$ were used for optimization and modeling of the $m_{\gamma\gamma}$ observable in the high-mass scalar search. Signal events were generated at next-to-leading order in QCD using an effective field theory implemented in MadGraph5_aMC@NLO [106]. The samples were generated with the NNPDF3.0 NLO parton distribution functions [107] using Pythia8 with the A14 tune [108] for parton showering. Pileup events were simulated with Pythia8 [103] and overlaid on the signal events. Signals were simulated for resonance masses between $m_X = 200$ GeV and $m_X = 2400$ GeV and for widths between $\Gamma_X = 4$ MeV and $\Gamma_X/m_X = 15\%$. As in the Higgs boson search, the generated events were passed through the full simulation of the ATLAS detector [105] and then weighted to match the z-vertex and μ distributions of data.

4.2.3 Background process simulations

The search for the Higgs boson in the $\gamma\gamma$ channel required very large samples of background Monte Carlo for the spurious signal procedure outlined in Section 7.2.2. Three generators were used to simulate the irreducible prompt diphoton background: Sherpa [109], Resbos [110], and Diphox [85]. The reducible background from γ-jet was simulated with Sherpa, while the dijet background was simulated with Pythia6 [89].

Large Monte Carlo sample sizes were necessary for modeling the high-statistics background with high precision, so it was infeasible to pass simulated events through a full detector simulation. Instead, detector effects were mimicked in the Monte Carlo by weighting events and smearing the particle momenta and energies. The Sherpa

$\gamma\gamma$ and γ-jet and the PYTHIA dijet samples were corrected for effects such as the photon identification efficiency, the photon energy resolution, photon conversions in the detector, and processes in which jets fake photons. Measurements of the $\gamma\gamma$, γ-jet, and dijet fractions in data were used determine the relative normalizations of the backgrounds. The smearing and weighting techniques were not applied to the RESBOS and DIPHOX samples, which were only corrected to account for the photon identification efficiency.

Additionally, a smaller number of Monte Carlo events were generated using the full ATLAS detector simulation [105]. SHERPA was used to generate the $\gamma\gamma$ background, while the γ-jet processes were simulated with ALPGEN [111]. These simulations were used for optimization studies and comparisons with kinematic distributions in data.

The high-mass scalar search in the $\gamma\gamma$ final state also required background Monte Carlo simulations for modeling and optimization studies. SHERPA 2.1.1 [109] was used to simulate the irreducible prompt diphoton background. Matrix elements with up to two partons were calculated to leading order in QCD. The reducible γ-jet background was also simulated with SHERPA 2.1.1, and matrix elements were calculated with up to four partons at LO. For both the $\gamma\gamma$ and γ-jet simulations, Sherpa parton showering [112] with the ME+PS@LO prescription [113] was interfaced to the generator, and the C10 PDF set [114] was used. Smaller samples of background Monte Carlo were necessary for modeling the high-mass background, since fewer events were expected in data. As a result, it was possible to pass the Monte Carlo events through the full ATLAS detector simulation [105].

Chapter 5

Reconstruction of physics objects

This chapter describes the reconstruction of physics objects from detector measurements in ATLAS. Section 5.1 covers the techniques that were used for the reconstruction, calibration, and identification of photon candidates. Most of the chapter is devoted to photons, since they were of primary importance in the search for the Standard Model Higgs boson and the search for high-mass scalar particles. Jet reconstruction and selection methods are also discussed in Section 5.2, since jets were used to enhance sensitivity to *VBF* production in the search for the Standard Model Higgs boson. Leptons, b-jets, and E_T^{miss} did not play a role in either search and are not discussed. Curious readers are invited to consult Ref. [115–120] for more information.

5.1 Photon candidates

5.1.1 Photon reconstruction

Photon reconstruction algorithms were applied to clusters of energy deposited in the electromagnetic calorimeter. Clusters were identified using a sliding-window

technique that searched for transverse energy measurements greater than 2.5 GeV within a region of $\Delta\eta \times \Delta\phi = 0.075 \times 0.123$ in the three EM calorimeter layers and the pre-sampling layer [121]. The η and ϕ positions of the EM clusters were matched to tracks reconstructed from hits in the inner detector [122].

Since photons produced in collisions often convert to e^+e^- pairs prior to reaching the electromagnetic calorimeter, the reconstruction algorithm had to distinguish unconverted photons, converted photons, and electrons. Unconverted photon candidates were identified using clusters that were not matched to any tracks from the inner detector. Converted photon candidates were identified using clusters that were matched to a track with a conversion vertex. Both single-track events (in which a cluster was matched to a single track with a conversion vertex) and two-track events (in which clusters were matched to a pair of tracks that shared a conversion vertex) were used to reconstruct converted photons. Other clusters and tracks were classified as electron candidates.

The photon reconstruction algorithms were updated in 2015 and 2016 for use in the high-mass scalar search. In particular, electron-oriented algorithms for pattern recognition and track fitting were used in addition to the standard track reconstruction algorithms. The converted photon criteria were also updated in order to accommodate the high-pileup conditions in the data.

Photon candidates were only considered for analysis if they were identified in the region $|\eta| < 2.37$, excluding the low-granularity barrel-end-cap transition region $1.37 < |\eta| < 1.52$. Overall, the average reconstruction efficiency for photons with $E_T > 25$ GeV was 96% in 2011 and 2012 [123]. The other 4% of photons were reconstructed as electrons. In the high-p_T region, the photon conversion reconstruction

efficiency decreased to 90% at $E_T = 1$ TeV due to the decreased separation between conversion tracks.

5.1.2 Photon energy calibration

The photon energy measurement relied on the electromagnetic calorimeter cells associated with candidate cluster in the pre-sampler and three calorimeter layers. For unconverted photons, cluster windows of $\Delta\eta \times \Delta\phi = 0.075 \times 0.123$ and 0.125×0.123 were used in the barrel and end-cap detector regions, respectively. A larger window of 0.075×0.172 for converted photon clusters in the barrel accounted for the separation of e^+e^- pairs in ϕ due to the solenoid field. The same 0.125×0.123 window was used for converted photon calibration in the end-cap region.

Separate calibrations were applied for converted and unconverted photons in order to account for energy loss prior to the particles entering the calorimeters and for energy leakage outside the clusters or into the hadronic calorimeter. η dependent correction factors for the calibration were derived using $Z \to e^+e^-$ events in data and had values on the order of 1%. Monte Carlo simulations, which were smeared to match the energy resolution in data, were also used to improve the energy corrections for converted photons. This was done by applying a scale factor so that the line-shape of $Z \to e^+e^-$ matched that in data. The scaling factors were derived for electrons and extrapolated to photons, and a small systematic uncertainty was applied to account for potential differences between γ and $e^{\pm}$.

A multivariate regression algorithm trained on Monte Carlo simulations was used to calibrate electrons and photons [124] in 2015 and 2016 data. Discriminating variables for the boosted decision tree included the energy measurements per calorimeter

layer, the η positions of the clusters, the cluster centroid in the second sampling layer, the transverse momenta of conversion tracks, and the conversion radii for converted photons. Layer energies were calibrated based on measurements in 2012 data, and the overall energy scale in data was measured with 2015 Zee data [125].

The energy scale uncertainties varied between $0.5\% - 2.0\%$ depending on η. The energy resolution uncertainty for photons with E_T 60 GeV varied between $5\% - 20\%$ for different η regions in 2011 and 2012 [126]. During 2015 and 2016, the energy resolution of photons with hundreds of GeV of energy varied between $30\% - 45\%$. $Z \to e^+e^-\gamma$ decays were used to independently cross-check the calibrations, which showed stability on the order of $\pm 0.1\%$ during data-taking.

5.1.3 Photon identification

Shower shapes of energy clusters in the electromagnetic calorimeter were analyzed to classify photon candidates [123]. A *loose* photon identification, used for the event trigger and the initial photon selection, consisted of rectangular cuts on shower shape variables related to the second EM calorimeter layer as well as the energy deposited in the hadronic calorimeter. The variables used for the *loose* photon identification are listed below.

- $\boldsymbol{R}_{\text{had,1}}$: Ratio of the E_T in the first sampling layer of the hadronic calorimeter to the E_T of the EM cluster.
- $\boldsymbol{R}_{\text{had}}$: Ratio of E_T in the hadronic calorimeter to the E_T in the EM cluster.
- $\boldsymbol{R}_{\boldsymbol{\eta}}$: Ratio of cell energies in $\Delta\eta \times \Delta\phi = 3 \times 7$ to cell energies in 7×7 for the second layer of the EM calorimeter.

- $\boldsymbol{\omega_{\eta,2}}$: Lateral shower width in the second layer of the EM calorimeter.

A *tight* photon identification was also defined for the final selection of photons in the analyses. In addition to the variables associated with the loose photon identification, the *tight* algorithm considered shower shape variables related to the finely segmented strip layer of the EM calorimeter:

- $\boldsymbol{R_{\phi}}$: Ratio of cell energies in $\Delta\eta \times \Delta\phi = 3 \times 3$ to cell energies in 3×7.
- $\boldsymbol{\omega}_{\mathrm{s},3}$: The shower width based on the three cells in the strip layer surrounding the strip with the maximum energy deposit.
- $\boldsymbol{\omega_{s,tot.}}$: The total lateral width of the EM shower in the strip layer.
- $\boldsymbol{F}_{\mathrm{side}}$: Fraction of energy deposited in non-core strips: $(E_{7 \text{ strips}} - E_{3 \text{ strips}})/E_{3 \text{ strips}}$.
- $\boldsymbol{\Delta E}$: Difference between the reconstructed energy associated with the second maximum in the strip layer and the minimum in the strip layer between the first and second maxima.
- $\boldsymbol{E}_{\mathrm{ratio}}$: $(E_{\mathrm{max},1} - E_{\mathrm{max},2})/(E_{\mathrm{max},1} + E_{\mathrm{max},2})$, where $E_{\mathrm{max},1}$ and $E_{\mathrm{max},2}$ are the largest and second largest energy deposits, respectively.

The photon identification algorithms were trained separately for converted and unconverted photons using Monte Carlo simulations in which the shower shape variables were shifted to improve the agreement with the distributions observed in data. A neural network classification algorithm was used for the *tight* photon identification with $\sqrt{s} = 7$ TeV data, while a rectangular cut-based selection that was less sensitive to pileup was used with $\sqrt{s} = 8$ TeV data and $\sqrt{s} = 13$ TeV data [123].

The efficiencies of these tight photon identification algorithms increased with E_T and varied from 85% for $E_T = 50$ GeV to 95% for $E_T = 200$ GeV. Uncertainties on the efficiencies were estimated using differences in the shower shape distributions in data and simulation. They varied between 2% and 5% for $E_T > 50$ GeV depending on $|\eta|$ and E_T [127].

The probability for electrons to fake a photon identification signature in the detector varied from 3% to 10% depending on the $|\eta|$ region and γ conversion status. Overall, only one π^0 or jet out of every 5000 was expected to be mistakenly classified as a photon by the *tight* identification algorithms [128].

5.1.4 Photon isolation

Photon candidates were required to be isolated from other objects in order to improve the rejection of hadronic backgrounds. Calorimeter information and tracking information were used to define two separate isolation criteria.

The transverse isolation energy ($E_T^{\text{iso.}}$) was defined as the sum of the E_T of topoclusters with $E > 0$ in the electromagnetic and hadronic calorimeters within a cone of $\Delta R = \sqrt{(\Delta\eta)^2 + (\Delta\phi)^2} = 0.4$ around a photon candidate, excluding the $\Delta\eta \times \Delta\phi$ region of 0.125×0.175 that encompassed the barycenter of the reconstructed photon [121]. Leakage corrections were applied to account for photon energy deposited outside of the central region. Topoclusters were processed using a low-p_T jet algorithm with k_T clustering [129, 130]. The low-p_T jets were used to compute an ambient event energy due to pileup and the underlying event, which was subtracted off on an event-by-event basis [131].

A track isolation variable, $p_T^{\text{iso.}}$, was also defined as the scalar sum of the p_T of

tracks with $p_T > 1.0$ GeV in a $\Delta R = 0.2$ cone around the photon candidate. Tracks associated with converted photons were not included in the sum. Additionally, tracks were only considered in the calculation if they were matched to the γ vertex. Small discrepancies in the isolation distributions in data and Monte Carlo for $Z \to e^+e^-$, and $Z \to l^+l^-\gamma$ events were used to derive a systematic uncertainty associated with the photon isolation.

The search for the Standard Model Higgs boson relied only on the calorimeter-based isolation variable. The optimal analysis sensitivity was achieved for $E_T^{\text{iso.}} < 4$ GeV. In the high-mass scalar search, both the calorimeter and track isolation variables were considered. Photon candidates were required to have $E_T^{\text{iso.}} < 0.022 \cdot E_T + 2.45$ GeV and $p_T^{\text{iso.}} < 0.05 \cdot E_T$. These criteria were optimized for the high-E_T regime which the high-mass scalar signals were expected to occupy. The calorimeter and track-based isolation criteria had a combined efficiency of $88\% - 97\%$ for E_T between 100 GeV and 500 GeV, with an uncertainty of $1\% - 2\%$.

5.2 Jet candidates

Jet candidates were reconstructed using the anti-k_T algorithm [132] with a distance parameter of $R = 0.4$ applied to 3-dimensional topological calorimeter clusters [121, 133, 134]. The pileup-dependence of the jet response was corrected using Monte Carlo [135]. Jet candidates were also corrected to point back to the primary vertex associated with the highest $\sum p_T^2$ from tracks [134]. Additional η-dependent corrections were calculated using Monte Carlo. Finally, residual calibrations were derived *in-situ* by balancing jet p_T with reference objects such as a γ or $Z \to l^+l^-$ in data [134].

Selection criteria were used to identify jet candidates that originated from a hard scattering. Jets were only considered for analysis if they had a pseudo-rapidity $|\eta| < 4.5$. In $\sqrt{s} = 7$ TeV data, jets were required to have a minimum transverse momentum of 25 GeV. In $\sqrt{s} = 8$ TeV data, jets with $2.5 < |\eta| < 4.5$ were required to have $p_T > 30$ GeV, while jets with $|\eta| \leq 2.5$ were required to have $p_T > 25$ GeV. For a given jet and vertex, the jet vertex fraction was defined as the ratio of the scalar sum of p_T for tracks in the jet associated with the vertex to the scalar sum of p_T for all tracks associated with the jet [136]. A requirement that JVT > 0.75 was made for jets with $\eta < 2.5$ in order to suppress the background from jets produced at a different primary vertex, thus making the analysis more robust with respect to pileup. Finally, jets were required to pass quality cuts and to have a minimum separation of $\Delta R = 0.4$ from all photon candidates.

Chapter 6

Diphoton event selection

This chapter discusses the selection of events for the search for the Standard Model Higgs boson (Section 6.1), and the search for high-mass scalar particles (Section 6.2). Diphoton event triggers used to identify relevant pp LHC collisions, as well as the primary vertex selection and kinematic requirements for the diphoton candidates are discussed for both analyses. A categorization scheme for the selected events in the search for the Standard Model Higgs boson is also mentioned in Section 6.1.4.

6.1 Selection for the Standard Model Higgs boson

6.1.1 Diphoton event trigger

Proton collisions from the LHC were first identified for analysis using a diphoton trigger. Events were recorded for analysis if they contained two calorimeter clusters passing transverse energy cuts. For the $\sqrt{s} = 7$ TeV data, events were required to have at least two photons each with $E_T > 20$ GeV. Events in $\sqrt{s} = 8$ TeV data were required to have one photon with $E_T > 35$ GeV and a second photon with $E_T > 25$

GeV. A requirement that both clusters pass the *loose* photon identification criteria outlined in Section 5.1.3 was also made at the event filter level of the trigger.

A bootstrapping method was used to estimate the efficiency of the trigger for events passing the analysis selection. The trigger selection efficiency with respect to the offline diphotons was factorized as the multiple of two terms that could be evaluated using minimum-bias events: the trigger selection efficiency relative to the L1 seed and the L1 seed efficiency [137]. The efficiency of the diphoton trigger was found to be insensitive to pileup and was measured to be $98.9\% \pm 0.2\%$ in $\sqrt{s} = 7$ TeV data and $99.6\% \pm 0.1\%$ in $\sqrt{s} = 8$ TeV data. Tag and probe methods were also used to cross-check the efficiency result and evaluate the systematic uncertainties, which were less than 1%.

6.1.2 Primary vertex selection

The primary vertex selection was important because the diphoton invariant mass resolution was influenced by the resolution of the vertex selection, as shown in Figure 6.1a. As a result of the jet vertex fraction requirement for jets discussed in Section 5.2, the two-jet category selection was strongly dependent on the vertex choice.

Several methods have been developed for identifying the primary vertex of an event. One common approach was to select the z-vertex associated with the highest $\sum p_T^2$ from tracks in the event. For photons, a calorimeter pointing approach was also used to extrapolate the line running through the barycenters of the photon clusters in the fine granularity first and second EM sampling layers back to the beam axis. The calorimeter pointing approach provided a resolution for the z-vertex of approximately 15 mm. For converted photons, the conversion tracks could also be extrapolated back

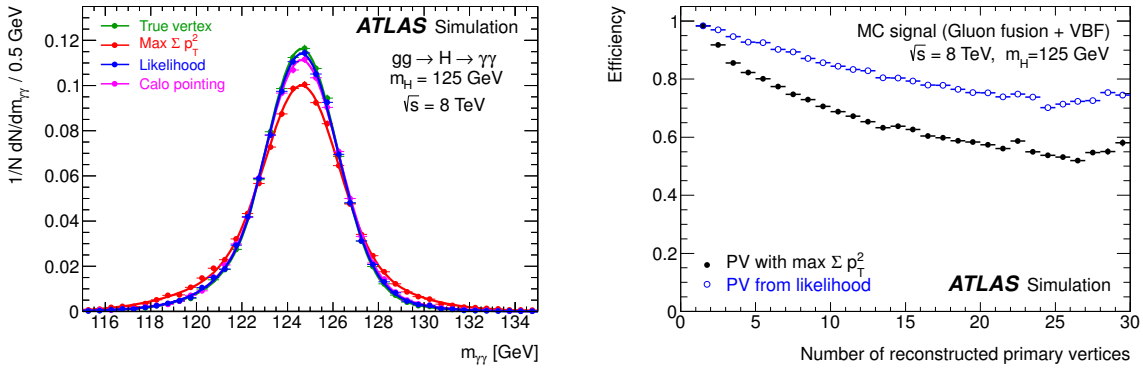

(a) (b)

Figure 6.1: The distribution of simulated Higgs boson signal events in the $m_{\gamma\gamma}$ observable is shown in Figure 6.1a for multiple vertex selection methods and for the truth vertex. Figure 6.1b shows the efficiency for reconstructing the primary vertex within $\Delta z = 0.2$ mm of the true vertex for the $\sum p_T^2$ method and the likelihood method. Both figures use a simulated Higgs boson signal with $m_H = 125$ GeV produced through the $gg \to H \to \gamma\gamma$ process.

to the beam line. This was done for $\sqrt{s} = 7$ TeV but not $\sqrt{s} = 8$ TeV data due to the higher event pileup environment.

These three methods for selecting primary vertices were combined using a global likelihood calculation. Input variables included the direction measurements for the two photons from the calorimeter sampling layers, the average beam spot position, the $\sum p_T^2$ of the tracks associated with each vertex, and the conversion vertex for converted photons associated tracks including silicon hits in $\sqrt{s} = 7$ TeV data.

The probability of selecting the correct diphoton primary vertex decreased as the number of reconstructed vertices in the event increased, as shown in Figure 6.1b. However, the likelihood vertex identification algorithm maintained a significantly higher selection efficiency than the highest $\sum p_T^2$ vertex algorithm as the amount of pileup increased. For each photon, E_T and η measurements were corrected using the se-

lected primary vertex. These values were subsequently used to calculate the diphoton invariant mass ($m_{\gamma\gamma}$).

6.1.3 Event selection

Events passing the trigger were required to contain two or more photon candidates in the detector region $|\eta_{s2}| < 2.37$, excluding $1.37 < |\eta_{s2}| < 1.52$, where the pseudorapidity was measured using the second sampling layer of the EM calorimeter. The photon with the highest transverse energy (the leading γ) was required to have $E_T > 40$ GeV, while the photon with the second-highest transverse energy (the subleading γ) was required to have $E_T > 30$ GeV. This selection was meant to ensure good sensitivity to Higgs bosons with masses between 110 GeV and 150 GeV, while also preserving a very high trigger efficiency for the signal. Various quality requirements were applied to the photon clusters, and converted photons were also rejected if they had tracks that passed through dead modules in the first pixel detector layer. Both photon candidates were also required to pass the tight photon identification outlined in Section 5.1.3 and the calorimeter isolation cut at 4 GeV outlined in Section 5.1.4. Finally, events were only considered for analysis if the diphoton invariant mass was between 100 GeV and 160 GeV. With 4.8 fb[1] of $\sqrt{s} = 7$ TeV data, 23788 events were observed following the full event selection. 35271 events were observed in the 5.9 fb^{-1} data sample with $\sqrt{s} = 8$ TeV following the full event selection.

6.1.4 Categorization

Events passing the inclusive selection procedure described in 6.1.3 were categorized in order to improve the sensitivity of the analysis to a Higgs discovery. As

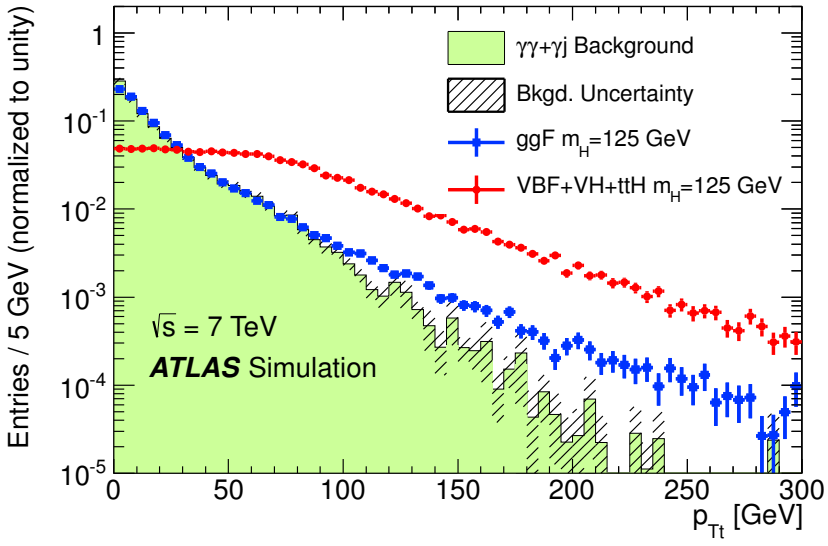

Figure 6.2: A comparison of the diphoton p_{Tt} spectrum in simulated signal and background samples. All three distributions are normalized to unit area. The $\gamma\gamma$ and γ-jet component normalizations are based on purity measurements. The signal simulations correspond to the $m_H = 125$ GeV mass hypothesis.

demonstrated in Ref. [128,138], splitting events into multiple categories with different signal-to-background ratios (s/b) and signal resolutions improved the sensitivity of the analysis. Furthermore, information about different signal production modes like vector boson fusion could be obtained by creating categories with different fractions of each mode. The Asimov formula [139] was used to evaluate the expected discovery significance for the search under the median signal-plus-background hypothesis:

$$\mathrm{med}[Z_0|1] = \sqrt{2((s+b)\ln(1+\tfrac{s}{b}) - s)}. \tag{6.1}$$

In Equation 6.1, the median expected discovery significance Z_0 is expressed in terms of the expected number of signal events s and expected number of background events b in a window containing 90% of the signal determined from Monte Carlo.

Category	$\sqrt{s} = 7$ **TeV data**	$\sqrt{s} = 8$ **TeV data**
Unconverted, central, low p_{Tt}	2054	2945
Unconverted, central, high p_{Tt}	97	173
Unconverted, rest, low p_{Tt}	7129	12136
Unconverted, rest, high p_{Tt}	444	785
Converted, central, low p_{Tt}	1493	2021
Converted, central, high p_{Tt}	77	113
Converted, rest, low p_{Tt}	8313	11112
Converted, rest, high p_{Tt}	501	708
Converted, transition	3591	5149
2-jet	89	129
Inclusive	23788	35271

Table 6.1: The number of selected events in data for the analysis categories of the SM Higgs boson search for 100 GeV $< m_{\gamma\gamma} <$ 160 GeV.

A categorization strategy was chosen that primarily relied on three event parameters: the conversion status of the two leading photon candidates, the pseudorapidity of the two photons as measured by the second sampling layer of the EM calorimeter, and the p_{Tt} of the diphoton system. Unconverted photons were associated with a better $m_{\gamma\gamma}$ resolution than converted photons, as shown in Table 6.2. Separating the two provided sets of high and low-resolution categories. Furthermore, signal events were expected to have conversions 50% of the time, while 60% of background events were expected to have converted photons. The difference was due to the presence of π^0 backgrounds that decayed to two collimated photons and had a higher conversion probability as a result.

The pseudorapidity parameter also separated events according to a high-resolution region (the barrel of the electromagnetic calorimeter) and a low-resolution region (the end-cap of the calorimeter). Scalar particles like the Higgs boson were expected to have isotropic distributions of the decay products, so the η_{s2} categorization also created

sub-samples of the data with different signal-to-background ratios.

In addition to separating signal and background, the diphoton p_{Tt} [140] discriminated between *ggH* and *VBF* signal production. The variable was defined as the orthogonal component of the $\gamma\gamma$ momentum when projected onto the axis defined by the difference of the leading and sub-leading photon transverse momenta ($p_T^{\gamma 1}$ and $p_T^{\gamma 2}$), as shown in Equation 6.2:

$$p_{Tt} = |(\vec{p}_T^{\gamma 1} + \vec{p}_T^{\gamma 2}) \times \hat{t}|, \text{ where } \hat{t} = \frac{(\vec{p}_T^{\gamma 1} - \vec{p}_T^{\gamma 2})}{|\vec{p}_T^{\gamma 1} + \vec{p}_T^{\gamma 2}|}. \tag{6.2}$$

The distribution of p_{Tt} in signal and background simulations is shown in Figure 6.2. This variable was chosen instead of the diphoton p_T because of better resolution and because cuts on the p_T (but not p_{Tt}) introduced peak structures in the $m_{\gamma\gamma}$ distribution that were difficult to model. Events were divided into low and high-p_{Tt} categories based on whether they had p_{Tt} greater or less than 60 GeV.

In addition to the categorization based on conversion status, η_{s2}, and p_{Tt}, a two-jet category was optimized for sensitivity to *VBF* production of a Higgs boson. Events in this category were required to have at least two jets with $|\eta| < 4.5$ passing the quality criteria discussed in Section 5.2. Since jets produced through *VBF* would recoil from a W or Z boson with large momenta, a cut on the dijet mass of $m_{jj} > 400$ GeV was made. The jets were also expected to be in the opposite forward regions of η, so a requirement that $|\Delta\eta_{jj}| > 2.8$ was chosen. Finally, a large difference between the diphoton and dijet azimuthal angles motivated a cut on ϕ: $\Delta\phi_{jj,\gamma\gamma} > 2.6$.

Figure 6.3 compares the jet multiplicity, $\Delta\eta_{jj}$, m_{jj}, and $\Delta\phi_{jj,\gamma\gamma}$ distributions in data with those in simulations of the signal and background. The $\gamma\gamma$ background was

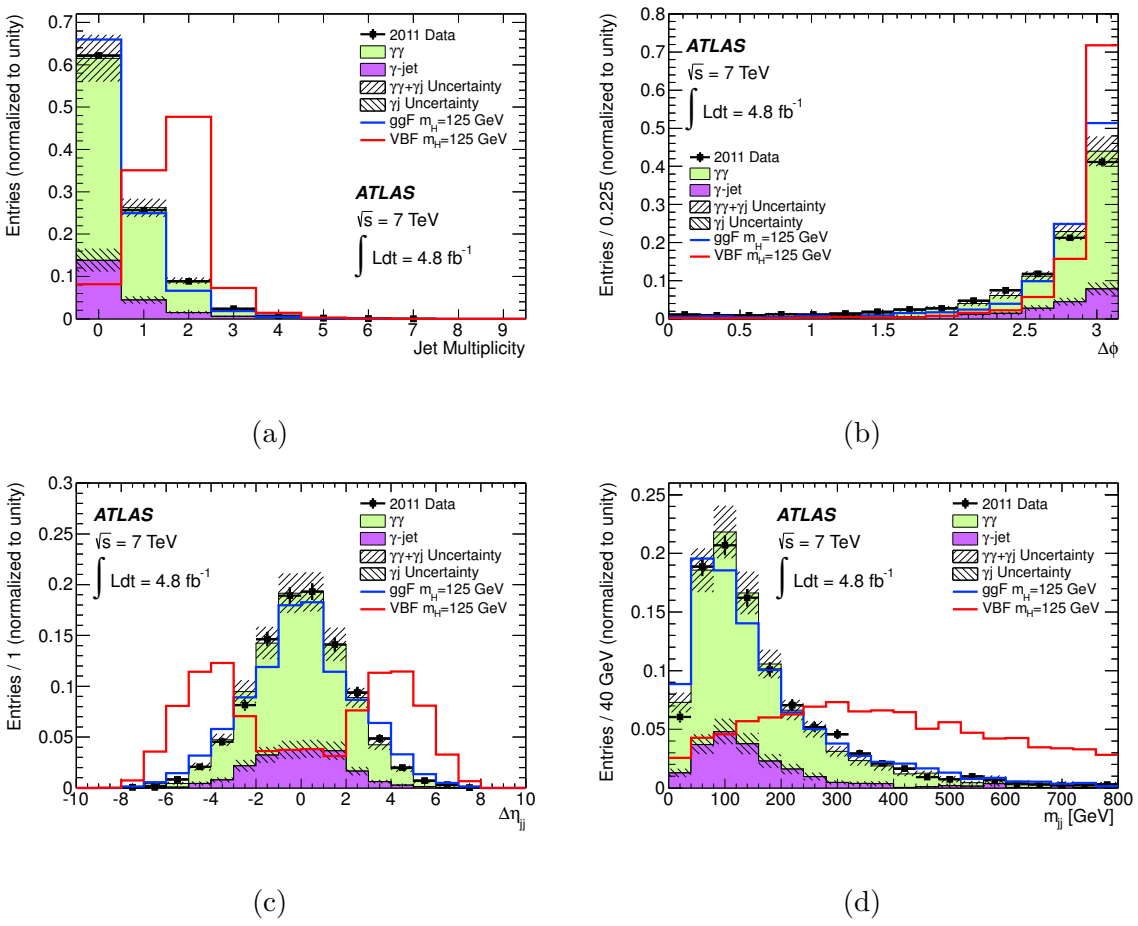

Figure 6.3: The unit-normalized signal and background distributions related to the two-jet category are compared to data for $\sqrt{s} = 7$ TeV events passing the inclusive selection. The $\gamma\gamma$ background was simulated with SHERPA, the γ-jet background was simulated with ALPGEN, and the two samples were combined according to the data-driven diphoton purity measurement. The Higgs boson signal is shown for a mass hypothesis of $m_H = 125$ GeV. Figure 6.3a shows the jet multiplicity distribution, Figure 6.3b shows the azimuthal separation of the dijet and diphoton systems, Figure 6.3c shows the pseudorapidity gap between the two jets, and Figure 6.3d shows the dijet invariant mass distribution.

generated with SHERPA [109], the γ-jet background was generated with ALPGEN [111], and both were passed through the full ATLAS detector simulation. The backgrounds were combined according to the data-driven diphoton purity measurement.

Table 6.1 provides the number of events observed in $\sqrt{s} = 7$ TeV and $\sqrt{s} = 8$ TeV data for the inclusive analysis and for each analysis category. The list below summarizes the ten categories that were used to distinguish signal from background and *ggH* from *VBF* in the search for the Standard Model Higgs boson.

- **Unconverted, central, low-p_{Tt}**: two γ candidates were reconstructed as unconverted with $|\eta_{s2}| < 0.75$, and diphoton $p_{Tt} < 60$ GeV.

- **Unconverted, central, high-p_{Tt}**: two γ candidates were reconstructed as unconverted with $|\eta_{s2}| < 0.75$, and diphoton $p_{Tt} \geq 60$ GeV.

- **Unconverted, rest, low-p_{Tt}**: two γ candidates were reconstructed as unconverted, at least one γ had $|\eta_{s2}| > 0.75$, and diphoton $p_{Tt} < 60$ GeV.

- **Unconverted, rest, high-p_{Tt}**: two γ candidates were reconstructed as unconverted, at least one γ had $|\eta_{s2}| > 0.75$, and diphoton $p_{Tt} \geq 60$ GeV.

- **Converted, central, low-p_{Tt}**: at least one γ candidate was reconstructed as converted, both photons had $|\eta_{s2}| < 0.75$, and diphoton $p_{Tt} < 60$ GeV.

- **Converted, central, high-p_{Tt}**: at least one γ candidate was reconstructed as converted, both photons had $|\eta_{s2}| < 0.75$, and diphoton $p_{Tt} \geq 60$ GeV.

- **Converted, rest, low-p_{Tt}**: at least one γ candidate was reconstructed as converted, at least one γ had $|\eta_{s2}| > 0.75$, and diphoton $p_{Tt} < 60$ GeV.

- **Converted, rest, high-p_{Tt}**: at least one γ candidate was reconstructed as converted, at least one γ had $|\eta_{s2}| > 0.75$, and diphoton $p_{Tt} \geq 60$ GeV.

- **Converted, transition**: at least one γ candidate was reconstructed as converted, and at least one γ had $1.3 < |\eta_{s2}| < 1.37$ or $1.52 < |\eta_{s2}| < 1.75$.

- **2-jet**: the event passed the two-jet selection criteria.

The invariant mass resolution, the expected number of signal and background events per category, and the number of observed events per category are provided in Table 6.2 for a hypothetical Higgs mass of $m_H = 126.5$ GeV. As expected, the high-p_{Tt} categories had better resolution than the low-p_{Tt} categories, the unconverted categories had better resolution than the converted categories, and the central-η categories had better resolution than the non-central-η categories. The highest s/b ratio was expected for the two-jet category. Eight out of the ten analysis categories observed significantly more events than expected in the background-only model.

Category	$\boldsymbol{\sigma_{CB}}$ **[GeV]**	$\boldsymbol{N}_{\text{sig.}}$	$\boldsymbol{N}_{\text{bkg.}}$	$\boldsymbol{N}_{\text{obs.}}$
Unconverted, central, low p_{Tt}	1.45	13.0	215	235
Unconverted, central, high p_{Tt}	1.37	2.3	14	15
Unconverted, rest, low p_{Tt}	1.57	28.3	1133	1131
Unconverted, rest, high p_{Tt}	1.51	4.8	68	75
Converted, central, low p_{Tt}	1.67	8.2	193	208
Converted, central, high p_{Tt}	1.50	1.5	10	13
Converted, rest, low p_{Tt}	1.93	24.6	1346	1350
Converted, rest, high p_{Tt}	1.68	4.1	72	69
Converted, transition	2.65	11.7	845	880
2-jet	1.57	2.6	12	18
Inclusive	1.63	100.4	3635	3693

Table 6.2: The expected width σ_{CB} of the Crystal Ball function that describes the Higgs boson $m_{\gamma\gamma}$ distribution in each category, along with the number of expected signal events $N_{\text{sig.}}$, the number of expected background events $N_{\text{bkg.}}$, and the number of observed events $N_{\text{obs.}}$ within a window containing 90% of the hypothetical signal. The numbers are based on $\sqrt{s} = 8$ TeV data and simulations of a Higgs boson with $m_H = 126.5$ GeV.

Category	**Events**	***ggH*** **[%]**	***VBF*** **[%]**	***WH*** **[%]**	***ZH*** **[%]**	***ttH*** **[%]**
Unconverted, central, low p_{Tt}	10.4	92.9	4.0	1.8	1.0	0.2
Unconverted, central, high p_{Tt}	1.5	66.5	15.7	9.9	5.7	2.4
Unconverted, rest, low p_{Tt}	21.6	92.8	3.9	2.0	1.1	0.2
Unconverted, rest, high p_{Tt}	2.7	65.4	16.1	10.8	6.1	1.8
Converted, central, low p_{Tt}	6.7	92.8	4.0	1.9	1.0	0.2
Converted, central, high p_{Tt}	1.0	66.6	15.3	10.0	5.7	2.5
Converted, rest, low p_{Tt}	21.0	92.8	3.8	2.0	1.1	0.2
Converted, rest, high p_{Tt}	2.7	65.3	16.0	11.0	5.9	1.8
Converted, transition	9.5	89.4	5.2	3.3	1.7	0.3
2-jet	2.2	22.5	76.7	0.4	0.2	0.1
Inclusive	79.3	87.8	7.3	2.9	1.6	0.4

Table 6.3: The total number of expected signal events per analysis category and the fractional contributions of each Higgs production mode for a Higgs boson with $m_H = 126.5$ GeV and a 4.8 fb^{-1} dataset collected with $\sqrt{s} = 7$ TeV.

Category	**Events**	***ggH*** [%]	***VBF*** [%]	***WH*** [%]	***ZH*** [%]	***ttH*** [%]
Unconverted, central, low p_{Tt}	14.4	92.9	4.2	1.7	1.0	0.2
Unconverted, central, high p_{Tt}	2.5	72.5	14.1	6.9	4.2	2.3
Unconverted, rest, low p_{Tt}	31.4	92.5	4.1	2.0	1.1	0.2
Unconverted, rest, high p_{Tt}	5.3	72.1	13.8	7.8	4.6	1.7
Converted, central, low p_{Tt}	9.1	92.8	4.3	1.7	1.0	0.3
Converted, central, high p_{Tt}	1.6	72.7	13.7	7.1	4.1	2.3
Converted, rest, low p_{Tt}	27.3	92.5	4.2	2.0	1.1	0.2
Converted, rest, high p_{Tt}	4.6	70.8	14.4	8.3	4.7	1.7
Converted, transition	13.0	88.8	6.0	3.1	1.8	0.4
2-jet	2.9	30.4	68.4	0.4	0.2	0.2
Inclusive	111.6	88.5	7.4	2.7	1.6	0.5

Table 6.4: The total number of expected signal events per analysis category and the fractional contributions of each Higgs production mode for a Higgs boson with $m_H = 126.5$ GeV and a 5.9 fb^{-1} dataset collected with $\sqrt{s} = 8$ TeV.

6.2 Selection for high-mass scalar particles

The event selection for the high-mass scalar search shared many features with the search for the Standard Model Higgs boson, since both analyses were designed to identify resonant $\gamma\gamma$ production against a non-resonant background. The differences in selection presented in this section are mostly due to the higher center-of-mass energy, the higher mass region for the search (200 GeV - 2400 GeV instead of 100-150 GeV), and the increased number of pileup events in 2015 and 2016 data.

6.2.1 Diphoton event trigger

Candidate diphoton events from LHC proton collisions were identified using a diphoton trigger. The E_T thresholds were 35 GeV for the leading photon and 25 GeV for the sub-leading photon candidate, and both were required to pass the *loose* photon identification criteria. The trigger efficiency, measured with a bootstrap method and cross-checked with tag-and-probe techniques, was close to 99% for simulated signal events passing the full analysis selection [137].

6.2.2 Primary vertex selection

Selection of the primary vertex was important for the high-mass scalar search. In addition to impacting the diphoton invariant mass resolution, the vertex choice also determined which tracks would be included in the track isolation computation described in Section 5.1.4.

A neural network discriminant was developed to replace the global likelihood method. Input variables including the direction measurements for the two photons

from the longitudinally-segmented sampling layers of the electromagnetic calorimeter along with their associated uncertainties, the average beam spot position, the $\sum p_T^2$ and scalar $\sum p_T$ of the tracks associated with each vertex, the difference in azimuthal angle $\Delta\phi$ between the vector sum of track momenta associated with each vertex and that of the diphoton system, and the conversion vertices for converted photons with silicon tracker hits were used to optimize the classifier on simulations. The efficiency of reconstructing a diphoton primary vertex within ± 0.3 mm of the true vertex was 88%.

6.2.3 Event selection

Additional identification criteria and transverse energy cuts were applied to events with two *loose* photon candidates that passed the trigger. Both photons were required to pass the *tight* photon identification selection. Only events with a leading photon $E_T > 40$ GeV and sub-leading photon $E_T > 30$ GeV were kept. In order to reduce the fake photon background from jets, the calorimeter and track-based isolation criteria described in Section 5.1.4 were also applied to the photon candidates: $E_T^{\text{iso.}} < 0.022 \cdot E_T + 2.45$ GeV and $p_T^{\text{iso.}} < 0.05 \cdot E_T$. Since scalar particles were expected to have isotropically-distributed decay products in the detector, an additional transverse energy cut was made to favor photons in the central η region. Specifically, $E_T > 0.4 \cdot m_{\gamma\gamma}$ for the leading photon and $E_T > 0.3 \cdot m_{\gamma\gamma}$ for the sub-leading photon. Finally, the search only considered events with $m_{\gamma\gamma} \geq 150$ GeV in 2015 and $m_{\gamma\gamma} \geq 180$ GeV in 2016. Overall, 7765 events were selected from the 2015 data and 15466 events were selected from the 2016 data.

6.2.4 Categorization

Events in the high-mass diphoton analysis were categorized according to the year in which they were collected (2015 or 2016). The intent was to test whether excesses observed in the standalone 2015 data [31] could be observed independently in the 2016 data. Although several categorization schemes based on the properties of the selected photon candidates were developed that had minimal model dependence, none brought a significant improvement in the search sensitivity.

Chapter 7

Signal and background modeling

This chapter describes how the invariant diphoton mass ($m_{\gamma\gamma}$) distributions of selected signal and background events were modeled in the search for the Standard Model Higgs boson and in the high-mass scalar search. Section 7.1 discusses the signal modeling, including the probability density function (PDF) to model the signal resolution, the parameterization of resolution variables as a function of resonance mass, the modeling of large-width signals, and the systematic uncertainties affecting the signal shape and yield. Section 7.2 describes the background modeling, including the composition measurement, the selection of a PDF, and the evaluation of the systematic uncertainty associated with the background description. The analytic PDFs defined in this section were used to construct the unbinned likelihood models described in Chapter 8.

7.1 Resonant signal model

7.1.1 Signal resolution for $m_{\gamma\gamma}$

The $m_{\gamma\gamma}$ distribution of the Standard Model Higgs boson was almost entirely determined by the detector resolution, as a result of the narrow ($\Gamma_H = 4$ MeV) signal width. The resolution for the narrow resonance was modeled using the sum of a Crystal Ball function [141] and a Gaussian function. The Crystal Ball PDF, defined in Equation 7.1, was used to model the core of the signal peak as well as the exponential low-mass tail of the distribution.

$$f_{\mathrm{CB}}[m_{\gamma\gamma}] = N \cdot \begin{cases} e^{-t^2/2} & \text{if } t > \alpha, \\ (\frac{n}{|\alpha|})^n \cdot e^{-\frac{1}{2}|\alpha|^2} \cdot (\frac{n}{|\alpha|} - |\alpha| - t)^{-n} & \text{if } t \leq \alpha. \end{cases} \tag{7.1}$$

In Equation 7.1, $t = (m_{\gamma\gamma} - m_H - \delta m_H)/\sigma_{\mathrm{CB}}$, where $m_{\gamma\gamma}$ is the diphoton invariant mass, m_H is the Higgs mass, δm_H represents an offset factor for the peak position and Higgs mass, and σ_{CB} represents the diphoton invariant mass resolution. N is a normalization factor for the Crystal Ball PDF, while α and n are related to the power-law damping of the low-mass tail.

The full signal model was the sum of a Crystal Ball PDF with a small Gaussian PDF to model outliers in the signal distribution:

$$f_S[m_{\gamma\gamma}] = \xi_{\mathrm{CB}} \cdot f_{\mathrm{CB}}[m_{\gamma\gamma}] + (1 - \xi_{\mathrm{CB}}) \cdot f_{\mathrm{Gauss}}[m_{\gamma\gamma}]. \tag{7.2}$$

The normalized signal PDF consisted of six parameters: the four Crystal Ball PDF parameters, the width of the Gaussian PDF (the mean was fixed so that $\mu_{\mathrm{Gauss}} = \mu_{\mathrm{CB}}$), and a relative normalization parameter for the two PDFs, ξ_{CB}. Values for each

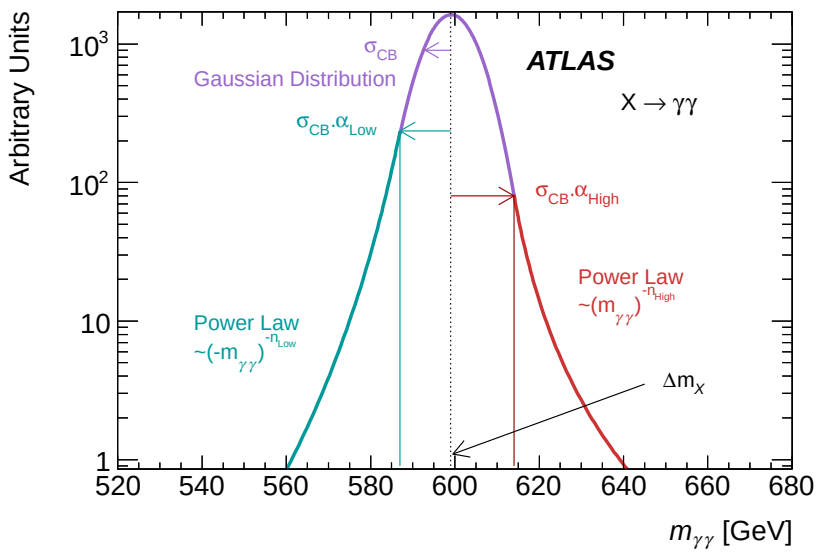

Figure 7.1: The double-sided Crystal Ball PDF used to model the $m_{\gamma\gamma}$ resolution for the high-mass scalar search.

of the parameters were obtained via maximum-likelihood fits of $f_S[m_{\gamma\gamma}]$ to the $m_{\gamma\gamma}$ distributions of the *ggH*, *VBF*, *WH*, *ZH*, and $t\bar{t}H$ Higgs signal simulations described in Section 4.2.1.

The high-mass scalar search used a slightly different PDF to describe the resolution of the narrow $m_{\gamma\gamma}$ resonance. A *double-sided* Crystal Ball PDF was chosen that improved the analytic description of the high-mass tails and resulted in a lower χ^2 probability than the Crystal Ball plus Gaussian PDF when fitted to the high-mass scalar signal simulations. Figure 7.1 illustrates the components of the double-sided Crystal Ball PDF [142], while the mathematical description of the double-sided Crystal Ball PDF is given in Equation 7.3:

$$f_{\mathrm{DCB}}[m_{\gamma\gamma}] = N \cdot \begin{cases} e^{-t^2/2} & \text{if } -\alpha_{\mathrm{low}} \leq t \leq \alpha_{\mathrm{high}}, \\ (\frac{n_{\mathrm{low}}}{\alpha_{\mathrm{low}}})^{n_{\mathrm{low}}} e^{-\alpha_{\mathrm{low}}^2/2} (\frac{n_{\mathrm{low}}}{\alpha_{\mathrm{low}}} - \alpha_{\mathrm{low}} - t)^{-n_{\mathrm{low}}} & \text{if } t < -\alpha_{\mathrm{low}}, \\ (\frac{n_{\mathrm{high}}}{\alpha_{\mathrm{high}}})^{n_{\mathrm{high}}} e^{-\alpha_{\mathrm{high}}^2/2} (\frac{n_{\mathrm{high}}}{\alpha_{\mathrm{high}}} - \alpha_{\mathrm{high}} + t)^{-n_{\mathrm{high}}} & \text{if } t > \alpha_{\mathrm{high}}. \end{cases} \tag{7.3}$$

In Equation 7.3, $t = (m_{\gamma\gamma} - m_X - \delta m_X)/\sigma_{\mathrm{CB}}$, where m_X is the mass of the scalar resonance, δm_X represents an offset factor for the peak position and the scalar mass, σ_{CB} represents the diphoton invariant mass resolution, N is an overall normalization factor, and α_{low}, n_{low}, α_{high}, and n_{high} are related to the power-law damping of the low and high-mass tails, respectively. Overall, the PDF consists of six shape variables, the values of which were obtained with maximum-likelihood fits to the high-mass scalar signal simulations discussed in Section 4.2.2.

7.1.2 Parameterization of the resolution

In the search for the Standard Model Higgs boson, the six shape variables associated with the Crystal Ball plus Gaussian PDF were parameterized as a function of m_H in order to provide an analytic description of the signal resolution that was continuous over the Higgs mass hypotheses. The δm_H, σ_{CB}, and α variables were parameterized as linear functions of m_H, while n, σ_{Gauss}, and ξ_{CB} were constant with respect to m_H. A simultaneous maximum-likelihood fit of the parameterized shape was performed for each analysis category on simulated Higgs boson signals with masses between 100 GeV and 150 GeV at increments of 5 GeV. The expected signal resolution as determined by the resolution model is provided in Table 6.2 for a Higgs boson mass of 126.5 GeV.

The expected Standard Model Higgs boson signal yields for each of the five

m_H	ggH		VBF		WH		ZH		$t\bar{t}H$		**Total**
[GeV]	ϵ [%]	$N_{\text{evt.}}$	ϵ [%]	$N_{\text{evt.}}$	ϵ [%]	$N_{\text{evt.}}$	ϵ [%]	$N_{\text{evt.}}$	ϵ [%]	$N_{\text{evt.}}$	$N_{\text{evt.}}$
110	37.3	71.7	37.9	5.2	33.5	2.8	33.5	1.5	33.7	0.4	81.6
115	39.5	73.8	40.1	5.5	34.9	2.8	35.5	1.5	34.9	0.3	83.9
120	40.9	73.5	42.1	5.8	37.0	2.6	36.9	1.4	35.9	0.3	83.6
125	42.0	70.9	43.8	5.8	38.1	2.4	38.4	1.3	37.2	0.3	80.7
130	43.1	66.3	44.8	5.7	39.3	2.1	39.9	1.2	37.8	0.3	75.6
135	44.6	59.8	46.9	5.3	40.7	1.8	40.8	1.0	38.7	0.2	68.1
140	45.2	51.7	48.7	4.8	41.8	1.5	42.3	0.9	39.5	0.2	59.1
145	45.8	42.3	49.8	4.1	42.5	1.2	43.6	0.7	40.5	0.2	48.5
150	45.8	31.6	49.7	3.1	44.1	0.9	44.7	0.5	40.7	0.1	36.2

Table 7.1: The expected signal efficiency, ϵ, and event yield, $N_{\text{evt.}}$, for the Standard Model $H \to \gamma\gamma$ process after event selection in 4.8 fb^{-1} of $\sqrt{s} = 7$ TeV data.

m_H	ggH		VBF		WH		ZH		$t\bar{t}H$		**Total**
[GeV]	ϵ [%]	$N_{\text{evt.}}$	ϵ [%]	$N_{\text{evt.}}$	ϵ [%]	$N_{\text{evt.}}$	ϵ [%]	$N_{\text{evt.}}$	ϵ [%]	$N_{\text{evt.}}$	$N_{\text{evt.}}$
110	33.8	100.6	34.5	7.4	29.9	3.7	29.5	2.1	27.3	0.6	114.4
115	35.6	103.8	36.2	7.9	30.6	3.6	32.5	2.1	27.9	0.6	118.0
120	37.2	103.6	38.1	8.2	32.7	3.4	32.9	2.0	29.4	0.6	117.8
125	38.3	100.3	39.6	8.3	33.9	3.2	34.2	1.8	29.7	0.5	114.1
130	39.1	94.1	41.2	8.0	35.1	2.8	35.9	1.6	31.1	0.5	107.0
135	40.4	85.3	42.4	7.6	35.7	2.4	36.6	1.4	32.2	0.4	97.1
140	41.1	74.0	43.0	6.8	37.0	2.0	36.8	1.2	32.4	0.3	84.3
145	41.6	60.6	43.7	5.8	38.0	1.6	38.5	0.9	33.6	0.3	69.2
150	41.7	45.3	44.8	4.4	38.2	1.1	39.2	0.7	34.0	0.2	51.7

Table 7.2: The expected signal efficiency, ϵ, and event yield, $N_{\text{evt.}}$, for the Standard Model $H \to \gamma\gamma$ process after event selection in 5.9 fb^{-1} of $\sqrt{s} = 8$ TeV data.

dominant production modes were also parameterized over the 100 GeV $\leq m_H \leq$ 150 GeV mass range with a second order polynomial. The expected signal efficiencies and yields for a range of Higgs boson masses are shown for $\sqrt{s} = 7$ TeV data in Table 7.1 and for $\sqrt{s} = 8$ TeV data in Table 7.2.

For the high-mass scalar search, the double-sided Crystal Ball description of the signal resolution was also parameterized. Due to the significantly larger search range

Variable	Parameterization	a	b	c
δm_X	$a + bmn, X + cm_{n,X}^2$	-0.0357	-0.0466	2.90×10^{-4}
σ_{CB}	$a + bm_{n,X}$	1.646	0.697	
α_{low}	$a + bm_{n,X} + cm_{n,X}^2$	1.536	-8.62×10^{-4}	-1.69×10^{-4}
n_{low}	a	12.5		
α_{high}	$a + bm_{n,X} + cm_{n,X}^2$	1.889	0.0140	-5.54×10^{-4}
n_{high}	a	9.9		

Table 7.3: Parameterizations of the double-sided Crystal Ball variables for the high-mass scalar search. In order to improve the fit convergence, the variable $m_{n,X} = \frac{m_X - 100 \text{ GeV}}{100 \text{ GeV}}$ was used to parameterize the shape with respect to the resonance mass.

(from $m_X = 200$ GeV to $m_X = 2400$ GeV), linear parameterization functions were not suitable for some of the shape variables. As shown in Table 7.3, second-order polynomials were necessary for describing the δm_X, α_{low}, and α_{high} variables, σ_{CB} was modeled as a linear function of m_X, and n_{low} and n_{high} were constant with respect to m_X.

A simultaneous fit of the parameterized resolution model was performed on simulations of narrow-width high-mass scalar particles with masses between 200 GeV and 2.5 TeV. Figure 7.2 compares the values of the double-sided Crystal Ball variables from the simultaneous fit of the parameterized resolution at all mass points to resolution fits at individual m_X points. The individual and parameterized fit results were in excellent agreement. As can be seen from the plot of σ_{CB}, the diphoton invariant mass resolution varied from 2.3 GeV for $m_X = 200$ GeV to 17.5 GeV at $m_X = 2.4$ TeV.

Since the high-mass scalar signals did not have a cross-section defined by theory, the kinematic acceptance and the efficiencies of the reconstruction and identification were parameterized as a function of m_X. The fiducial acceptance was defined as the number of generator-level events passing the $E_T^{\text{iso.}}$ requirement described in Section

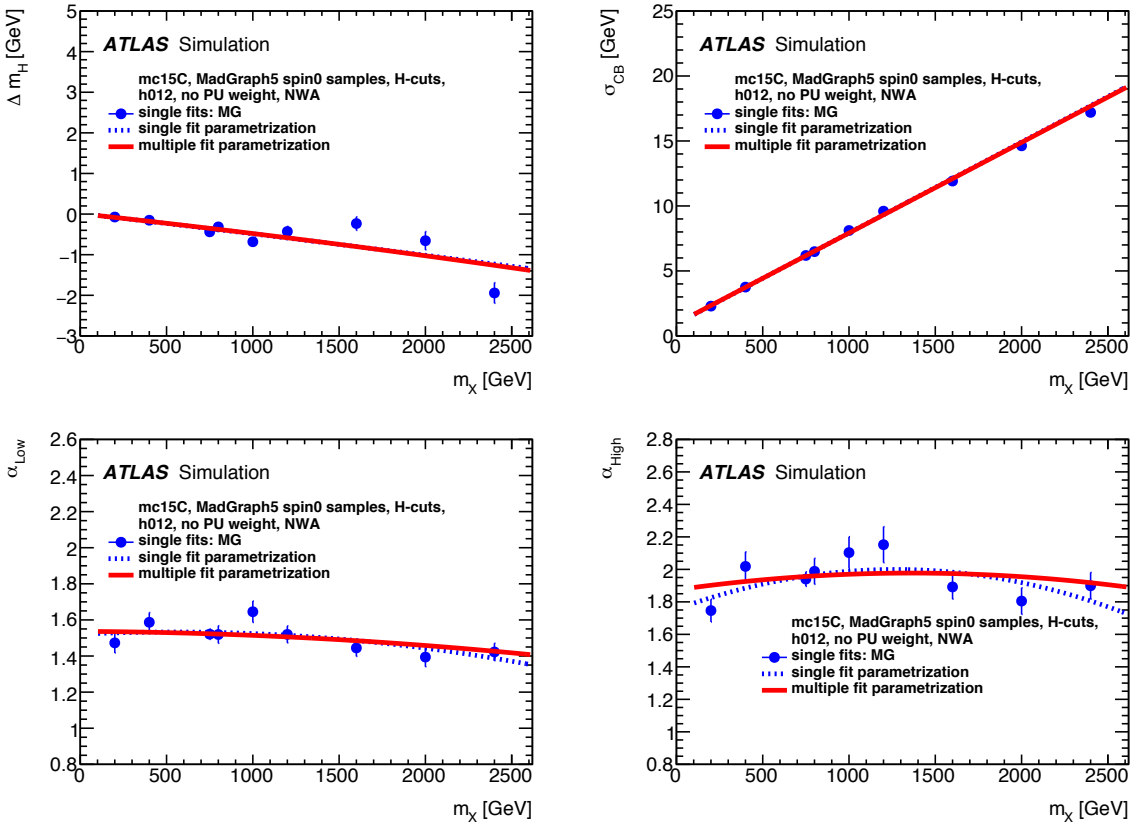

Figure 7.2: A comparison of the double-sided Crystal Ball shape variables from fits to individual m_X hypotheses and from a single parameterized fit for the entire m_X range. Comparisons are shown for δm_X (top left), σ_{CB} (top right), α_{low} (bottom left), and α_{high} (bottom right).

5.1.4 as well as the $|\eta|$ and E_T requirements described in Section 6.2.3. Acceptance for the signal ranged from 54% at $m_X = 200$ GeV to 61% at $m_X = 700$ GeV. The efficiency was defined as the ratio of the number of signal events expected to pass the reconstruction and identification requirements to the expected number of accepted signal events. The reconstruction and identification efficiency varied from 66% at $m_X = 200$ GeV to 74% for $m_X = 700$ GeV. The expected high-mass scalar signal yield was calculated as the multiple of the cross-section times branching ratio to $\gamma\gamma$, the acceptance of the kinematic selection, and the efficiency of the photon reconstruction

and identification. Search results were interpreted using the fiducial cross-section, defined as the product of the cross-section times branching ratio to $\gamma\gamma$ within the fiducial acceptance.

7.1.3 Modeling large width signals

The parameterized signal resolution model described in Section 7.1.2 was sufficient for searches involving narrow-width resonances in which the detector resolution was significantly larger than the $\Gamma = 4$ MeV signal width. However, the high-mass scalar search also considered signal models with larger values of Γ_X/m_X.

In order to model the large-width scalar signals, the parameterized detector resolution was convoluted with the mass line-shape at the generator level. The theoretical line-shape was the multiple of three components: the Breit-Wigner implemented in MadGraph5_AMC@NLO [106], the parameterization of the gluon-gluon parton luminosity from NNPDF3.0 NLO [107], and the matrix element of the effective field theory [143] times the flux factor and the phase space.

The large width model agreed well with the high-mass scalar Monte Carlo, as shown in Figure 7.3b. This figure presents a direct comparison, and not a fit, of the convolution of the detector resolution and line-shape with the large-width scalar simulation for $m_X = 800$ GeV and $\Gamma_X/m_X = 6\%$. Figure 7.3a shows the corresponding detector resolution component from a fit to the narrow width scalar simulation for $m_X = 800$ GeV.

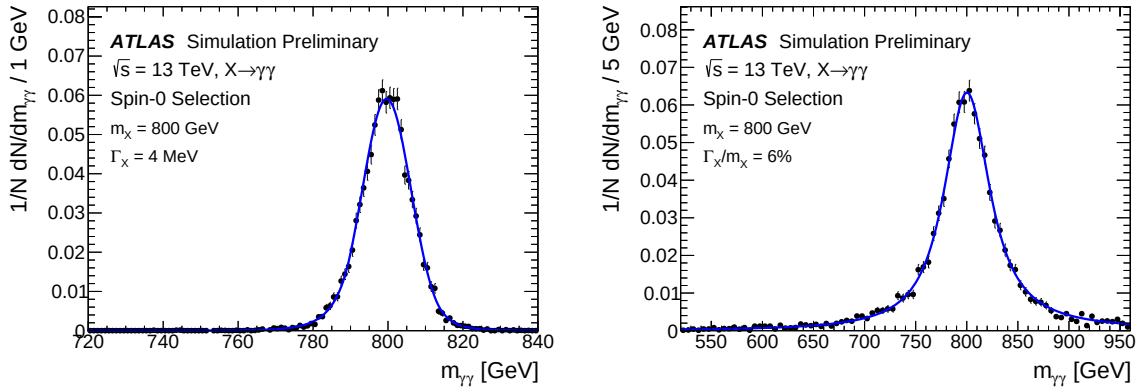

(a) $\Gamma_X = 4$ MeV. (b) $\Gamma_X/m_X = 6\%$.

Figure 7.3: The expected $m_{\gamma\gamma}$ distributions for a scalar resonance of $m_X = 800$ GeV and a width of $\Gamma_X = 4$ MeV (Figure 7.3a) or $\Gamma_X/m_X = 6\%$ (Figure 7.3b). The blue analytic signal PDF is compared with the black distribution of simulated events.

7.1.4 Systematic uncertainties affecting the signal

Systematic uncertainties affecting the expected signal in the search for the Standard Model Higgs boson and the high-mass scalar search could be broadly classified as yield systematics or shape systematics. Yield systematics, described in Section 7.1.4.1, affected either the overall normalization of the expected signal or the distribution of expected signal events among the analysis categories. Shape systematics, described in Section 7.1.4.2, affected the diphoton mass resolution and the mass scale.

7.1.4.1 Uncertainties on the signal yield

The uncertainties affecting the total number of expected signal events for the Standard Model Higgs boson search are listed below. A summary of the systematic uncertainty values is also provided in Table 7.4.

- An uncertainty on the integrated luminosity of 1.8% for $\sqrt{s} = 7$ TeV data

and 3.6% for $\sqrt{s} = 8$ TeV data was calculated using the method in Ref. [100]. The luminosity uncertainties for $\sqrt{s} = 7$ TeV and $\sqrt{s} = 8$ TeV data were uncorrelated.

- The uncertainty on the *loose* diphoton trigger efficiency was found to be 1.0%.

- The uncertainty of the photon identification efficiency was measured using Monte Carlo signal simulations and data-driven measurements with $Z \to e^+e^-\gamma$ and $Z \to e^+e^-$ events. For $\sqrt{s} = 7$ TeV data, the relative systematic uncertainty of the neural-network photon identification algorithm was approximately 4% per photon. A relative uncertainty of 8.4% on the expected signal yield in $\sqrt{s} = 7$ TeV data was found by fully correlating the photon identification uncertainties between photons in each event. In the $\sqrt{s} = 8$ TeV analysis, the photon identification uncertainty was 5% for photons in the barrel region and 7% for photons in the end-cap region. This corresponded to an uncertainty on the expected signal yield of 10.8% in $\sqrt{s} = 8$ TeV data after fully correlating the uncertainties due to each photon in the event.

- An uncertainty on the expected signal yield due to the efficiency of the isolation cut was found to be 0.4% per event in $\sqrt{s} = 7$ TeV data and 0.5% for $\sqrt{s} = 8$ TeV data. The size of the systematic uncertainty was evaluated by comparing the isolation cut efficiency on $Z \to e^+e^-$ events in data and Monte Carlo.

- An uncertainty due to the presence of pileup events of 4% was assigned to the expected signal yield. The effect was observed by comparing the numbers of selected events in samples with μ greater than and less than the mean in data.

- Uncertainties related to the photon energy scale, which are described more in Section 7.1.4.2, contributed a 0.3% uncertainty on the expected signal yield.

Theoretical uncertainties related to the Standard Model Higgs boson production cross-sections and the decay branching fraction for $H \to \gamma\gamma$ also affected the expected signal yield. The dominant uncertainties on the cross-section were due to the QCD perturbative uncertainties for the gluon fusion process [47, 48] and the parton distribution function uncertainties associated with the CTEQ [114], MSTW [51], and NNPDF PDF sets [144]. A 5% branching fraction uncertainty was implemented [145].

Systematic uncertainties also affected the expected distribution of signal events among the analysis categories in the search for the Standard Model Higgs boson. These sources of uncertainty, referred to as *migration* systematic uncertainties, are listed below. Correlations between the migration systematics in each analysis categories ensured a constant total signal yield. A summary of the systematic uncertainty values is also provided in Table 7.5.

- Uncertainties related to pileup events contributed to migrations of expected signal events between the analysis categories with unconverted and converted photons. In $\sqrt{s} = 7$ TeV data, the uncertainty was found to be 3% for categories with unconverted photon, 2% for categories with converted photons, and 2% for the two-jet category. The uncertainty was found to be 2% for categories with unconverted photon, 2% for categories with converted photons, and 12% for the two-jet category in $\sqrt{s} = 8$ TeV data.

- Uncertainties on the material description of the ATLAS detector also contributed to migrations of expected signal events between the conversion categories. Sim-

ulations were performed with 5% and 20% extra material upstream from the electromagnetic calorimeter, and the differences in event yields between the categories were measured. Material distributions primarily affected conversion rates, and migration uncertainties of 4% and 3.5% were assigned to categories with unconverted and converted photons, respectively.

- The selection of the primary vertex had a negligible impact ($< 0.1\%$) on migrations of events between categories.

- Uncertainties on the jet energy scale affected migrations of expected signal events for the two-jet categories. Variations of the scale corrections from Ref. [134] were used to calculate the jet energy scale uncertainty, which produced an uncertainty on the expected signal yield of 19% for the two-jets categories and 4% for the other categories.

- Jet energy resolution uncertainties had a negligible impact on the expected signal yield in each analysis category.

- The perturbative uncertainty on the ggH contribution to the two-jet categories was evaluated separately from the total cross-section uncertainty according to the procedure in Ref. [146]. An uncertainty of 25% on the expected signal yield for the two-jet categories was computed for the ggH process [147].

- A migration uncertainty resulting from the underlying event modeling was estimated by comparing different tunes of the underlying event simulation [148]. A 30% uncertainty was assigned to contributions from the ggH and VH processes, while a 6% uncertainty was assigned to the contributions from the VBF process.

Systematic uncertainty	$\sqrt{s} = 7$ **TeV** [%]	$\sqrt{s} = 8$ **TeV** [%]
γ identification	± 8.4	± 10.8
pileup	± 4	
γ energy scale	± 0.3	
γ isolation	± 0.4	± 0.5
trigger	± 1	
luminosity	± 1.8	± 3.6
σ_{Higgs} (perturbative)	ggH: $^{+12}_{-8}$, VBF: ± 0.3, WH: $^{+0.2}_{-0.8}$, ZH: $^{+1.4}_{-1.6}$, $t\bar{t}H$: $^{+3}_{-9}$, ggH + 2 jets: ± 25	ggH: $^{+7}_{-8}$, VBF: ± 0.2, WH: $^{+0.2}_{-0.6}$, ZH: $^{+1.6}_{-1.5}$, $t\bar{t}H$: $^{+4}_{-9}$,
σ_{Higgs} (PDF+α_s)	ggH: $^{+8}_{-7}$, VBF: $^{2.5}_{-2.1}$, VH: ± 3.5, $t\bar{t}H$: ± 9,	ggH: $^{+8}_{-7}$, VBF: $^{+2.6}_{-2.8}$, VH: ± 3.5, $t\bar{t}H$: ± 8,
$BR(H \to \gamma\gamma)$	± 5	
underlying event (2-jets)	VBF: ± 6, others: ± 30	

Table 7.4: A summary of the systematic uncertainties on the expected signal yield for a Standard Model Higgs boson with $m_H = 125$ GeV.

- The jet vertex fraction migration systematic uncertainty was evaluated by comparing efficiencies in data and Z + 2-jets simulations. A 13% uncertainty was assigned for $\sqrt{s} = 8$ TeV data.

- The expected kinematics of the Higgs boson signal affected the expected distribution of events among the categories, particularly as a result of the classification according to diphoton p_{Tt}. The uncertainty due to the Higgs boson modeling was quantified by varying scales and PDFs with HqT2 [48]. Uncertainties of 1.1%, 12.5%, and 9% were obtained for the low-p_{Tt} categories, high-p_{Tt} categories, and two-jet categories, respectively.

In the high-mass scalar search, uncertainties on the efficiency of the reconstruction and selection algorithms came from several sources. An uncertainty of $\pm 0.6\%$ was related to the efficiency of the *loose* diphoton trigger. The photon identification efficiency contributed a mass-dependent systematic uncertainty of $\pm 2\%$ to $\pm 3\%$,

Systematic uncertainty	$\sqrt{s} = 7$ **TeV** [%]	$\sqrt{s} = 8$ **TeV** [%]
material	unconv: ± 4, conv: ∓ 3.5	
pileup	unconv: ± 3, conv: ∓ 2 2-jets: ± 2	unconv: ± 2, conv: ∓ 2 2-jets: ± 12
jet energy scale	*low-*p_{Tt} ggH: ± 0.1, VBF: ± 2.6, others: ± 0.1	*low-*p_{Tt} ggH: ± 0.1, VBF: ± 2.3, others: ± 0.1
	high-p_{Tt} ggH: ± 0.1, VBF: ± 4 others: ± 0.1	
	2-jets ggH: ∓ 19, VBF: ∓ 8, others: ∓ 15	*2-jets* ggH: ∓ 18, VBF: ∓ 9, others: ∓ 13
jet vertex fraction	2-jets: ± 13, others: ∓ 0.3	
Higgs p_T modeling	low-p_{Tt}: ± 1.1, high-p_{Tt}: ∓ 12.5, 2-jets: ∓ 9	

Table 7.5: A summary of the systematic uncertainties on the expected distribution of signal events among the analysis categories for a SM Higgs boson with $m_H = 125$ GeV. The signs on each value represent the correlations between analysis categories.

while the photon isolation efficiency contributed another mass-dependent 1% to 4% uncertainty to the expected signal yield. Photon energy scale and energy resolution uncertainties had a negligible impact on the expected signal yield and were not implemented in the statistical model. Selected events in the high-mass scalar search were not categorized according to event topology or photon characteristics, so migration uncertainties were not necessary for the analysis.

7.1.4.2 Uncertainties on the signal shape

In the search for the Standard Model Higgs boson, the mass scale, or position of the resonance peak, was influenced primarily by systematic uncertainties related to the photon energy scale. A systematic uncertainty due to the electromagnetic calorimeter pre-sampler energy scale was estimated to be 5% for the barrel region and

10% for the calorimeter end-cap region. An additional uncertainty due to material effects for the extrapolation of the electron energy scale to photons was also evaluated separately for the regions $|\eta| < 1.8$ and $|\eta| \geq 1.8$. Multiple uncertainties related to the *in-situ* calibration technique discussed in Section 5.1.2 were also applied. Overall, a 0.6% uncertainty was assigned to the mass scale parameter, δm_H. This mass scale systematic uncertainty was correlated between the $\sqrt{s} = 7$ TeV and $\sqrt{s} = 8$ TeV data categories.

Several sources of uncertainty affected the signal resolution in the search for the Standard Model Higgs boson. One source of uncertainty was related to uncertainty on the constant term of the parameterization of the calorimeter resolution described in Ref. [126]. The constant term was 1% in the barrel of the calorimeter and up to 2.1% in the end-cap region. A 12% systematic uncertainty on the $m_{\gamma\gamma}$ resolution was assigned for the constant term of the calorimeter resolution. The extrapolation of the calorimeter response for electrons to photons contributed another 6% to the resolution uncertainty. Pileup events also affected the mass resolution. The effect was observed by comparing the full-width-half-maximum of the signal peak in events with μ greater than and less than the average from data. The impact of pileup on the $m_{\gamma\gamma}$ resolution was found to be 4%. Finally, the impact of an incorrect primary vertex selection on the mass resolution was evaluated and found to be negligible (on the order of 0.2%). Overall, the mass resolution uncertainty was 14%. This systematic uncertainty was applied to the Crystal Ball and Gaussian resolution variables σ_{CB} and σ_{GA} and was correlated between the $\sqrt{s} = 7$ TeV and $\sqrt{s} = 8$ TeV data categories.

For the high-mass scalar search, the relative uncertainty on the diphoton mass resolution was dominated by the constant term of the energy resolution parameteriza-

tion. It varied from ±17% at $m_X = 200$ GeV to ±40% at $m_X = 2$ TeV. The systematic uncertainty on the mass scale resulting from the photon energy scale uncertainty was found to be small and was neglected in the search.

7.2 Continuum background model

7.2.1 Background composition

In order to properly model the shape of the non-resonant background for the search for the Standard Model Higgs boson, it was necessary to determine the contributions from the irreducible $\gamma\gamma$ and reducible γ-jet + dijet processes. A method involving control regions obtained by relaxing the photon identification and isolation requirements was used to estimate the number of events in which jets were misidentified as photons [131, 149]. Photon isolation and identification variables were chosen because of their nearly orthogonal rejections of fake backgrounds. The Drell Yan background was determined by measuring the probabilities for electrons to be reconstructed as photons with $Z \to e^+e^-$ events.

For the $\sqrt{s} = 7$ TeV data in the Higgs boson search, $(80 \pm 4)\%$ of non-resonant events were estimated to be from $\gamma\gamma$ processes, while $(19 \pm 3)\%$ were found to be from γ-jet and $(1.8 \pm 0.5)\%$ from dijet processes. In $\sqrt{s} = 8$ TeV data, the corresponding $\gamma\gamma$, γ-jet, and dijet fractions of the non-resonant background were measured to be $(75 \pm 3)\%$, $(22 \pm 2)\%$, and $(2.6 \pm 0.5)\%$, respectively. Uncertainties on the composition estimates were related to the statistical uncertainties in the data samples, the definitions of the control regions, the modeling of the isolation distribution, and possible correlations between the isolation and identification variables. Figure 7.4 shows the

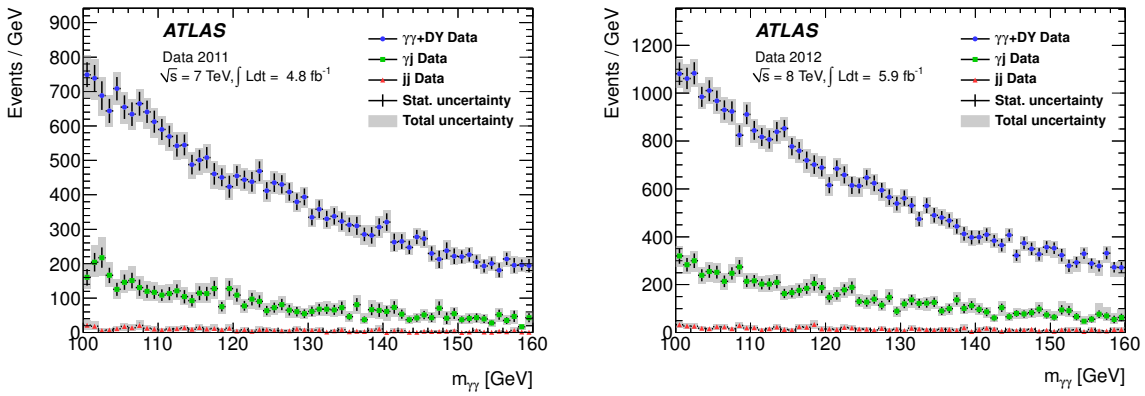

(a) $\sqrt{s} = 7$ TeV data. (b) $\sqrt{s} = 8$ TeV data.

Figure 7.4: The estimated contributions from the $\gamma\gamma$, γ-jet, and dijet processes to the non-resonant background in the search for the Standard Model Higgs boson.

purity measurement for both datasets in bins of $m_{\gamma\gamma}$. The very small contribution to the background from the Drell-Yan process was included in the $\gamma\gamma$ component.

The composition of the non-resonant background was also measured for the high-mass scalar search. A matrix method [150] and a 2×2D sideband method [151] were used to estimate a diphoton purity of $(90^{+3}_{-10})\%$. Both methods relied on relaxed photon isolation and identification control regions as in the purity measurement for the search for the Standard Model Higgs boson. The purity of the high-mass search was significantly better than in the lower mass Higgs search, since selection criteria such as the photon identification improve with photon p_T. Figure 7.5 shows the composition of the high-mass scalar search data collected during 2015 in bins of $m_{\gamma\gamma}$. Purity estimates from both the matrix and 2×2D methods are shown, and were found to agree within uncertainties.

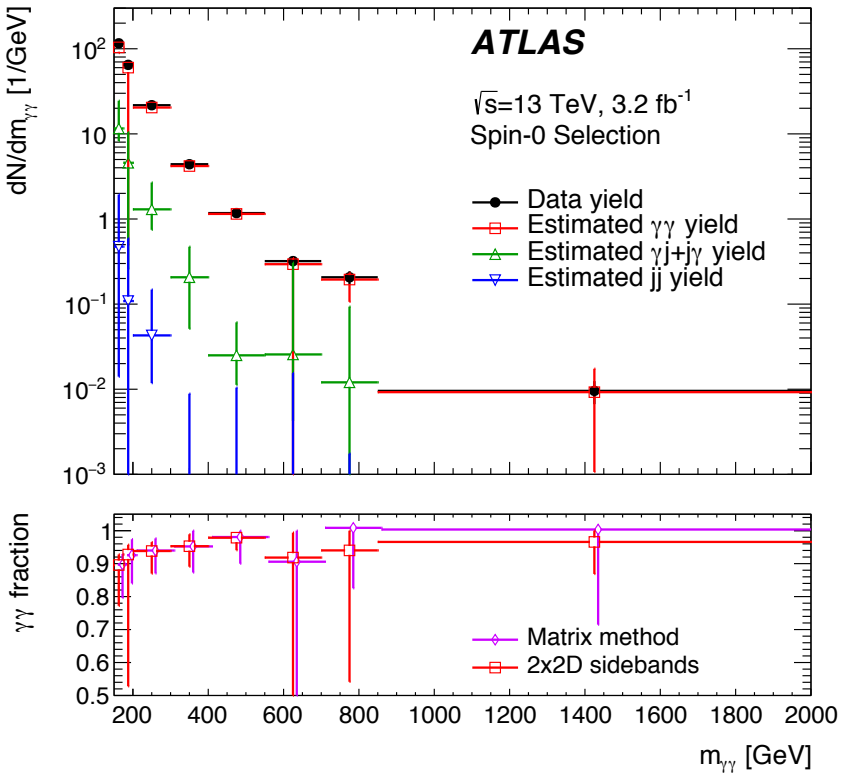

Figure 7.5: The estimated contributions to the high-mass scalar search non-resonant background in 2015 data from the $\gamma\gamma$, γ-jet, and dijet processes using the 2×2D and matrix methods.

7.2.2 Background PDF for $m_{\gamma\gamma}$

The parameterization of the non-resonant background in the search for the Standard Model Higgs boson was chosen separately for each analysis category. Multiple functional forms were considered for the background shape, including Bernstein polynomials up to seventh order, exponential functions with polynomial exponents up to three orders, and exponential functions with modified turn-on behaviors. The parameters of each function, including the overall normalization, were unconstrained and allowed to float in fits to data.

In order to choose between the analytic background PDF candidates, maximum

likelihood fits in the mass range 100 GeV $\leq m_{\gamma\gamma} \leq$ 160 GeV were performed on the high-statistics *smeared* Monte Carlo simulations of the background described in Section 4.2.3. The background model under consideration, together with the expected signal shape with a floating normalization, were fit repeatedly for a scan of the full range of m_H hypotheses (between 110 GeV and 150 GeV). At each point, the number of fitted signal events was measured. This *spurious signal* corresponded to the bias in the fitted signal yield for a particular Higgs mass hypothesis resulting from the parameterization of the background.

Candidate background functions were only considered to be viable if the measured bias on the signal yield was less than 20% of the uncertainty on the fitted signal yield and less than 10% of the expected number of signal events in the analysis category. Additionally, background models were discarded when the fits did not converge reliably. These requirements had to be satisfied for every Higgs mass hypothesis. The background model that passed all of the requirements and gave the best expected sensitivity to the Higgs boson signal was chosen.

The bias on the signal yield resulting from the background modeling was used to define a shape systematic uncertainty for the Higgs search background. Table 7.6 lists the selected background model for each of the analysis categories in the search for the Standard Model Higgs boson, along with the magnitude of the spurious signal systematic uncertainty. The implementation of the spurious signal systematic uncertainty in the likelihood model is discussed in Section 8.1.2.

The normalization of the background was represented by an unconstrained normalization parameter in the fit model, the value of which was determined by the number of events the observed data. As a consequence of this freedom in the background

Category	**Background PDF**	**Uncertainty [N_{events}]**	
		$\sqrt{s} = 7$ TeV	$\sqrt{s} = 8$ TeV
Unconverted, central, low p_{Tt}	Exp. of $\mathcal{O}(2)$ polynomial	2.1	3.0
Unconverted, central, high p_{Tt}	Exponential	0.2	0.3
Unconverted, rest, low p_{Tt}	$\mathcal{O}(4)$ polynomial	2.2	3.3
Unconverted, rest, high p_{Tt}	Exponential	0.5	0.8
Converted, central, low p_{Tt}	Exp. of $\mathcal{O}(2)$ polynomial	1.6	2.3
Converted, central, high p_{Tt}	Exponential	0.3	0.4
Converted, rest, low p_{Tt}	$\mathcal{O}(4)$ polynomial	4.6	6.8
Converted, rest, high p_{Tt}	Exponential	0.5	0.7
Converted, transition	Exp. of $\mathcal{O}(2)$ polynomial	3.2	4.6
2-jet	Exponential	0.4	0.6
Inclusive	$\mathcal{O}(4)$ polynomial	7.3	10.6

Table 7.6: The systematic uncertainty on the number of fitted signal events resulting from the background parameterization in each analysis category. The size of the uncertainty, in terms of number of events, was determined for integrated luminosities of 4.8 fb^{-1} for $\sqrt{s} = 7$ TeV data and 5.9 fb^{-1} for $\sqrt{s} = 8$ TeV data.

model, no systematic uncertainties on the background yield were necessary.

The analytic background PDF for the high-mass scalar search was selected in a similar manner to the background model in the Higgs search. As a consequence of the vastly expanded high-mass search range, different classes of functions had to be considered for the background model. A set of functions developed for dijet searches [152] was chosen to describe the invariant diphoton mass distribution at high-masses:

$$f_k[x, b, \{a_k\}] = N(1 - x^{1/3})^b \cdot x^{\sum_{j=0}^{k} a_j (\log(x))^j}, \tag{7.4}$$

where b and a_k were unconstrained parameters, N was a normalization parameter, and $x = m_{\gamma\gamma}/\sqrt{s}$. A model f_k thus corresponded to $k + 2$ free parameters, not including the normalization.

Maximum likelihood fits of the background functions were performed to background-only samples in the mass range $m_{\gamma\gamma} \geq 150$ GeV for 2015 data and $m_{\gamma\gamma} \geq 180$ GeV

for 2016 data. The background-only samples was composed of the SHERPA $\gamma\gamma$ Monte Carlo discussed in Section 4.2.3 and data-driven estimates of the γ-jet and dijet backgrounds obtained by relaxing the photon identification criteria. These samples were mixed according to the background composition measurement discussed in Section 7.2.1. The background model under consideration, together with the expected signal shape with a floating normalization, were repeatedly fitted to the background sample as the signal mass and width were scanned across the full search range (200 GeV $\leq m_X \leq$ 2400 GeV, and $\Gamma_X \geq 4$ MeV with $\Gamma_X/m_X \leq 10\%$). The signal yield resulting from signal plus-background fits to the background-only samples corresponded to the *spurious signal* bias on the signal yield measurement.

The spurious signal requirements for background functions were relaxed in the high-mass scalar search with respect to the Higgs boson search. Since the scalar signal lacked a well-defined theoretical cross-section expectation, the requirement on the expected signal yield was abandoned. The requirement that the spurious signal be less than 20% of the statistical uncertainty on the fitted signal yield was also loosened to 30% for the scalar search. Since over-fitting becomes a concern for functions with too many degrees of freedom, the background function with the fewest degrees of freedom that passed the selection criteria was chosen for the analysis. Using this procedure, the $f_{k=0}$ background PDF with two free shape parameters was chosen.

The bias on the signal yield resulting from the analytic background PDF was used to define a shape systematic uncertainty for the high-mass scalar search background. For the narrow signal-width hypothesis, the spurious signal for the selected background model was found to decrease from 18 events at $m_X = 200$ GeV to 0.012 events at $m_X = 2400$ GeV with the 2015+2016 data. Similarly, the spurious signal decreased

from 117 events at $m_X = 200$ GeV to 0.35 events at $m_X = 2400$ GeV for signals with $\Gamma_X/m_X = 10\%$. In order to define a continuous systematic uncertainty for the search, the envelope of the magnitude of the spurious signal was parameterized as a function of m_X.

The spurious signal was the only systematic uncertainty defined for the high-mass scalar search background. Additional systematic uncertainties on the background yield and shape were not necessary, since the background shape and normalization parameters were unconstrained and determined entirely *in-situ* by the observed data.

Chapter 8

Statistical methodology

This chapter describes how the observed data are characterized using profile likelihood ratio test statistics [139] in the search for the Standard Model Higgs boson in the $H \to \gamma\gamma$ channel and the search for additional scalar particles in the high-mass $\gamma\gamma$ final state. The statistical procedures implemented in both analyses are based on the recommendations provided by Ref. [153]. Section 8.1 describes the construction of a likelihood model for the signal-plus-background and background-only hypotheses that can be tested against the observed data. Profile likelihood ratio test statistics for evaluating the data under these hypotheses are discussed in Section 8.2. Pseudo-experiment and asymptotic methods for determining the sampling distributions of the test statistics are described in Sections 8.3 and 8.4, respectively. Methods for quantifying the *look elsewhere* effect and measuring the global significance of a local excess in data are mentioned in Section 8.5. Finally, the statistical procedure for parameter measurements is outlined in Section 8.6.

Maximum-likelihood fits were performed for the analyses using the RooFit library [154] in the ROOT data analysis framework [155]. The RooStats library [156]

was used to implement algorithms related to the hypothesis tests.

8.1 Likelihood model

A likelihood function, $\mathcal{L}(\text{data}|\mathcal{H})$ was used to evaluate the likelihood of a dataset given a certain hypothesis, $\mathcal{H}$. The function was composed of a statistical component, based on the Poisson probability for the observed event count with respect to the expectation, and a systematic component, based on the constraint terms associated with each source of uncertainty.

8.1.1 Statistical component of the likelihood

The number of expected signal events in the analysis was expressed in terms of the signal cross-section (σ), the branching ratio to $\gamma\gamma$ ($BR_{\gamma\gamma}$), the signal efficiency times acceptance ($\epsilon_c A_c$), and the luminosity (L) for a given category (c):

$$S_c = (\sigma \times BR_{\gamma\gamma}) \cdot \epsilon_c A_c \cdot L. \tag{8.1}$$

This model worked well for the Standard Model Higgs boson search, where the expected signal phenomenology was well understood. A theoretical cross-section was less well defined in the high-mass diphoton search, however. In that instance, it made more sense to derive results using a fiducial cross-section times branching-ratio $(\sigma \times BR_{\gamma\gamma})_{fid.}$ along with a fiducial acceptance correction factor.

The total expected number of events for a single analysis category was the sum of signal and background expectations:

$$N_c = \mu S_c + B_c, \tag{8.2}$$

where S_c represents the number of signal events and B_c represents the number of background events. The number of background events, B_c, was a free parameter that was profiled to data in each analysis. A signal strength parameter, $\mu = \sigma_{\text{observed}}/\sigma_{\text{S}}$, was used to construct a single continuous likelihood model that incorporated both the background-only and signal-plus-background hypotheses. The signal-plus-background hypothesis corresponded to the model with $\mu = 1$, while the background-only hypothesis corresponded to the model with $\mu = 0$.

In each analysis, unbinned likelihood models were profiled to the distribution of the $m_{\gamma\gamma}$ observable. Equation 8.3 expresses the statistical component of the unbinned likelihood function for k events observed in a single analysis category [153]:

$$\mathcal{L}^{c}_{\text{stat.}}(\text{data}|\mu) = k^{-1} \prod_{i}^{k} \Big(\mu S_c \cdot f_{S,c}[m_{\gamma\gamma,i}] + B_c \cdot f_{B,c}[m_{\gamma\gamma,i}] \Big) \cdot e^{-(\mu S_c + B_c)}. \tag{8.3}$$

In this equation, the normalized signal and background probability density functions (PDFs) for the $m_{\gamma\gamma}$ observable in category c are represented by $f_{S,c}[m_{\gamma\gamma}]$ and $f_{B,c}[m_{\gamma\gamma}]$, respectively. Given a hypothesis that predicts S_c, $f_{S,c}$, B_c, and $f_{B,c}$, Equation 8.3 represents the probability to observe k events with observable values of $m_{\gamma\gamma,1}, m_{\gamma\gamma,2}, ..., m_{\gamma\gamma,k}$.

For analyses with multiple categories, the statistical likelihood terms for each category were multiplied together in order to construct the full statistical likelihood, as shown in Equation 8.4:

$$\mathcal{L}_{\text{stat.}}(\text{data}|\mu) = \prod_{c}^{N_c} \mathcal{L}^{c}_{\text{stat.}}(\text{data}|\mu). \tag{8.4}$$

8.1.2 Systematic component of the likelihood

In order to incorporate theoretical and experimental systematic uncertainties in the likelihood model, the event expectation term given in Equation 8.2 was modified as shown in Equation 8.5.

$$N_c = \mu S_c(\boldsymbol{\epsilon}_S, \boldsymbol{\delta}_S) + B_c(\boldsymbol{\epsilon}_B, \boldsymbol{\delta}_B) + N_{\text{spur},c} \cdot \delta_{\text{spur},c}. \tag{8.5}$$

In this equation, $\boldsymbol{\epsilon}_S$ represents the relative uncertainties from all of the systematic uncertainties influencing the signal yield, while $\boldsymbol{\delta}_S$ represents the nuisance parameters associated with those same systematic uncertainties. The same applies for $\boldsymbol{\epsilon}_B$ and $\boldsymbol{\delta}_B$ with respect to the background. The *spurious signal* systematic described in Section 7.2.2 was implemented by adding the term $(N_{\text{spur},c} \cdot \delta_{\text{spur},c})$, where $N_{\text{spur},c}$ represents the number of spurious signal events in category c. The values of the relative uncertainties, $\boldsymbol{\epsilon}$, were know *a priori* from studies of the systematics, while the values of the nuisance parameters, $\boldsymbol{\delta}$, were obtained by profiling data.

In addition to influencing the expected event yield, sources of uncertainty affected the expected distribution of the $m_{\gamma\gamma}$ observable. For example, the photon energy scale systematic uncertainty affected the position of the signal peak in $m_{\gamma\gamma}$. The signal and background PDFs were generalized to the forms $f_{S,c}[m_{\gamma\gamma}, \boldsymbol{\epsilon}_S, \boldsymbol{\delta}_S]$ and $f_{B,c}[m_{\gamma\gamma}, \boldsymbol{\epsilon}_B, \boldsymbol{\delta}_B]$.

Systematic uncertainties were incorporated into the likelihood model via response functions that were multiplied with the affected model parameters. In the case of Gaussian systematic uncertainties, the response functions were of the form $(1 + \epsilon_i \cdot \delta_i)$. For log-normal systematic uncertainties, the response functions were of

the form $e^{\ln(1+\epsilon_i \cdot \delta_i)}$. Log-normal systematics were used in cases where negative values for the affected parameter did not make sense. Resolution uncertainties used log-normal systematics, for example, since negative resolutions are unphysical.

Nuisance parameters associated with uncertainties were constrained by Gaussian PDFs, represented by $\mathcal{G}_i(m_i|\delta_i)$ for the i^{th} source of uncertainty. The constraint terms were incorporated in the full likelihood model $\mathcal{L}$ via multiplication, as shown in Equation 8.6:

$$\mathcal{L} = \mathcal{L}_{\text{stat.}} \cdot \prod_l \mathcal{G}_i(m_i|\delta_i), \text{ where } \mathcal{G}_i(m_i|\delta_i) = \frac{1}{\sqrt{2\pi}} e^{-\frac{1}{2}(m_i-\delta_i)^2}. \tag{8.6}$$

In this equation, m_i represents the auxiliary measurement of the i^{th} systematic uncertainty that provides the nominal value of the systematic uncertainty. As before, δ_l^S represents the nuisance parameter corresponding to that systematic uncertainty. The constraint term introduced a likelihood penalty when the nuisance parameter δ_i was pulled to a very different value in data than the associated auxiliary measurement m_i.

8.2 Hypothesis tests

8.2.1 Profile likelihood ratio

The compatibility of observed data with various hypotheses was compared using the profile likelihood ratio [139]:

$$\lambda(\mu) = \frac{\mathcal{L}(\text{data}|\mu, \hat{\hat{\boldsymbol{\theta}}}_\mu)}{\mathcal{L}(\text{data}|\hat{\mu}, \hat{\boldsymbol{\theta}})}. \tag{8.7}$$

In this equation, $\hat{\mu}$ and $\hat{\boldsymbol{\theta}}$ represent the global maximum-likelihood values for the signal strength μ and the nuisance parameter set $\boldsymbol{\theta}$, respectively. The $\hat{\hat{\boldsymbol{\theta}}}_\mu$ parameter

corresponds to the conditional maximum-likelihood values of the nuisance parameters, given the signal strength μ.

The likelihood ratio $\lambda(\mu)$ compares two hypotheses. The numerator likelihood, $\mathcal{L}(\text{data}|\mu, \hat{\hat{\boldsymbol{\theta}}}_\mu)$, corresponds to a fixed-μ hypothesis: $\mu = 1$ corresponds to the signal-plus-background hypothesis while $\mu = 0$ corresponds to the background-only hypothesis. The denominator likelihood, $\mathcal{L}(\text{data}|\hat{\mu}, \hat{\boldsymbol{\theta}})$, corresponds to the maximum-likelihood hypothesis in which μ is free to assume the value preferred by data. Two fits were thus required to construct the likelihood ratio: one conditional maximum-likelihood fit for the numerator in which μ was fixed to the value of interest, and one maximum-likelihood fit for the denominator in which the signal strength parameter was allowed to float.

In analyses with small sample sizes such as the high-mass diphoton search, a positive signal strength was required in order to prevent unphysical negative PDFs from entering the likelihood. The modified likelihood ratio $\tilde{\lambda}(\mu)$ imposed the $\mu \geq 0$ requirement:

$$\tilde{\lambda}(\mu) = \begin{cases} \frac{\mathcal{L}(\text{data}|\mu, \hat{\hat{\boldsymbol{\theta}}}_\mu)}{\mathcal{L}(\text{data}|\hat{\mu}, \hat{\boldsymbol{\theta}})} & \hat{\mu} \geq 0, \\ \frac{\mathcal{L}(\text{data}|\mu, \hat{\hat{\boldsymbol{\theta}}}_\mu)}{\mathcal{L}(\text{data}|0, \hat{\hat{\boldsymbol{\theta}}}_0)} & \hat{\mu} < 0. \end{cases} \tag{8.8}$$

Equation 8.8 accounts for the fact that the best agreement between data and the likelihood model would be found with $\mu = 0$ when the data would prefer $\hat{\mu} < 0$. The variable $\hat{\hat{\boldsymbol{\theta}}}_0$ represents the conditional maximum-likelihood values of the nuisance parameters when $\mu = 0$.

8.2.2 q_μ test-statistic

The q_μ test statistic, shown in Equation 8.9, is based on the profile likelihood ratio and was used to determine the compatibility of the data with a signal-plus-background hypothesis.

$$q_\mu = \begin{cases} -2\ln\lambda(\mu) & \hat{\mu} \leq \mu \\ 0 & \hat{\mu} > \mu. \end{cases} = \begin{cases} -2\ln\frac{\mathcal{L}(\mu,\hat{\hat{\boldsymbol{\theta}}}_\mu)}{\mathcal{L}(\hat{\mu},\hat{\boldsymbol{\theta}})} & \hat{\mu} \leq \mu, \\ 0 & \hat{\mu} > \mu. \end{cases} \tag{8.9}$$

q_μ is small if the maximum-likelihood fit to data favors the signal-plus-background hypothesis and is large if the maximum-likelihood fit to data favors the background-only hypothesis. The q_μ test-statistic was structured so that fluctuations of the dataset with profiled signal strengths greater than the signal strength of the tested hypothesis were considered compatible with the signal-plus-background model ($q_\mu = 0$ if $\hat{\mu} > \mu$).

For the high-mass search, where $\mu > 0$ was required, the test-statistic $\tilde{q}_\mu$ was defined using the $\tilde{\lambda}(\mu)$ profile likelihood ratio:

$$\tilde{q}_\mu = \begin{cases} -2\ln\tilde{\lambda}(\mu) & \hat{\mu} \leq \mu, \\ 0 & \hat{\mu} > \mu, \end{cases} = \begin{cases} -2\ln\frac{\mathcal{L}(\mu,\hat{\hat{\boldsymbol{\theta}}}_\mu)}{\mathcal{L}(0,\hat{\hat{\boldsymbol{\theta}}}_0)} & \hat{\mu} < 0, \\ -2\ln\frac{\mathcal{L}(\mu,\hat{\hat{\boldsymbol{\theta}}}_\mu)}{\mathcal{L}(\hat{\mu},\hat{\boldsymbol{\theta}})} & 0 \leq \hat{\mu} \leq \mu, \\ 0 & \hat{\mu} > \mu. \end{cases} \tag{8.10}$$

Strong background-like fluctuations of the data, where $\hat{\mu} < 0$, would have a truncated $\tilde{q}_\mu$ value ($\tilde{q}_\mu < q_\mu$).

8.2.3 CL_s exclusion limits

Exclusion limits on a signal hypothesis were computed for the data using the $\tilde{q}_\mu$ test-statistic. The normalized distribution of $\tilde{q}_\mu$ under the signal-plus-background hypothesis – $f(\tilde{q}_\mu|\mu, \hat{\hat{\boldsymbol{\theta}}}_{\mu,\text{obs.}})$ – and the normalized distribution of $\tilde{q}_\mu$ under the background-only hypothesis – $f(\tilde{q}_\mu|0, \hat{\hat{\boldsymbol{\theta}}}_{0,\text{obs.}})$ – were integrated to calculate p_μ and p_B, respectively. The sampling distributions of the test statistics were determined via pseudo-experiment or asymptotic methods, as discussed in Sections 8.3 and 8.4. The $\tilde{q}_\mu$ distributions can be thought of as the distributions of the test statistic that would result from multiple repetitions of the experiment given a certain hypothesis, in which statistical variations of the observed data and fluctuations in the values of the systematic uncertainties affect the outcome.

The normalized distribution of $\tilde{q}_\mu$ generated under the signal-plus-background hypothesis was integrated to compute p_μ for the observation:

$$p_\mu = \int_{\tilde{q}_{\mu,\text{obs}}}^{\infty} f(\tilde{q}_\mu|\mu, \hat{\hat{\boldsymbol{\theta}}}_{\mu,\text{obs}}) d\tilde{q}_\mu. \tag{8.11}$$

Equation 8.11 represents the fraction of experiments performed on signal-plus-background data that gave a value of $\tilde{q}_\mu$ greater than or equal to the observed value. This corresponds to the fraction of experiments conducted under the signal-plus-background hypothesis that showed worse agreement with that hypothesis. From a frequentist perspective, p_μ can be interpreted as the probability that the observed data were generated by the signal-plus-background hypothesis. $p_{\mu=1}$ is sometimes quoted as the CL_{S+B} limit.

Similarly, the normalized distribution of $\tilde{q}_\mu$ generated under the background-only

hypothesis was integrated to compute p_B for the observation:

$$p_B = \int_{-\infty}^{\tilde{q}_{\mu,\mathrm{obs}}} f(\tilde{q}_\mu|0,\hat{\hat{\boldsymbol{\theta}}}_{0,\mathrm{obs}})d\tilde{q}_\mu. \tag{8.12}$$

Equation 8.12 represents the fraction of experiments performed on background-only data that gave a value of $\tilde{q}_\mu$ less than or equal to the observed value. This corresponds to the fraction of experiments conducted under the background-only hypothesis that showed better agreement with the signal-plus-background hypothesis. p_B can be interpreted as the probability that the observed data were generated by the background-only hypothesis. $1 - p_B$ is sometimes referred to as the background-only hypothesis confidence level, or CL_B.

The search results in this thesis are presented in terms of exclusion limits using the CL_s method [157, 158]. Equation 8.13 defines the CL_s limit:

$$CL_S(\mu) = \frac{p_\mu}{1 - p_B}. \tag{8.13}$$

A hypothesis with a specific value of the signal strength, μ, was excluded at 95% CL when $CL_s(\mu) < 0.05$. In the search for the Standard Model Higgs boson, a particular value of m_H was excluded at 95% CL when the $\mu = 1$ hypothesis at that mass was excluded at 95% CL. Exclusions were performed in terms of $(\sigma \times BR_{\gamma\gamma})_{fid.}$ for the high-mass diphoton search, where an expectation for $\mu = 1$ was not well-defined.

The expected CL_s exclusion was calculated in a similar manner to the observed CL_s, except that the median value of $\tilde{q}_\mu$ under the background-only hypothesis was used instead of the observed value of $\tilde{q}_\mu$. Equations 8.11 and 8.12 were modified by substituting $\tilde{q}_{\mu,\mathrm{exp}}$ for $\tilde{q}_{\mu,\mathrm{obs}}$ in the integration limits, where $\tilde{q}_{\mu,\mathrm{exp}}$ was the me-

dian of $f(\tilde{q}_\mu|0,\hat{\hat{\boldsymbol{\theta}}}_{0,\text{obs}})$. This convention reflects the requirement that $p_B = 0.5$ for the background-only expectation. A procedure for calculating the $\pm1\sigma$ and $\pm2\sigma$ uncertainty bands on the expected limit is explained in depth in Ref. [159].

8.2.4 q_0 test-statistic

The compatibility of the data with the background-only hypothesis was computed using the q_0 profile likelihood ratio test-statistic:

$$q_0 = \begin{cases} -2\ln\lambda(0) & \hat{\mu} \geq 0, \\ 0 & \hat{\mu} < 0. \end{cases} \tag{8.14}$$

The q_0 test-statistic is structured so that downward fluctuations of the dataset are compatible with the background-only hypothesis. Greater compatibility of the data and the background-only hypothesis are represented by smaller values of q_0, whereas signal-like fluctuations in the data that are less compatible with the background-only hypothesis correspond to larger values of q_0.

8.2.5 p_0 probability

The p_0 probability was used to quantify the level of agreement between the observed data and the background-only hypothesis. It was calculated by integrating the normalized distribution of q_0 generated under the background-only hypothesis – $f(q_0|0,\hat{\hat{\boldsymbol{\theta}}}_{0,\text{obs}})$ – from the observed value of q_0 to infinity, as in Equation 8.15:

$$p_0 = \int_{q_{0,\text{obs}}}^{\infty} f(q_0|0,\hat{\hat{\boldsymbol{\theta}}}_{0,\text{obs}})dq_0. \tag{8.15}$$

p_0 represents the fraction of experiments performed on background-only data that give a value of q_0 greater than or equal to the observed value. From a frequentist perspective, p_0 can be interpreted as the probability that the observed data represent a fluctuation of the background-only hypothesis. To discover a new phenomenon, the background-only hypothesis must be tested against the alternative signal-plus-background hypothesis and rejected at the level of 5 standard deviations, corresponding to $p_0 < 2.87 \times 10^{-7}$.

8.3 Pseudo-experiment ensembles

The sampling distributions of the $\tilde{q}_\mu$ and q_0 test-statistics under the signal-plus-background and background-only hypotheses were needed in order to calculate CL_s exclusion limits and p_0 probabilities. Pseudo-experiment ensembles provided one method of constructing the $f(\tilde{q}_\mu)$ and $f(q_0)$ distributions.

The full likelihood model (Equation 8.6) was used to generate randomized simulated datasets, called toy Monte Carlo. In order to generate a dataset for a particular hypothesis μ', a conditional maximum-likelihood fit was performed on data that maximized the corresponding likelihood model, $\mathcal{L}(\mu', \hat{\hat{\boldsymbol{\theta}}}_{\mu',obs})$. This fit provided the conditional maximum-likelihood values of the nuisance parameters, $\hat{\hat{\boldsymbol{\theta}}}_{\mu',obs}$, that were used to randomize the associated auxiliary measurement terms in each toy Monte Carlo dataset according to the associated constraint PDF. Auxiliary measurement randomization was implemented for the purpose of propagating variations in the data due to sources of uncertainty into the pseudo-data ensemble. For each toy Monte Carlo dataset, the distribution of the $m_{\gamma\gamma}$ observable parameter was also generated randomly according to the PDF defined by the likelihood model.

Once a toy Monte Carlo dataset was generated, the corresponding values of $\tilde{q}_\mu$ or q_0 were obtained by profiling the likelihood. A distribution of the test statistics was build by repeating this procedure on thousands of randomized toy Monte Carlo datasets. In order to compute the CL_s exclusion, toy Monte Carlo datasets were generated for the signal-plus-background and background-only hypotheses, and the $\tilde{q}_\mu$ distributions were built for both ($f(\tilde{q}_\mu|\mu, \hat{\hat{\boldsymbol{\theta}}}_{\mu,\text{obs.}})$ and $f(\tilde{q}_\mu|0, \hat{\hat{\boldsymbol{\theta}}}_{0,\text{obs.}})$). The p_0 calculation only required the generation of toy Monte Carlo datasets corresponding to the background-only hypothesis, which were used to construct $f(q_0|0, \hat{\hat{\boldsymbol{\theta}}}_{0,\text{obs}})$.

8.4 Asymptotic methods

Asymptotic forms of the $f(\tilde{q}_\mu|\mu)$ and $f(q_0|0)$ sampling distributions were introduced in Ref. [139] and were used for both the search for the Standard Model Higgs boson and the search for high-mass diphoton resonances. The derivations relied on approximate forms of the profile likelihood ratio $-2\ln\lambda$ by Wilks [160] and Wald [161] that contain corrections of $\mathcal{O}(1/\sqrt{N})$, where N is the sample size. Thus, the asymptotic test-statistic approximations are valid for very large datasets but require validation in low-statistics search regions.

The sampling distribution $f(q_0|0)$ was approximated by two components: a χ^2 distribution for a single degree of freedom and a delta function centered at zero.

$$f(q_0|0) = \frac{1}{2}\delta(q_0) + \frac{1}{2}\frac{e^{-q_0/2}}{\sqrt{2\pi q_0}}. \tag{8.16}$$

The corresponding p_0 probability was related to the Gaussian cumulative distribution function Φ:

$$p_{0,obs.} = 1 - \Phi(\sqrt{q_{0,obs.}}). \tag{8.17}$$

Similarly, the sampling distribution $f(\tilde{q}_\mu|\mu')$ with $\mu' \neq \mu$ was approximated:

$$f(\tilde{q}_\mu|\mu') = \Phi(\tfrac{\mu'-\mu}{\sigma})\delta(\tilde{q}_\mu) + \begin{cases} \frac{1}{2}\frac{1}{\sqrt{2\pi}}\frac{1}{\sqrt{\tilde{q}_\mu}}e^{-\frac{1}{2}\left(\sqrt{\tilde{q}_\mu}-\frac{\mu'-\mu}{\sigma}\right)^2} & 0 < \tilde{q}_\mu \leq \mu^2/\sigma^2, \\ \frac{1}{\sqrt{2\pi}(2\mu/\sigma)}e^{-\frac{1}{2}\left(\frac{(\tilde{q}_\mu-(\mu^2-2\mu\mu')/\sigma^2)^2}{(2\mu/\sigma)^2}\right)} & \tilde{q}_\mu > \mu^2/\sigma^2. \end{cases} \tag{8.18}$$

σ represents the standard deviation of the expected distribution of $\hat{\mu}$ with a mean value of μ' in Equation 8.18. It was calculated using Asimov data [139]. The cumulative distribution function for $f(\tilde{q}_\mu|\mu')$ was given by the expression:

$$F(\tilde{q}_\mu|\mu') = \begin{cases} \Phi\left(\sqrt{\tilde{q}_\mu} - \frac{\mu-\mu'}{\sigma}\right) & 0 < \tilde{q}_\mu \leq \mu^2/\sigma^2, \\ \Phi\left(\frac{\tilde{q}_\mu-(\mu^2-2\mu\mu')/\sigma^2}{2\mu/\sigma}\right) & \tilde{q}_\mu > \mu^2/\sigma^2. \end{cases} \tag{8.19}$$

The values of p_μ and p_B necessary for the CL_S method were calculated using $F(\tilde{q}_\mu|\mu')$ as shown in Equations 8.20 and 8.21:

$$p_\mu = 1 - F(\tilde{q}_\mu|\mu), \tag{8.20}$$

$$p_B = F(\tilde{q}_\mu|0). \tag{8.21}$$

Asymptotic formulae were advantageous because they significantly reduced the CL_s and p_0 computation times and became more accurate as the sample sizes increased. However, the high-statistics requirement of Wilks' theorem [160] necessitated the validation of the accuracy of the asymptotic methods using pseudo-experiment

ensembles. This was done for $f(\tilde{q}_\mu|\mu)$ and $f(q_0|0)$ in both the search for the Standard Model Higgs boson and the search for high-mass diphoton resonances using the procedure outlined in Ref. [159].

8.5 Look-elsewhere effect and global significance

The p_0 probability discussed in Section 8.2.5 corresponds to a *local* probability: the probability of the background creating a signal-like fluctuation at a single point in the signal space. However, searches often take place over a range of signal parameter values. For instance, the search for the Standard Model Higgs boson was conducted over a large range of m_H values. The search for high-mass diphoton resonances was conducted over an even larger range of m_X as well as a range of signal widths Γ_X. When this large space of partially correlated searches is considered, the probability that the background will fluctuate to produce any given local p_0 value is actually significantly higher ($p_0^{\text{global}} \geq p_0^{\text{local}}$). This is the so-called *look elsewhere* effect.

Several methods exist to quantify the global p_0 probability. A brute force approach involves generating large pseudo-experiment ensembles, fitting them with every signal-plus-background hypothesis in the search, and integrating the distribution of the minimum p_0 values profiled to each pseudo-experiment from $p_{0,\text{obs.}}$ to ∞ to calculate the global p_0. This approach is outlined in greater detail in Appendix A, and was used as the baseline method for the high-mass diphoton search.

The search for the Standard Model Higgs boson used the trial factor method [162], which approximates the global Z_0 for searches in one dimension. In this method, a small number of pseudo-experiments were generated in order to calculate a trial factor related to the average number of times the observed local-p_0 curve in the one-

dimensional search crossed the expected local-p_0 curve. This trial factor was used to calculate the global p_0 corresponding to the minimum local-p_0 observed in the search.

Another method based on the properties of random fields can also be used to determine the global significance of a search in multiple dimensions [163]. It can be thought of as a generalization of the trial factor approach to higher dimensions, and also requires a small batch of pseudo-experiments for tuning two extrapolation parameters. The random field method was used as a cross-check for the high-mass diphoton search. Both the trial factor and random field approximations performed well for large global significances but diverged from the expected result when the global significance was small. This is generally not a problem, as the global significance is only of interest when searches uncover large deviations from the background-only hypothesis.

8.6 Parameter measurements

In order to measure one or more parameters of the likelihood model, the profile likelihood ratio from Equation 8.7 was extended:

$$\lambda(\mu) = \frac{\mathcal{L}(\text{data}|\boldsymbol{\nu}, \hat{\hat{\boldsymbol{\theta}}}_{\boldsymbol{\nu}})}{\mathcal{L}(\text{data}|\hat{\boldsymbol{\nu}}, \hat{\boldsymbol{\theta}})}. \tag{8.22}$$

$\boldsymbol{\nu}$ represents the set of parameters of interest for a particular hypothesis, while $\hat{\boldsymbol{\nu}}$ represents the maximum-likelihood values of the nuisance parameters. In the simple case of a signal strength measurement, $\boldsymbol{\nu} = (\mu)$ as in Equation 8.7. For a two-dimensional measurement of the Higgs mass and Higgs signal strength, $\boldsymbol{\nu} = (\mu, m_H)$.

The profile likelihood ratio for multiple parameters of interest from Equation 8.22 was used to construct a test-statistic t_μ:

$$t_\mu = -2 \ln \lambda(\mu). \tag{8.23}$$

As with q_0 and $\tilde{q}_\mu$, an asymptotic form of the sampling distribution was derived [139]. For one parameter of interest,

$$f(t_\mu|\mu) = \frac{1}{\sqrt{2\pi}} \frac{1}{\sqrt{t_\mu}} e^{-\frac{1}{2}t_\mu}. \tag{8.24}$$

For multiple parameters of interest, the asymptotic sampling distribution follows a χ^2 distribution for n degrees of freedom, where n is the dimensionality of $\hat{\boldsymbol{\nu}}$. The one-dimensional sampling distribution has a cumulative distribution function given by:

$$F(t_\mu|\mu) = 2\Phi(\sqrt{t_\mu}) - 1. \tag{8.25}$$

The maximum-likelihood values of the parameters of interest, $\hat{\boldsymbol{\nu}}$, were used for the central values of the parameter measurements. The standard deviations were found by solving for $-2 \ln \lambda(\mu) = 1$ [160]. In practice, this was done by performing a likelihood scan in the space of $\boldsymbol{\nu}$ and looking for the points $\boldsymbol{\nu}_-$ and $\boldsymbol{\nu}_+$ where the likelihood curve crossed 1. For a single parameter such as μ, the measurement and uncertainty were quoted as $\hat{\mu}^{+(\mu_+ - \hat{\mu})}_{-(\hat{\mu} - \mu_-)}$.

Chapter 9

Results

9.1 Search for the Standard Model Higgs boson

This section summarizes the results of the search for the Standard Model Higgs boson in the diphoton decay channel using 4.8 fb^{-1} of data collected at a center-of-mass energy of $\sqrt{s} = 7$ TeV and 5.9 fb^{-1} of data collected at $\sqrt{s} = 8$ TeV during 2011 and 2012. Section 9.1.1 presents the observed diphoton invariant mass distributions for selected events from data, Section 9.1.2 provides the compatibility of the observations with the background-only hypothesis, Section 9.1.3 gives the exclusion limits on Standard Model Higgs bosons calculated using the data, and Section 9.1.4 shows the signal strength of the observed excess of events. Finally, Section 9.1.5 discusses the statistical combination of the $H \to \gamma\gamma$ results with observations from the $H \to ZZ^* \to 4l$ and $H \to WW^* \to l\nu l\nu$ channels.

9.1.1 Invariant mass spectra

The invariant mass distributions for selected events in each analysis category of the $H \to \gamma\gamma$ search are shown in Figures 9.1 - 9.10. Each histogram compares the observed data to the background-only hypothesis, illustrated with a solid red line, and the signal-plus-background hypothesis for a Higgs mass of 126.5 GeV, illustrated with a dashed red line. Sub-figures provide the background-subtracted distribution of invariant masses.

Figure 9.11 shows the inclusive invariant mass distribution, which includes all of the analysis channels for both center-of-mass energies. Figure 9.12 shows the inclusive invariant mass distribution after each event is given a weight, w_i, based on the signal-to-background ratio (S_i/B_i) of the category (index i) into which it was sorted: $w_i = \ln(1 + \frac{S_i}{B_i})$. In these figures, the inclusive background is modeled by a fourth-order Bernstein polynomial function. The Higgs signal hypothesis is superimposed on the background for a hypothetical Higgs mass of $m_H = 126.5$ GeV. Both distributions reveal an excess of events near this Higgs boson mass, and agreement is qualitatively better between the data and the signal-plus-background model than the background-only model.

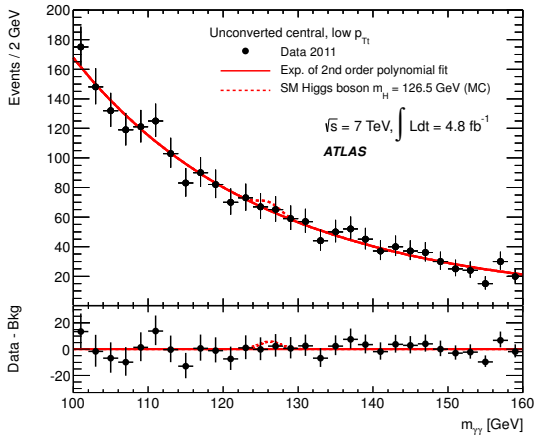

(a) $\sqrt{s} = 7$ TeV data.

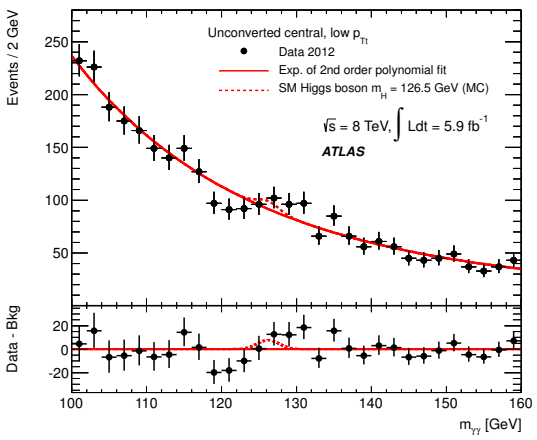

(b) $\sqrt{s} = 8$ TeV data.

Figure 9.1: The diphoton invariant mass spectrum for selected events in the unconverted, central, low-p_{Tt} category for 2011 and 2012 data.

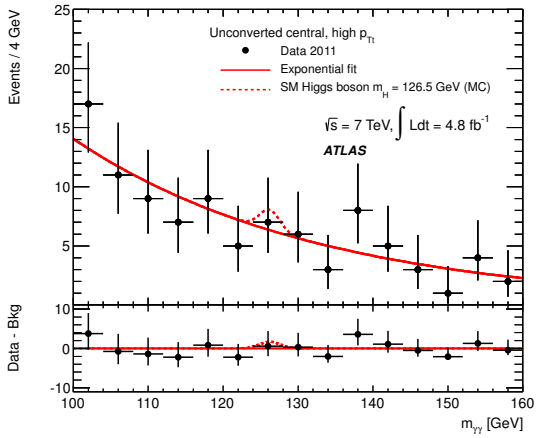

(a) $\sqrt{s} = 7$ TeV data.

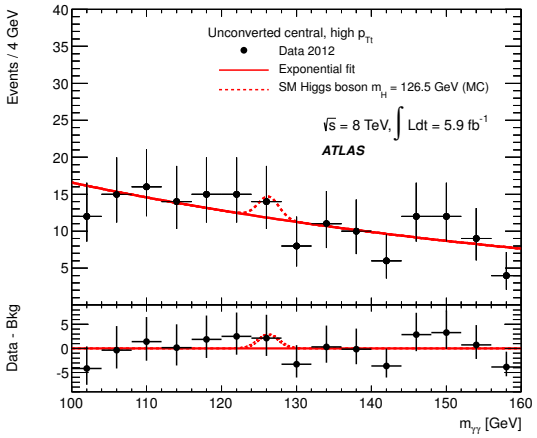

(b) $\sqrt{s} = 8$ TeV data.

Figure 9.2: The diphoton invariant mass spectrum for selected events in the unconverted, central, high-p_{Tt} category for 2011 and 2012 data.

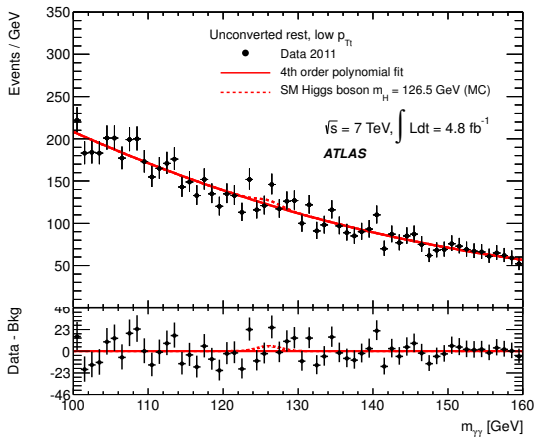

(a) $\sqrt{s} = 7$ TeV data.

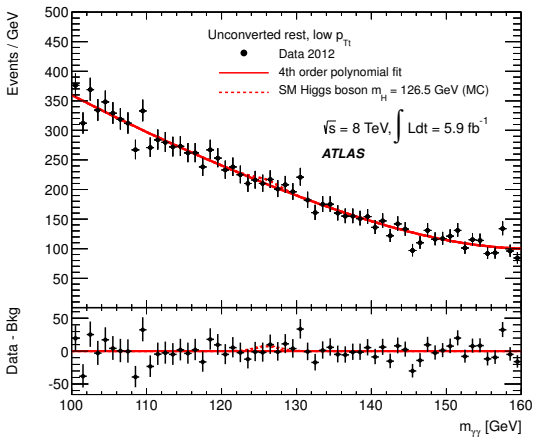

(b) $\sqrt{s} = 8$ TeV data.

Figure 9.3: The diphoton invariant mass spectrum for selected events in the unconverted, rest, low-p_{Tt} category for 2011 and 2012 data.

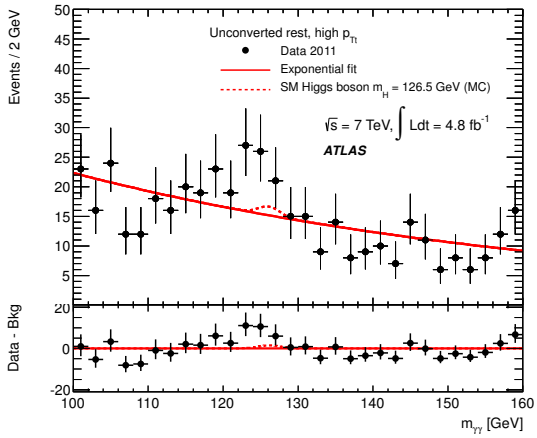

(a) $\sqrt{s} = 7$ TeV data.

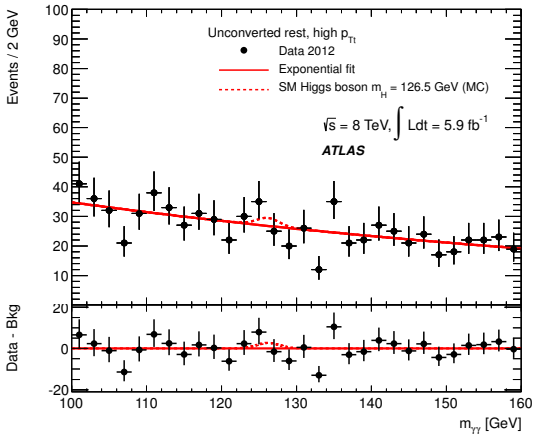

(b) $\sqrt{s} = 8$ TeV data.

Figure 9.4: The diphoton invariant mass spectrum for selected events in the unconverted, rest, high-p_{Tt} category for 2011 and 2012 data.

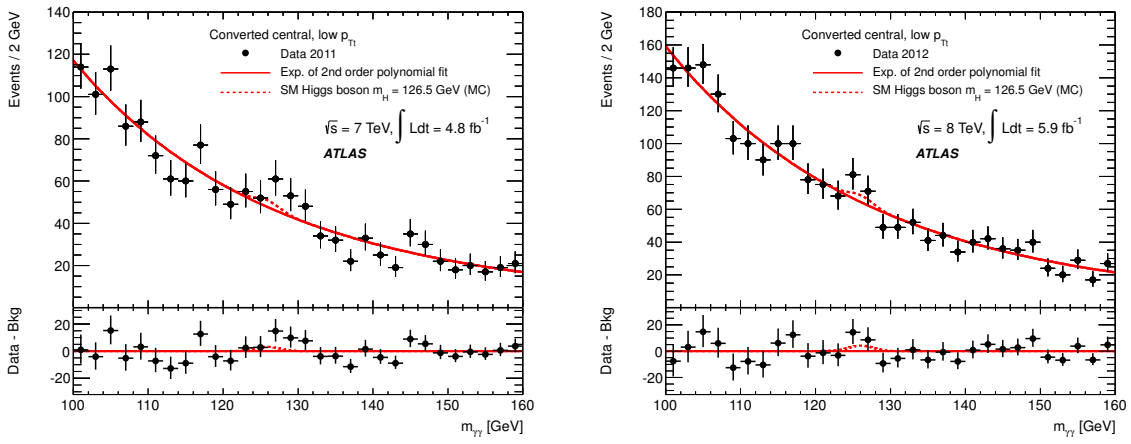

(a) $\sqrt{s} = 7$ TeV data. (b) $\sqrt{s} = 8$ TeV data.

Figure 9.5: The diphoton invariant mass spectrum for selected events in the converted, central, low-p_{Tt} category for 2011 and 2012 data.

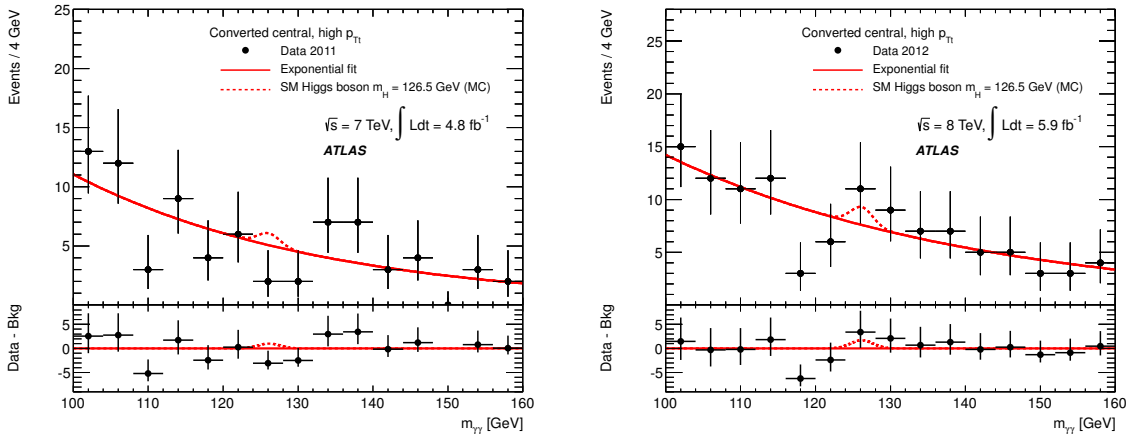

(a) $\sqrt{s} = 7$ TeV data. (b) $\sqrt{s} = 8$ TeV data.

Figure 9.6: The diphoton invariant mass spectrum for selected events in the converted, central, high-p_{Tt} category for 2011 and 2012 data.

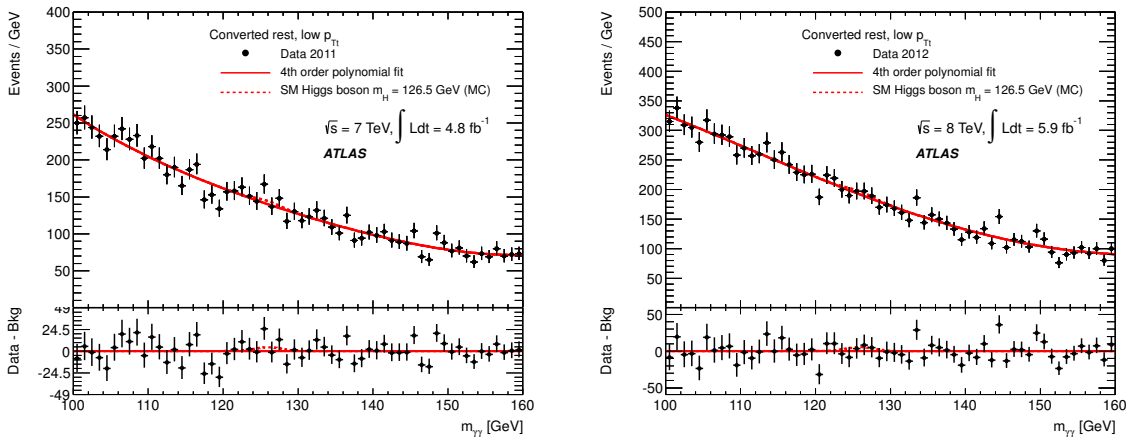

(a) $\sqrt{s} = 7$ TeV data. (b) $\sqrt{s} = 8$ TeV data.

Figure 9.7: The diphoton invariant mass spectrum for selected events in the converted, rest, low-p_{Tt} category for 2011 and 2012 data.

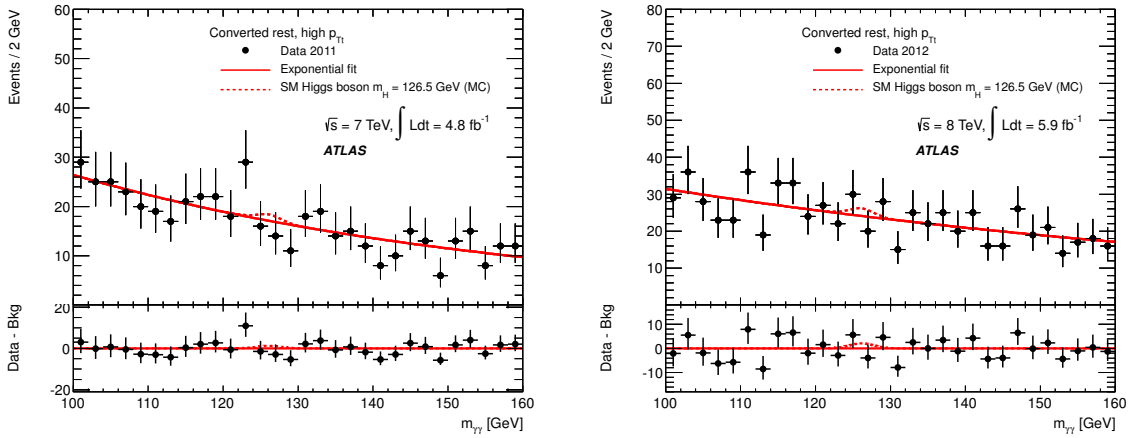

(a) $\sqrt{s} = 7$ TeV data. (b) $\sqrt{s} = 8$ TeV data.

Figure 9.8: The diphoton invariant mass spectrum for selected events in the converted, rest, high-p_{Tt} category for 2011 and 2012 data.

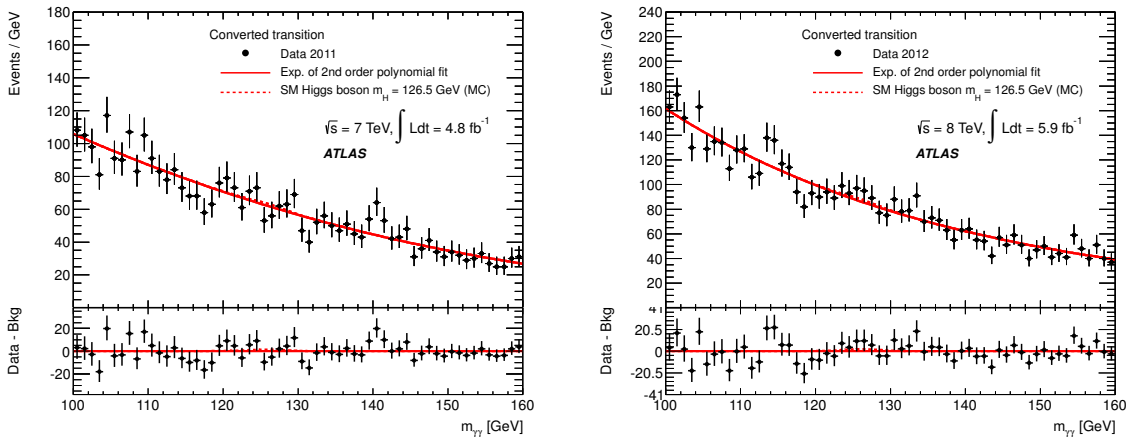

(a) $\sqrt{s} = 7$ TeV data. (b) $\sqrt{s} = 8$ TeV data.

Figure 9.9: The diphoton invariant mass spectrum for selected events in the converted, transition category for 2011 and 2012 data.

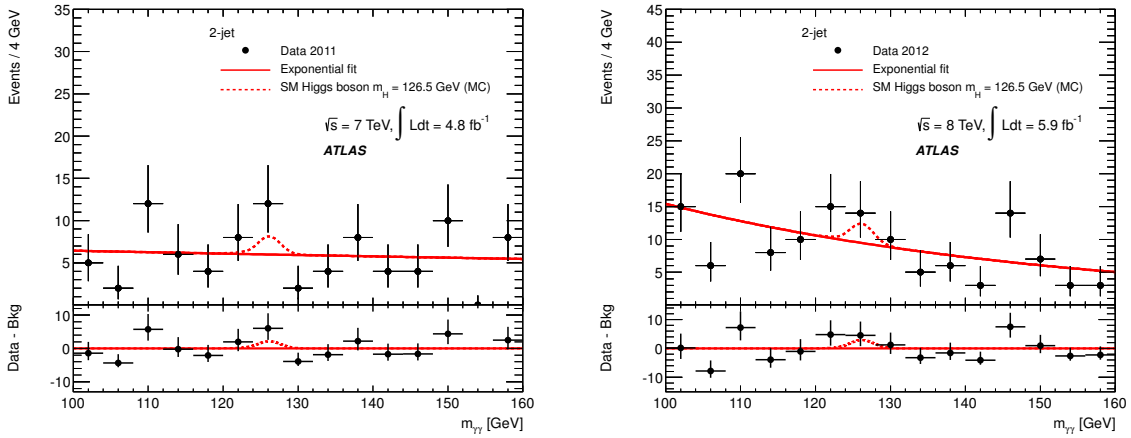

(a) $\sqrt{s} = 7$ TeV data. (b) $\sqrt{s} = 8$ TeV data.

Figure 9.10: The diphoton invariant mass spectrum for selected events in the two-jet category for 2011 and 2012 data.

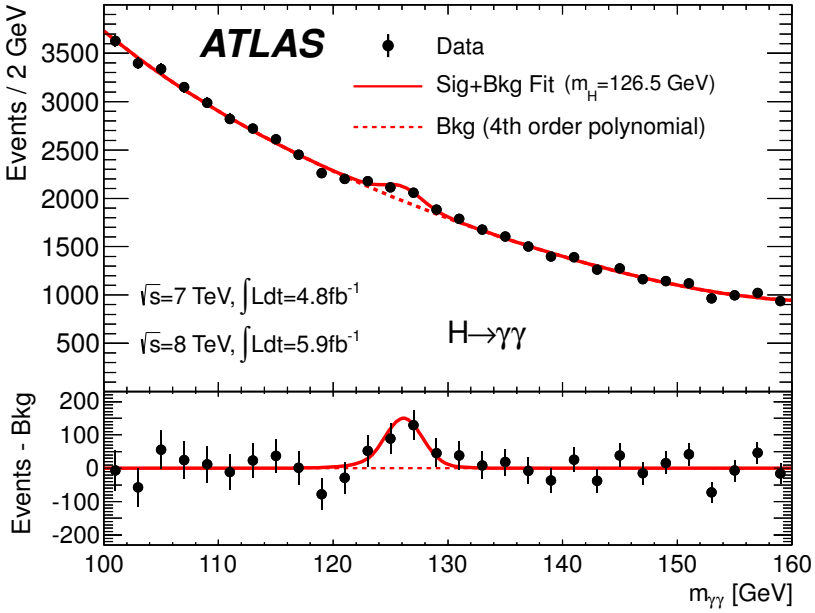

Figure 9.11: The unweighted distribution of diphoton invariant masses for selected events in the combined $\sqrt{s} = 7$ TeV and $\sqrt{s} = 8$ TeV dataset.

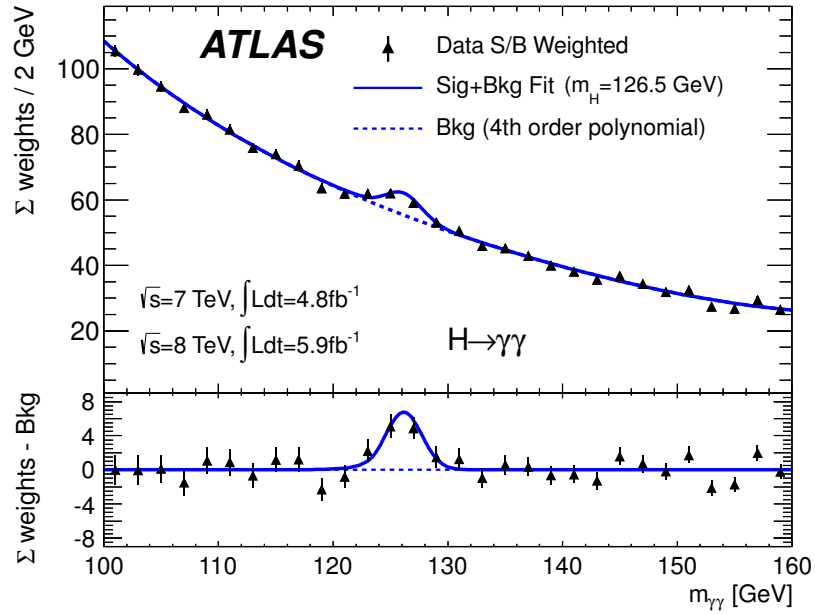

Figure 9.12: The weighted distribution of diphoton invariant masses for selected events in the combined $\sqrt{s} = 7$ TeV and $\sqrt{s} = 8$ TeV dataset. Data are weighted according to the signal-to-background ratio in the associated analysis category.

9.1.2 Compatibility with the background-only hypothesis

In order to provide a more quantitative assessment of the data, the p_0 test described in Section 8.2.5 was used to evaluate the compatibility of the observed data with the background-only hypothesis. A scan of the p_0 probability was performed for the range of hypothetical Higgs boson masses 110 GeV $\leq m_H \leq$ 150 GeV with a step size of 0.5 GeV. Figure 9.13 shows the results of the scans for the individual analysis categories separately for each center-of-mass energy. The plots demonstrate that multiple categories contribute to the excess of events observed near a mass of 126.5 GeV. The p_0 results obtained by combining all of the analysis categories and the datasets from $\sqrt{s} = 7$ TeV and $\sqrt{s} = 8$ TeV are provided in Figure 9.14. The observed p_0 values, shown with solid curves, are compared to the expected p_0 values for Higgs bosons as a function of Higgs mass, shown with dashed curves.

An excess of events, corresponding to a local significance of 4.7 standard deviations, is observed in the search for the Standard Model Higgs boson using the $\gamma\gamma$ decay channel for a signal mass of $m_H = 126.5$ GeV. This result is driven by separate excesses of 3.4 standard deviations at $m_H = 126$ GeV in the $\sqrt{s} = 7$ TeV data and 3.2 standard deviations at $m_H = 127$ GeV in the $\sqrt{s} = 8$ TeV data. The impact of energy-scale systematic uncertainties on the result is shown with circled points near the minima of the p_0 curves in Figure 9.14. When the energy scale systematics are incorporated in the fits, the significance of the excess in the combined dataset drops to 4.5 standard deviations. The range of compatible Higgs boson mass values also increases, as demonstrated by the broadening of the p_0 curves near the minima.

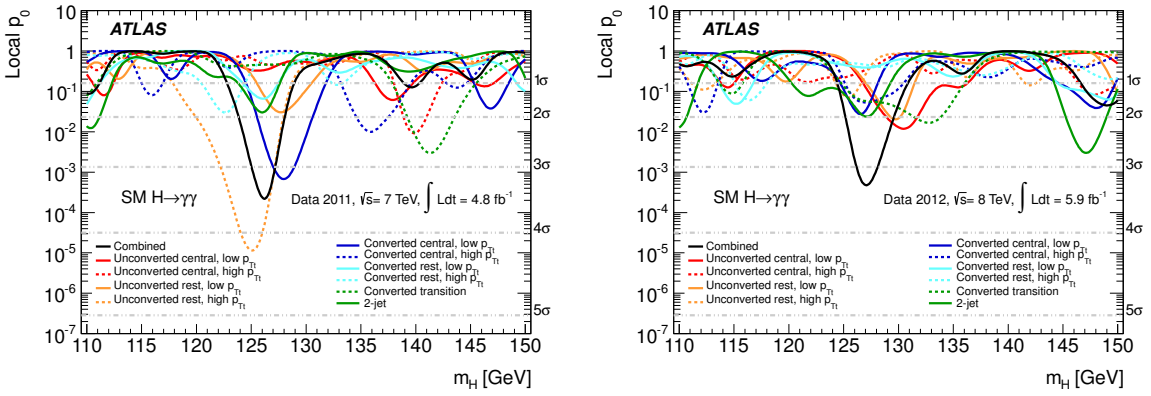

(a) $\sqrt{s} = 7$ TeV data. (b) $\sqrt{s} = 8$ TeV data.

Figure 9.13: The compatibility of the data with the background-only hypothesis, as a function of the hypothetical Higgs mass. Each curve in the plot represents the p_0 probability from a single analysis category.

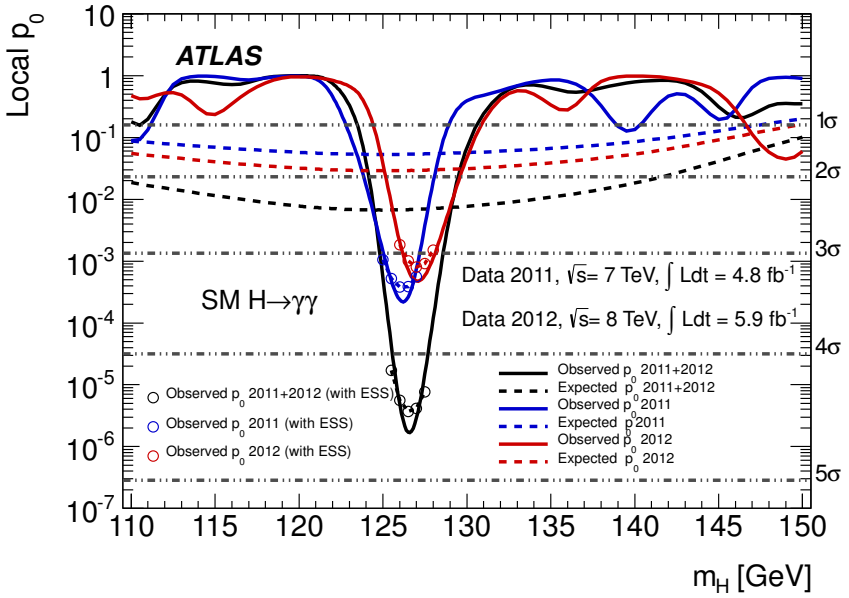

Figure 9.14: The compatibility of the data with the background-only hypothesis, as a function of the hypothetical signal mass, after combining the individual analysis categories and the $\sqrt{s} = 7$ TeV and $\sqrt{s} = 8$ TeV datasets. The p_0 values are shown with and without energy scale systematics.

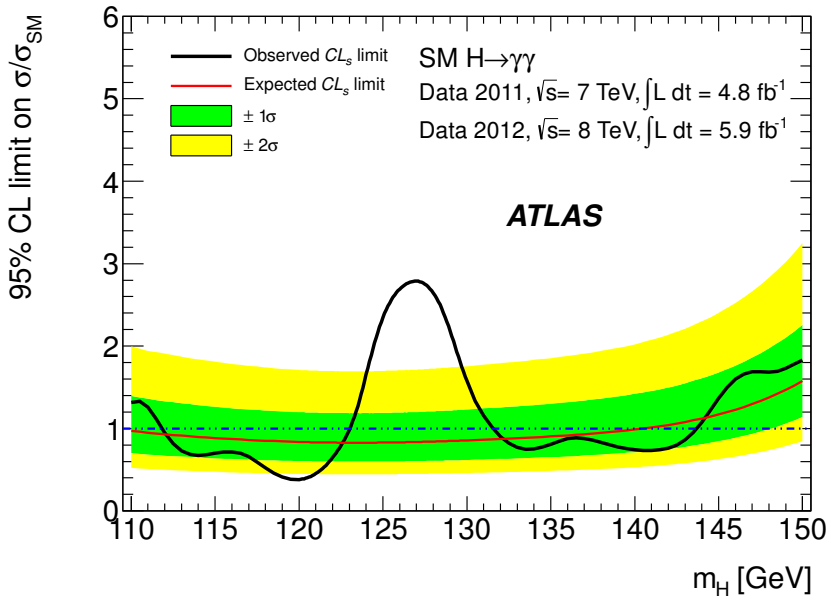

Figure 9.15: The expected and observed 95% *CL* exclusion limits on the Standard Model Higgs boson with the $H \to \gamma\gamma$ channel, after combining the individual analysis categories and the $\sqrt{s} = 7$ TeV and $\sqrt{s} = 8$ TeV datasets.

9.1.3 Exclusion limits on the Standard Model Higgs boson

The observed data were used to compute 95% *CL* exclusion limits on the Standard Model Higgs boson in the mass range 110 GeV $\leq m_H \leq$ 150 GeV. Figure 9.15 shows the expected and observed *CL* limit on the signal strength. The search was expected to exclude Standard Model Higgs bosons with masses between 110 GeV and 140 GeV. Given the excess of events observed near $m_H = 126.5$ GeV, the exclusion was limited to the mass ranges 112 GeV $\leq m_H \leq$ 123 GeV and 132 GeV $\leq m_H \leq$ 143 GeV.

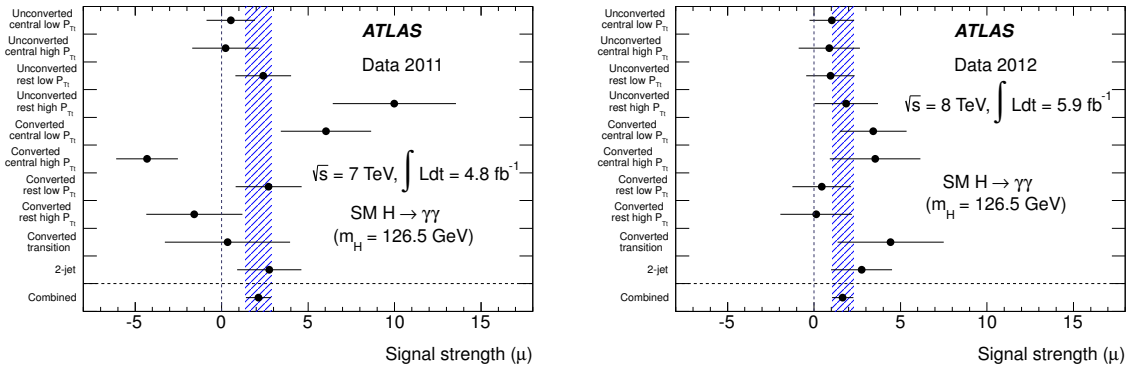

(a) $\sqrt{s} = 7$ TeV data.

(b) $\sqrt{s} = 8$ TeV data.

Figure 9.16: The signal strength in each of the analysis categories, for $\sqrt{s} = 7$ TeV and $\sqrt{s} = 8$ TeV data, separately. The measurements are performed using the maximum-likelihood mass of $\hat{m}_H = 126.5$ GeV.

9.1.4 Signal strength measurement

The compatibility of the cross-section of the excess with the expectation for the Standard Model Higgs boson was measured. The signal strength, $\mu = \sigma_{\text{obs.}}/\sigma_{\text{SM}}$ was profiled for each analysis category independently in $\sqrt{s} = 7$ TeV and $\sqrt{s} = 8$ TeV data (Figure 9.16) and with the combined dataset (Figure 9.17). For the maximum-likelihood mass of $m_H = 126.5$ GeV, the corresponding inclusive signal strength was $\hat{\mu} = 1.9 \pm 0.5$.

A full 2D likelihood contour scan in the plane of m_H and μ was performed. Figure 9.18a shows the maximum-likelihood fit value along with the 68% and 95% *CL* contours. The separate signal strengths for Higgs boson production via ggH or $t\bar{t}H$ and VBF or VH were also measured using a 2D likelihood contour scan in the plane of $\mu_{ggH+t\bar{t}H}$ and μ_{VBF+VH}. The maximum-likelihood fit result, along with the 68% and 95% *CL* contours, are shown in Figure 9.18b.

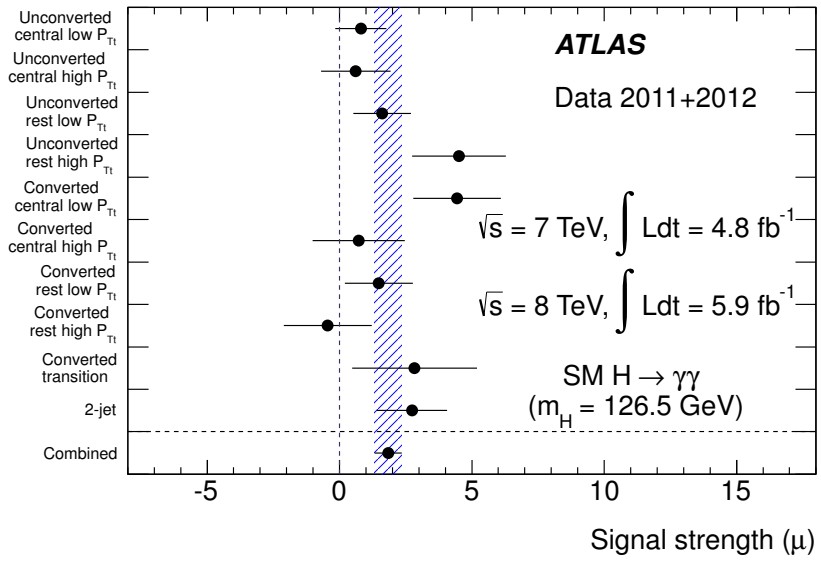

Figure 9.17: The signal strength in each of the analysis categories, after combining $\sqrt{s} = 7$ TeV and $\sqrt{s} = 8$ TeV data. The measurements are performed using the maximum-likelihood mass of $\hat{m}_H = 126.5$ GeV.

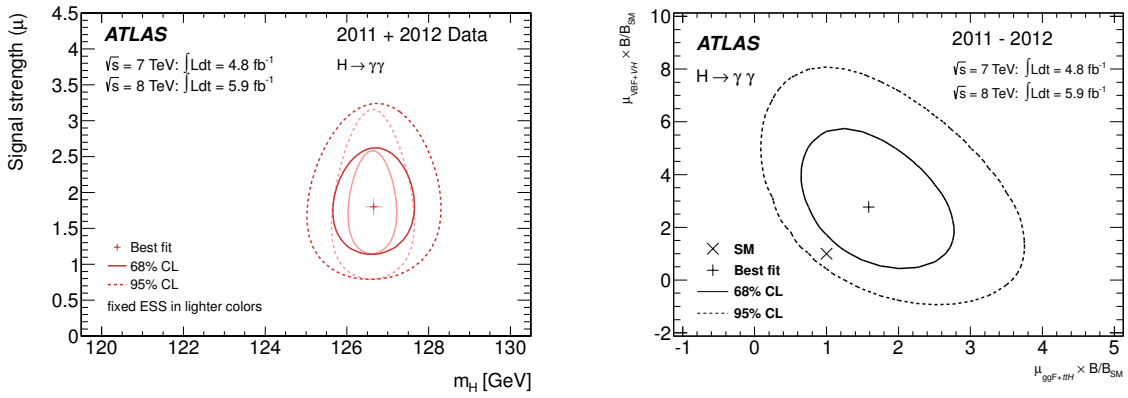

(a) (b)

Figure 9.18: A two-dimensional likelihood scan of the mass and signal strength of the observed particle is shown in Figure 9.18a. The lighter colored contours show the results when the energy scale systematic uncertainties are fixed. A two-dimensional likelihood scan of the signal strength of the observed particle in the decays to $ggH+t\bar{t}H$ and $VBF+VH$ is shown in Figure 9.18b. Both figures show the maximum-likelihood values from the scan, along with the 68% and 95% CL contours.

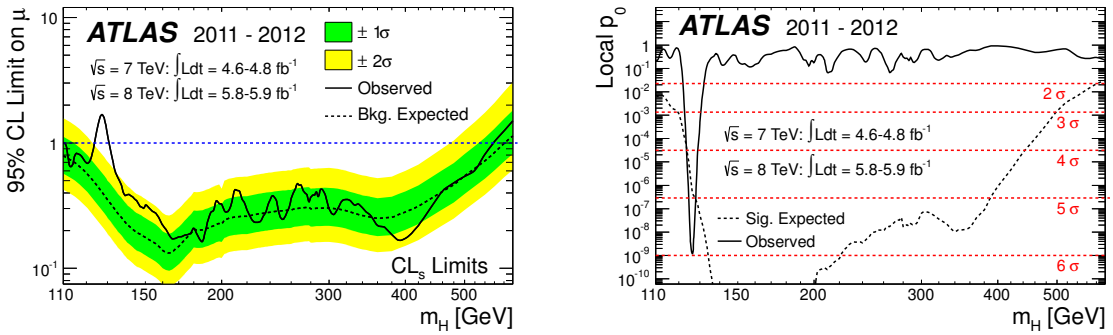

(a) CL limits on μ.

(b) Local p_0.

Figure 9.19: Statistical results from the combined search for the Standard Model Higgs boson using the $H \to \gamma\gamma$, $H \to ZZ^* \to 4l$, and $H \to WW^* \to l\nu l\nu$ decay channels. Figure 9.19a shows the 95% CL exclusion limit on the Standard Model Higgs boson, while Figure 9.19b shows the p_0 compatibility of the data with the background-only expectation.

9.1.5 Combination with other Higgs decay channels

Observations from the $H \to \gamma\gamma$ decay channel were combined with the $H \to ZZ^* \to 4l$ and $H \to WW^* \to e\nu\mu\nu$ decay channels to increase the statistical power of the search for the Standard Model Higgs boson [19]. Figure 9.19 summarizes the results of the statistical combination of channels. Figure 9.19a provides the expected and observed 95% CL exclusion limits on the Standard Model Higgs boson, in units of signal strength and as a function of hypothetical signal mass. The search was expected to exclude the mass range 110 GeV $\leq m_H \leq$ 582 GeV, but the observed exclusion was limited to the regions 111 GeV $\leq m_H \leq$ 122 GeV and 131 GeV $\leq m_H \leq$ 559 GeV.

Figure 9.19b shows the p_0 value for the combined search for the Standard Model Higgs boson. The compatibility of the background-only hypothesis with the observed

data is $p_0 = 1.7\times10^{-9}$ for a hypothetical Higgs boson mass of 126.5 GeV, corresponding to 5.9 standard deviations. Once the look-elsewhere effect is taken into account for the mass range 110 GeV $\leq m_H \leq$ 600 GeV, the global significance of the excess is reduced to 5.1 standard deviations. This level of incompatibility of the observations with the background-only hypothesis in favor of the Higgs boson signal-plus-background hypothesis constitutes a discovery of a new particle.

Figure 9.20a shows the measured signal strength for a Higgs boson as a function of m_H in the combined analysis. The results are compatible with zero (background-only expectation), except for points near $m_H = 126.5$ GeV, where the signal strength is more compatible with the Standard Model Higgs boson expectation. The high-resolution $H \to \gamma\gamma$ and $H \to ZZ^* \to 4l$ were used to calculate a maximum-likelihood Higgs boson mass of $\hat{m}_H = 126.0$ GeV ± 0.4 GeV (stat.) ± 0.4 GeV (sys.). Figure 9.20b shows the signal strengths for the individual Higgs boson decay channels along with the combined measurement of $\hat{\mu} = 1.4 \pm 0.3$ for the maximum-likelihood mass value.

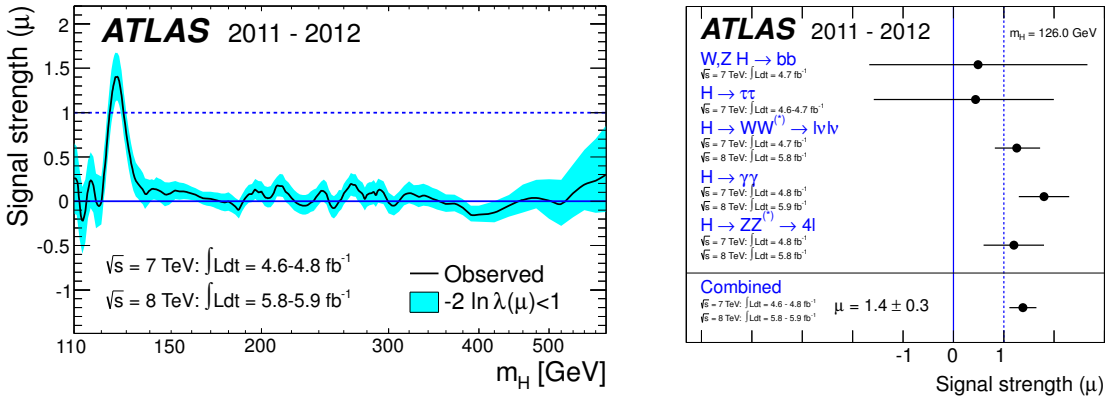

(a) (b)

Figure 9.20: The profiled signal strength from the combined search for the Standard Model Higgs boson using the $H \to \gamma\gamma$, $H \to ZZ^* \to 4l$, and $H \to WW^* \to l\nu l\nu$ decay channels is shown in Figure 9.20a as a function of Higgs boson mass. Figure 9.20b shows the profiled signal strengths from the individual channels for the maximum-likelihood Higgs boson mass of $\hat{m}_H = 126.0$ GeV.

9.2 Search for high-mass scalar resonances

This section summarizes the results of the search for new scalar particles in the resonant high-mass diphoton final state using 15.4 fb^{-1} of data collected with a center-of-mass energy of $\sqrt{s} = 13$ TeV during 2015 and 2016. Section 9.2.1 summarizes the observed invariant mass distributions of selected diphoton events, Section 9.2.2 discusses the compatibility of the data with the background-only hypothesis, and Section 9.2.3 provides the exclusion limits placed on the fiducial cross-sections of signals.

9.2.1 Invariant mass spectra

Figures 9.21a and 9.21b show the distributions of invariant diphoton masses for selected events in the 2015 and 2016 datasets, respectively, while Figure 9.22 shows the sum of the two datasets. The red curves in these figures correspond to the background-only hypothesis after performing a maximum-likelihood fit. The sub-figures provide the background-subtracted data. From all of the selected events, the highest mass diphoton pair was seen in 2016 with $m_{\gamma\gamma} = 2.2$ TeV. Considering this, the statistical analyses were limited to the mass range 200 GeV $< m_{\gamma\gamma} <$ 2400 GeV. Qualitatively, good agreement was observed between the data and the background-only hypothesis.

9.2.2 Compatibility with the background-only hypothesis

The p_0 test described in Section 8.2.5 was used to evaluate the compatibility of the observed data with the background-only hypothesis. The p_0 probability was scanned for a range of hypothetical scalar masses (200 GeV $< m_X <$ 2.4 TeV) and widths ($\Gamma_X \geq 4$ MeV and $\Gamma_X/m_X < 10\%$). Figure 9.23 shows the results of p_0 scans

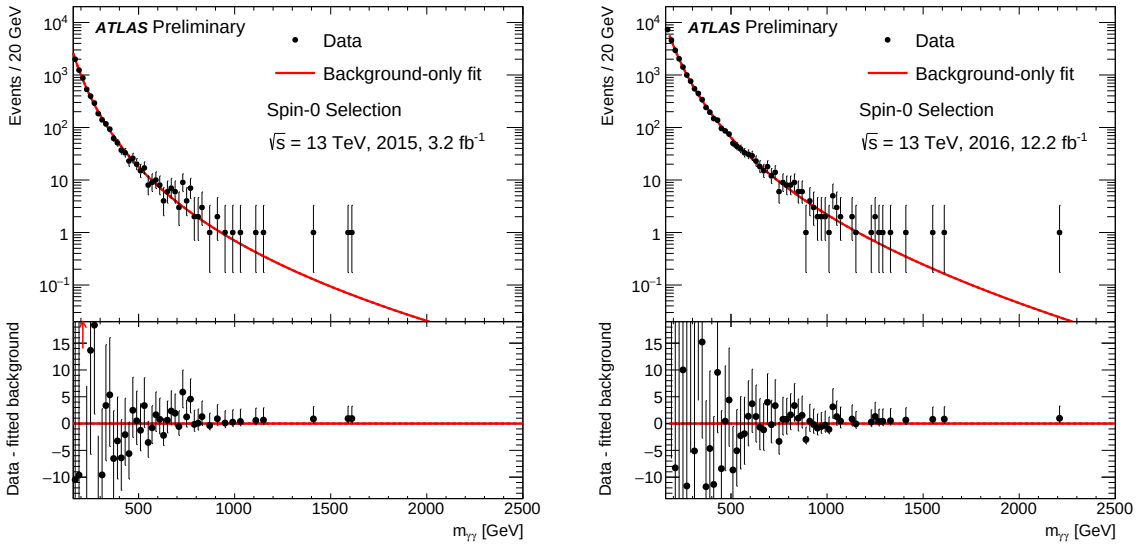

(a) 2015 data

(b) 2016 data

Figure 9.21: The diphoton invariant mass spectrum for selected events in the 2015 data (Figure 9.21a) and the 2016 data (Figure 9.21b). The black data points are compared with the red background-only fit result. The sub-plot shows the observed data after subtraction of the background-only fit result.

as a function of mass for several values of the relative width. Figure 9.24 shows the z_0 significances corresponding to the observed p_0, in units of standard deviations, for the full two-dimensional space of hypothetical scalar masses and widths.

No significant deviations from the background-only hypothesis were observed. The largest deviation from the background expectation was found for a hypothetical signal mass of 1.6 TeV and a narrow width ($\Gamma_X = 4$ MeV), and corresponded to a local significance of 2.4 standard deviations. The pseudo-experiment procedure detailed in Appendix A was used to calculate a global significance of $-0.8\sigma \pm 0.05\sigma$. In other words, the median background-only experiment would see a larger fluctuation (2.6 standard deviations) than the one actually observed in data.

In the standalone publication of 2015 data [31], the high-mass diphoton search

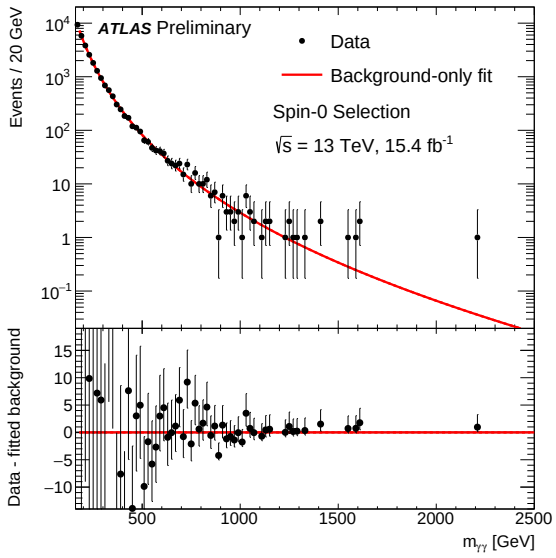

Figure 9.22: The distribution of diphoton invariant masses for selected events in the combined datasets from 2015 and 2016. The red background-only fit result is compared with the black data entries. The sub-plot shows the observed data after subtraction of the background-only fit result.

found a local deviation from the background-only hypothesis of 3.9 standard deviations for a hypothetical signal with $m_X = 750$ GeV and $\Gamma_X/m_X = 6\%$. The corresponding global significance of that observation was 2.1 standard deviations. After implementing improvements to the photon reconstruction algorithms, the significance of the excess in 2015 data with the current analysis strategy was reduced to 3.4 standard deviations with maximum-likelihood fit values for the mass and relative width of $m_X = 730$ GeV and $\Gamma_X/m_X = 8\%$. The compatibility between the 2015 and 2016 data for this mass hypothesis was found to be 2.7 standard deviations.

9.2.3 Exclusion limits on new scalars

The observed high-mass diphoton data were used to calculate 95% *CL* exclusion limits on the cross-section times branching ratio to $\gamma\gamma$ for new scalars. In order to

minimize the model dependence of the results, the limits were based on the cross-section within the fiducial acceptance. Figure 9.25 shows one-dimensional scans of the expected and observed limits as a function of hypothetical resonance mass for multiple values of the signal width, including $\Gamma_X = 4$ MeV, $\Gamma_X/m_X = 2\%$, $\Gamma_X/m_X = 6\%$, and $\Gamma_X/m_X = 10\%$. Figure 9.26 provides the expected and observed limits in a two-dimensional plane of hypothetical signal masses and relative widths. The limits vary from 50 fb for $m_X = 200$ GeV and $\Gamma_X/m_X = 10\%$ to 0.2 fb for $m_X = 2.4$ TeV and $\Gamma_X = 4$ MeV.

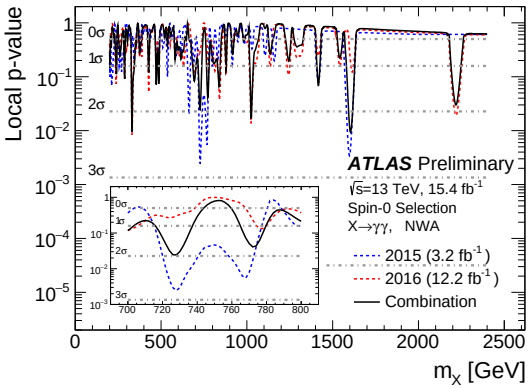

(a) $\Gamma_X = 4$ MeV

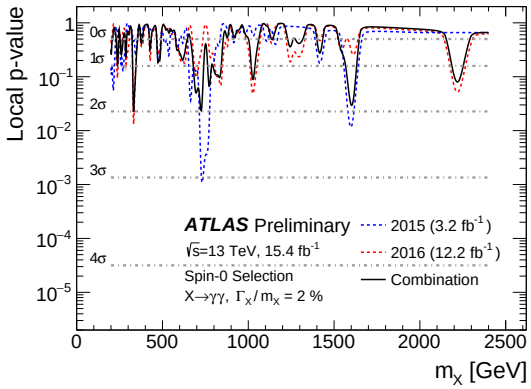

(b) $\Gamma_X/m_X = 2\%$

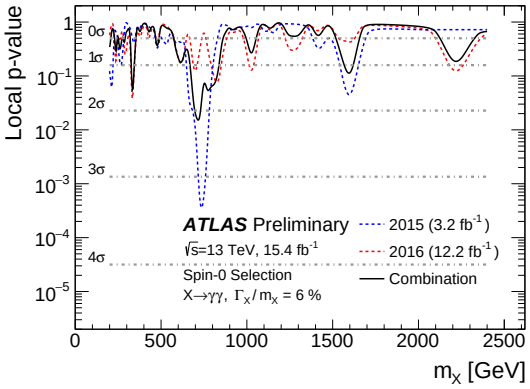

(c) $\Gamma_X/m_X = 6\%$

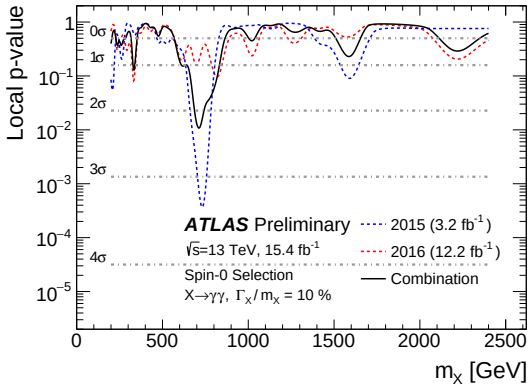

(d) $\Gamma_X/m_X = 10\%$

Figure 9.23: p_0 scans showing the compatibility of the observed data with the background-only hypothesis as a function of the mass of hypothetical scalar signals. Results are shown for four signal width hypotheses, including the narrow-width approximation, where $\Gamma_X = 4$ MeV (Figure 9.23a), $\Gamma_X/m_X = 2\%$ (Figure 9.23b), $\Gamma_X/m_X = 6\%$ (Figure 9.23c), and $\Gamma_X/m_X = 10\%$ (Figure 9.23d).

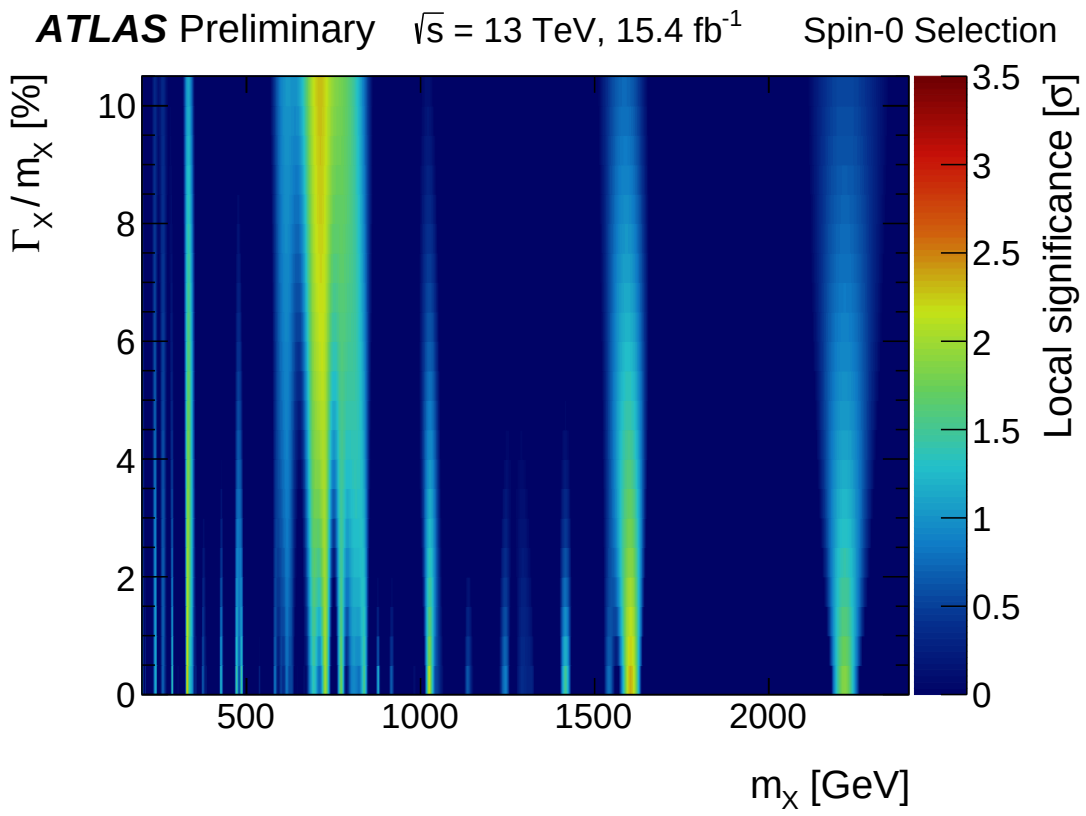

Figure 9.24: The z_0 compatibility of the observed data with the background-only hypothesis as a function of mass and width for hypothetical scalar signals, in units of standard deviations (σ).

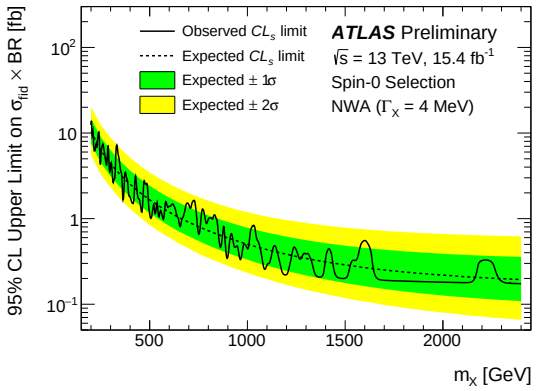

(a) $\Gamma_X = 4$ MeV

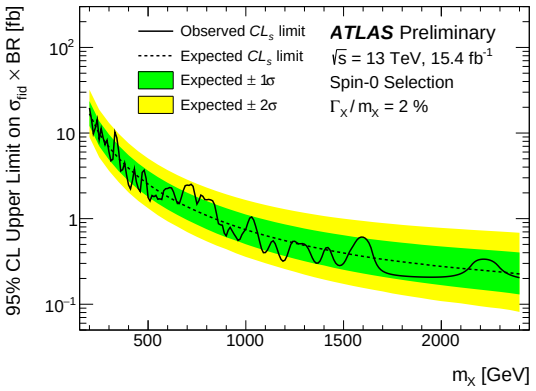

(b) $\Gamma_X/m_X = 2\%$

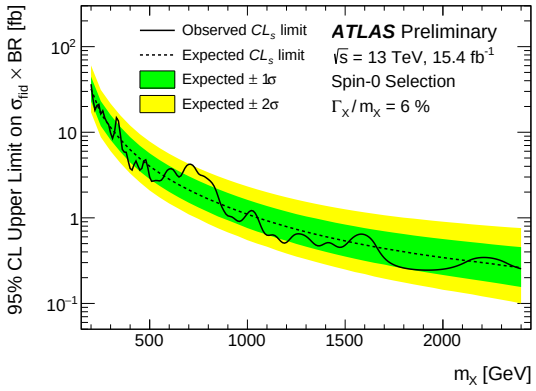

(c) $\Gamma_X/m_X = 6\%$

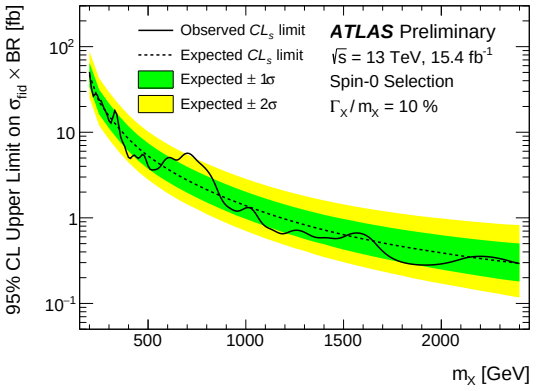

(d) $\Gamma_X/m_X = 10\%$

Figure 9.25: Expected and observed 95% *CL* exclusion limits on the fiducial cross-section times branching ratio to $\gamma\gamma$ at $\sqrt{s} = 13$ TeV as a function of mass for hypothetical scalar signals. Results are shown for four signal width hypotheses, including the narrow-width approximation, where $\Gamma_X = 4$ MeV (Figure 9.25a), $\Gamma_X/m_X = 2\%$ (Figure 9.25b), $\Gamma_X/m_X = 6\%$ (Figure 9.25c), and $\Gamma_X/m_X = 10\%$ (Figure 9.25d).

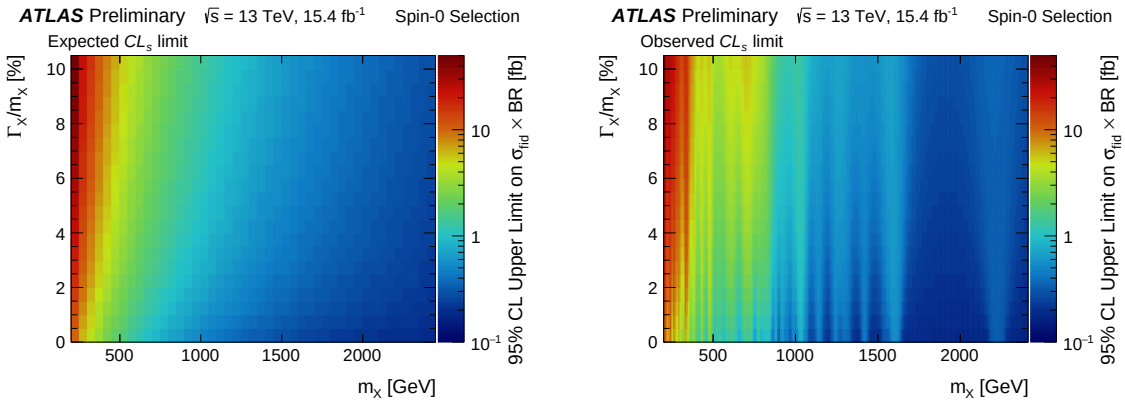

(a) Expected limits.

(b) Observed limits.

Figure 9.26: Expected and observed 95% *CL* exclusion limits on the fiducial cross-section times branching ratio to $\gamma\gamma$ at $\sqrt{s} = 13$ TeV as a function of mass and width for hypothetical scalar signals.

Chapter 10

Conclusions

10.1 Discovery of a Standard Model Higgs boson

A search for the Standard Model Higgs boson decaying to two photons was conducted with 4.8 fb^{-1} of $\sqrt{s} = 7$ TeV data and 5.9 fb^{-1} of $\sqrt{s} = 8$ TeV data collected with the ATLAS detector at the LHC. The search was expected to exclude Higgs boson mass hypotheses at 95% *CL* between 110 GeV and 139.5 GeV, but the observed exclusion was limited to the mass regions 112 GeV $\leq m_H \leq$ 122.5 GeV and 132 GeV $\leq m_H \leq$ 143 GeV. An excess of events above the background-only hypothesis expectation was observed at 126.5 GeV which corresponded to a significance of 4.5 standard deviations.

The $H \to \gamma\gamma$ search was combined with the $H \to ZZ^* \to 4l$ and $H \to WW^* \to e\nu\mu\nu$ decay channels in ATLAS in order to improve the sensitivity of the Standard Model Higgs boson search. With the exception of the mass range 122 GeV $\leq m_H \leq$ 131 GeV, the Higgs boson mass hypotheses between 111 GeV and 559 GeV were excluded at 95% *CL*. An excess of events in all three decay channels was observed

with a local significance of 5.9 standard deviations at a mass of 126.0 ± 0.4 (stat.) ± 0.4 (sys.) GeV. Once the look-elsewhere effect was taken into consideration for the search region, the global significance of the excess was 5.1 standard deviations. This constituted the discovery of a new particle. The signal strength was measured to be 1.4 ± 0.3 times the Standard Model signal strength.

10.2 Concluding the high-mass diphoton search

A search for high-mass scalar resonances in the $\gamma\gamma$ channel was conducted with 15.4 fb^{-1} of data collected at $\sqrt{s} = 13$ TeV during 2015 and 2016. Overall, the data were consistent with the background-only hypothesis. The largest deviation from the background expectation occurred for a scalar mass hypothesis of 1.6 TeV and had a local significance of 2.4 standard deviations. However, this fluctuation was not globally significant, after accounting for the look-elsewhere effect. 95% *CL* limits were calculated for scalar mass hypotheses between 200 GeV and 2.4 TeV and width hypotheses between $\Gamma_X = 4$ MeV and $\Gamma_X/m_X = 10\%$.

10.3 Prospects for experimental high-energy physics

Since the discovery of the Higgs boson, measurements of the spin [22], production rates, and decay rates [23] have been in excellent agreement with the Standard Model predictions. Searches for supersymmetry, dark matter, and other extensions to the Standard Model have also failed to uncover any new phenomena.

Having accomplished the last energy upgrade intended for the LHC, it is natural to wonder about the prospects for discovery moving forward. Datasets with significantly larger integrated luminosities will certainly benefit precision measurements, but

they do not improve search sensitivities nearly as much as increased center-of-mass energies. Four-fold increases in sample sizes are necessary to double discovery potential, while a doubling of $\sqrt{s}$ can increase production cross-sections by orders of magnitude for some BSM processes.

It therefore seems in the best interest for the field to pursue future accelerators with higher center-of-mass energies instead of higher luminosities. Dark matter, dark energy, inflation, and gravitation are just a few of the known physical phenomena that lack an experimentally verified field theory description. It is possible that none of these phenomena would impact TeV-scale experiments.

Another step towards the energy frontier is necessary, yet there is no strong motivation for doing so from observations. This makes a future accelerator difficult to sell, and raises the stakes for future results. If the superconducting supercollider is any guide, large scale accelerators without a clear physics motivation have difficulty sustaining funding and rallying support in the field. But one must continue the search, for there is always more knowledge to be gained and new questions to be asked. And the greatest discoveries are often unexpected. Experimental high-energy physics will continue. The only question is whether we will be the ones lucky enough to first glimpse the new horizon.

Appendix A

Global significance

This chapter extends the discussion from Section 8.5 on methods for quantifying the look-elsewhere effect and measuring the global significance for the high-mass scalar search. Section A.1 summarizes the pseudo-experiment procedure that was developed and optimized for the analysis, while Section A.2 introduces an approximation formula that can be extrapolated to 5 standard deviation global significances. These studies were initially motivated by excesses of events above the Standard Model expectation in 2015 data that represented local deviations from the background-only hypothesis of 3.9 standard deviations and 3.8 standard deviations in the scalar and graviton searches, respectively [31].

A.1 Pseudo-experiment method

The value of $Z_{0,\text{global}}$ as a function of $Z_{0,\text{local}}$ was computed using fits to background-only pseudo-experiment ensembles. The procedure for creating randomized pseudo-experiments from a likelihood model is described in Section 8.3. An *unconditional* pseudo-experiment ensemble was generated in which the auxiliary measurements cor-

responding to each systematic uncertainty were randomized with a Gaussian constraint around the nuisance parameter values obtained through a background-only hypothesis-conditional maximum-likelihood fit to the observed data. The diphoton invariant mass observable was also randomized according to the background PDF defined in the likelihood model.

Following the generation of the pseudo-data, the largest deviation from the background-only hypothesis, corresponding to the maximum local Z_0, had to be identified. Repeating the simple scan over width and mass hypotheses in the analysis would have required tens of thousands of maximum-likelihood fits to each pseudo-experiment in an ensemble consisting of thousands of pseudo-experiments. Considering the fact that a single maximum-likelihood fit required several minutes of CPU time, such an analysis was considered impractical.

An alternative was developed in which multiple unconditional maximum-likelihood fits with floating parameters of interest (m_X, Γ_X, σ_X) were performed on each dataset. Prior to every fit, the initial values of the parameters of interest were randomized within the signal parameter space of the search. The fit giving the minimum negative-log-likelihood value was assumed to correspond to the maximum $Z_{0,\text{local}}$ from the pseudo-experiment.

Repetition of the maximum-likelihood fits was necessary due to the number of local minima in the likelihood space. Studies of the quality of the result as a function of the number of fit retries were performed. Figure A.1 shows the mean and Gaussian width of the distribution of local-Z_0 values as a function of the number of attempted maximum-likelihood fits. The distribution stabilized after approximately 50 retries, which indicated that a reasonable approximation of the maximum-likelihood

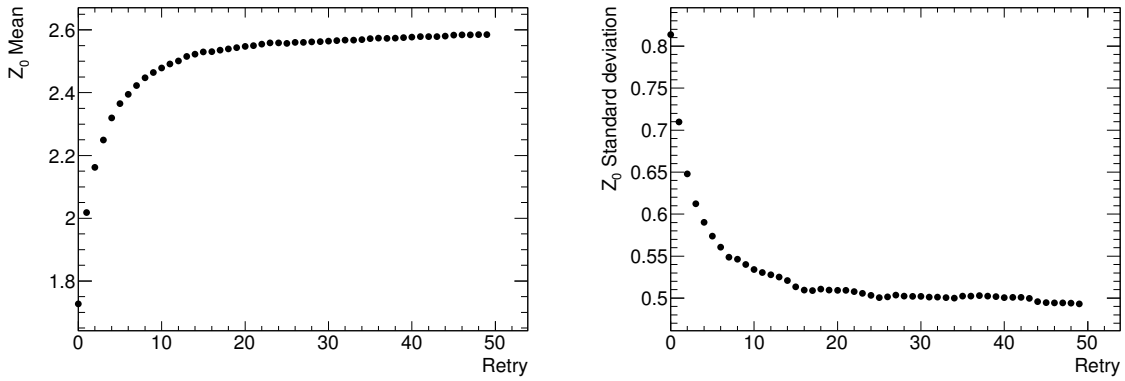

(a) (b)

Figure A.1: The mean value (Figure A.1a) and Gaussian width (Figure A.1b) of the distribution of local-Z_0 values as a function of the number of attempted maximum-likelihood fits for the high-mass scalar analysis.

fit (and the maximum local significance) had been achieved for most pseudo-datasets. Furthermore, Figure A.2 indicated that the average improvement in the $-\ln\mathcal{L}$ dropped to a level that was unlikely to significantly impact the global significance calculation. Furthermore, there was reason to believe that multiple fit retries primarily assisted in the identification of the maximum-likelihood fit result for datasets with relatively small values of the maximum $Z_{0,\mathrm{local}}$.

The distribution of $Z_{0,\mathrm{local}}$ from statistical tests on the background-only pseudo-experiments was used to derive the $Z_{0,\mathrm{global}}$. An example distribution from 2500 pseudo-experiments is shown in the top plot of Figure A.3 for the high-mass graviton search described in Ref. [31] . In this example, the median experiment searching for a graviton would observe a local significance at least as large as 2.6 standard deviations.

To calculate $Z^{\mathrm{obs.}}_{0,\mathrm{global}}$ for a given $Z^{\mathrm{obs.}}_{0,\mathrm{local}}$, the distribution of $Z_{0,\mathrm{local}}$, represented by $f(Z_{0,\mathrm{local}})$, was integrated from the observed value to infinity:

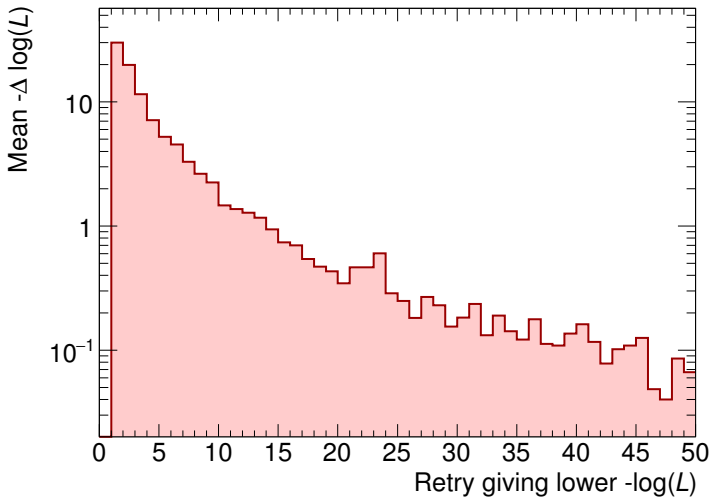

Figure A.2: Average reduction in $-\ln\mathcal{L}$ for fits that find a new minimum, as a function of the number of fit attempts.

$$Z^{\text{obs.}}_{0,\text{global}} = \int_{Z^{\text{obs.}}_{0,\text{local}}}^{\infty} f(Z_{0,\text{local}})dZ_{0,\text{local}}. \tag{A.1}$$

Binomial errors, based on the number of pseudo-experiments and the $p^{\text{obs.}}_{0,\text{local}}$, were used to derive an uncertainty on the measurement. The conversion of local significance to global significance is shown in the bottom plot of Figure A.3. For the graviton example, a local significance of 3.8 standard deviations was observed, and the corresponding global significance was measured to be 2.15 ± 0.04 standard deviations. The results were compared to the trial factor method [162] and random field method [163], and were found to agree within 10%.

A.2 Analytic approximation

Despite the improvements that were made to the pseudo-experiment calculation of the global significance described in Section A.1, the procedure was not feasible for

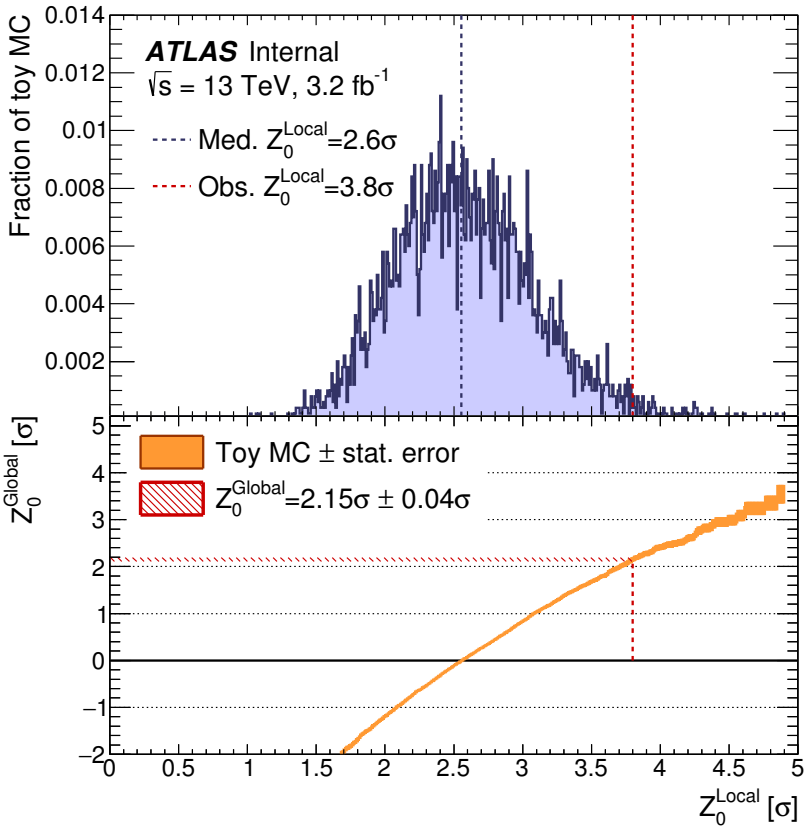

Figure A.3: The distribution of $Z_{0,\text{local}}$ in fits to pseudo-experiments in the graviton analysis. Bottom: measurement of $Z_{0,\text{global}}$ as a function of the local significance. Binomial errors due to the pseudo-experiment sample size are illustrated in yellow.

estimating large global significances. Given typical CPU consumption of 1 minute per fit and 1 hour per pseudo-experiment, a toy ensemble capable of delivering a 5 standard deviation global significance estimate would require millions of CPU hours. To overcome this obstacle, an analytic approximation algorithm was developed for the purpose of extrapolating the pseudo-experiment measurement of the global significance obtained using a small ensemble to very large global significances.

A.2.1 Derivation of the approximation

The derivation assumed that a physics search in a large signal space could be approximated by N uncorrelated statistical trials. This was a slight simplification, since most searches look for new phenomena in continuous signal spaces such as a mass variable or width variable. With this assumption, it was straightforward to derive a global p-value for a given local p-value. The steps are explained below.

- $(1 - p_{0,\text{local}})$: the probability of not observing a background fluctuation with a smaller value of $p_{0,\text{local}}$.
- $(1 - p_{0,\text{local}})^N$: the probability of not observing a background fluctuation with a smaller value of $p_{0,\text{local}}$ in N separate trials.
- $[1 - (1 - p_{0,\text{local}})^N]$: the probability of observing at least one background fluctuation with a smaller value of $p_{0,\text{local}}$ in any one of the N trials.

Thus, a search across N independent trials with a local observation of $p_{0,\text{local}}$ would have a $p_{0,\text{global}}$ given by Equation A.2. The corresponding sampling distribution of $p_{0,\text{local}}$ in multiple experiments is described by Equation A.3. As expected, $p_{0,\text{global}} = p_{0,\text{local}}$ in the trivial case of $N = 1$.

$$p_{0,\text{global}} = [1 - (1 - p_{0,\text{local}})^N] \tag{A.2}$$

$$\frac{dp_{0,\text{global}}}{dp_{0,\text{local}}} = N(1 - p_{0,\text{local}})^{N-1} \tag{A.3}$$

The expressions for the distributions of $Z_{0,\text{local}}$ and the value of $Z_{0,\text{global}}$ were then calculated as in Equations A.6 and A.7.

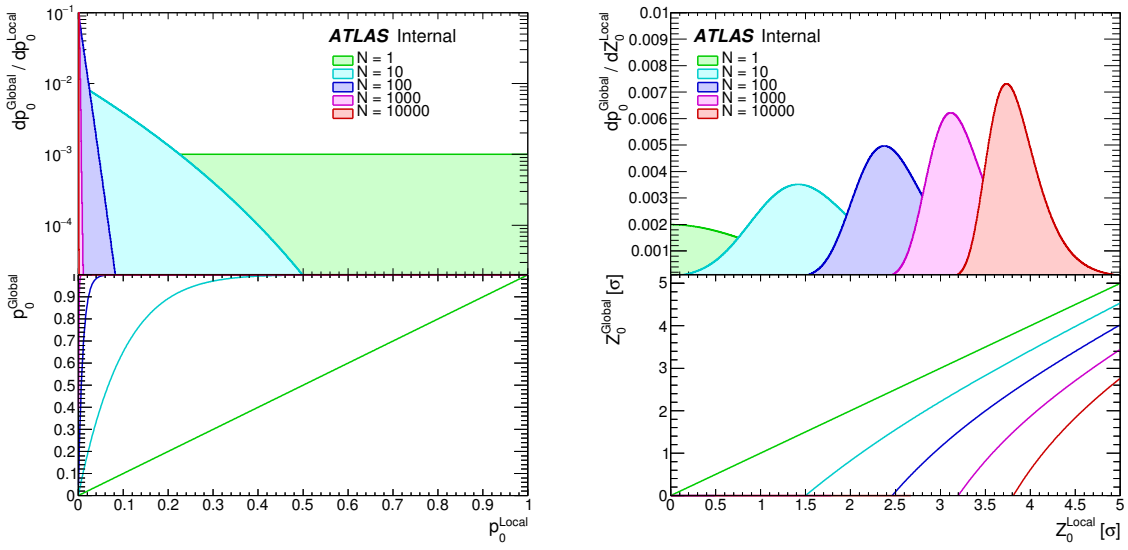

(a) p_0 (b) Z_0

Figure A.4: The normalized expected distributions of the local-p_0 and local-Z_0 for multiple values of N are shown in Figures A.4a and A.4b, respectively. The sub-figures show the conversion from local-p_0 or local-Z_0 to the corresponding global statistic.

$$Z_{0,\text{global}} = \Phi^{-1}\big(\Phi(Z_{0,\text{local}})^N\big), \tag{A.4}$$

$$\frac{dp_{0,\text{global}}}{dZ_{0,\text{local}}} = N\big(\Phi(Z_{0,\text{local}})\big)^{N-1}\Phi'(Z_{0,\text{local}}). \tag{A.5}$$

In these equations, Φ represents the cumulative distribution function of the Gaussian function, Φ^{-1} represents the quantile of the Gaussian function, and Φ' represents the Gaussian function. As expected, $Z_{0,\text{global}} = Z_{0,\text{local}}$ and $(dp_{0,\text{global}}/dZ_{0,\text{local}})$ simplifies to a Gaussian in the trivial case of $N = 1$.

An additional parameter was added to the analytic expression in order to account for non-asymptotic behavior of the q_0 sampling distribution discussed in Section 8.4. This was done by substituting $(1 + \alpha)Z_{0,\text{local}}$ for $Z_{0,\text{local}}$ in Equation A.6:

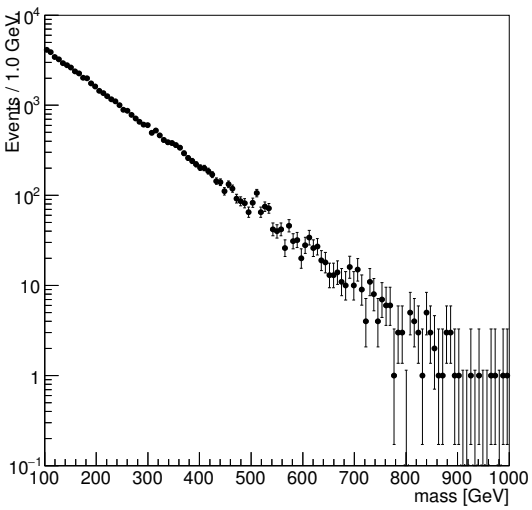

Figure A.5: The invariant mass distribution for a single pseudo-experiment generated with the simplified likelihood model described in Section A.2.2.

$$Z_{0,\text{global}} = \Phi^{-1}\big(\Phi((1+\alpha)Z_{0,\text{local}})^N\big), \tag{A.6}$$

$$\frac{dp_{0,\text{global}}}{dZ_{0,\text{local}}} = N\big(\Phi((1+\alpha)Z_{0,\text{local}})\big)^{N-1}\Phi'((1+\alpha)Z_{0,\text{local}})(1+\alpha). \tag{A.7}$$

The analytic expression thus uses two parameters, N and α, to convert a local significance measurement to a global measurement. In order to be of practical use, values of the parameters had to be set. Various methods for estimating the values of N and α were investigated, but fitting Equation A.7 to the distribution of $Z_{0,\text{local}}$ from a limited sample of pseudo-experiments was found to be the most reliable method.

A.2.2 Validation of the approximation

A simple likelihood model was used to generate 10^6 pseudo-experiments to validate Equations A.6 and A.7. The likelihood model described a search for a resonance

across a 100 GeV to 1 TeV mass (m_X) range, with a background described by a simple exponential function and a signal described by a Gaussian that scaled with resolution according to $\sigma_X = m_X/50$. No systematic uncertainties were implemented. As a result, the model had four free parameters: the background normalization and slope, the signal normalization and mean value. The model was deliberately made as simple as possible in order to reduce the time required by each maximum-likelihood fit to a few seconds. Figure A.5 shows the mass distribution for one of the background-only pseudo-experiments.

A comparison of Equations A.6 and A.7 to the results from simplified pseudo-experiments is shown in Figure A.6. The approximation agreed with the pseudo-experiment result within 5%. Fitting A.6 to sub-samples of the simplified pseudo-experiment ensemble also provided agreement in the $Z_{0,\text{global}}$ result within 10% for a 5 standard deviation global significance when the sub-sample consisted of 1000 or more pseudo-datasets.

A.2.3 Implications of the approximation

A few observations about the global significance computation can be made using the analytic approximation formula in Equation A.6. First, the global significance is only dependent on the range of the signal parameters in the search, the resolution of each parameter, and the correlations between the signal parameters – anything that can alter the trial factor N. This means that systematic uncertainties, other than those affecting the signal resolution, do not have any impact on the global significance. Even the choice of background model does not affect the relation between local and global significance, though a bad model could produce an invalid local significance.

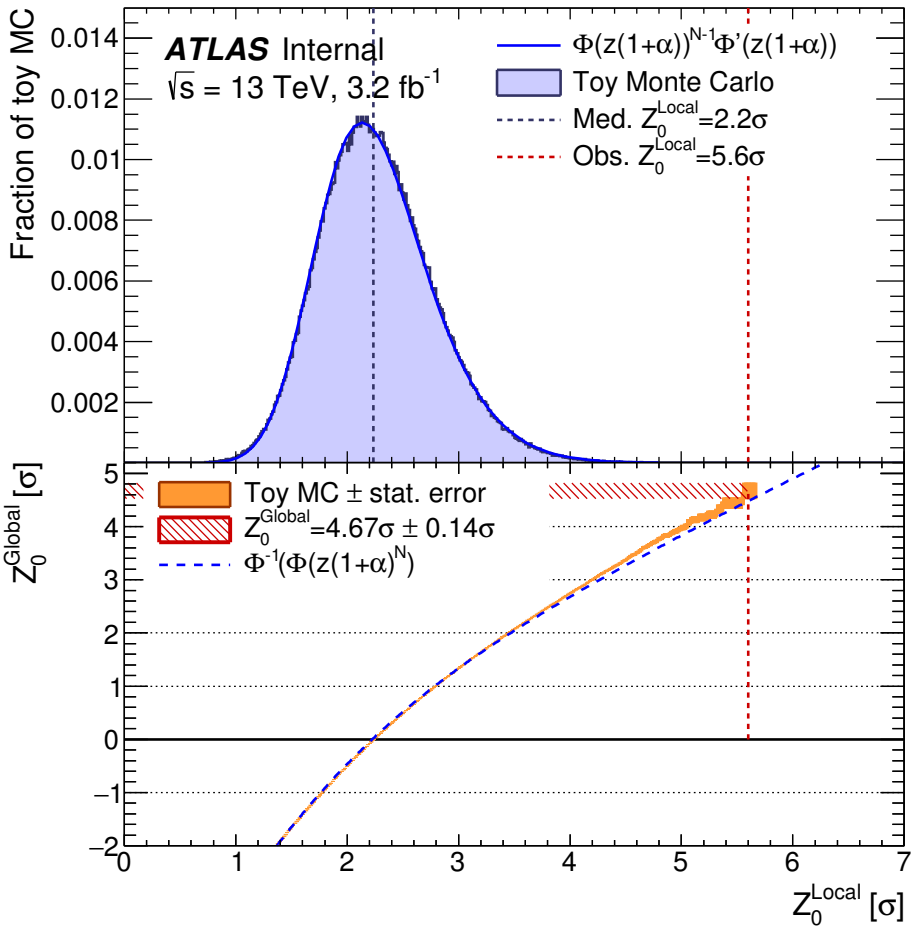

Figure A.6: Top: a comparison of the distribution of $Z_{0,\text{local}}$ in simplified pseudo-experiments to a fit of the analytic description from Equation A.7. Bottom: a comparison of the integral of $Z_{0,\text{local}}$ to the analytic description from Equation A.7.

The global significance also has a logarithmic dependence on the size of the search region, as illustrated in Figure A.4b. Order of magnitude increases in the size of the search range, approximated by N, lead to linear decreases in the global significance. The lesson is that the search region used to compute the global significance does not need to be determined with a high degree of precision.

A.3 Discussion of high-mass scalar search observations

The global significance corresponding to the maximum local significance observed in the high-mass scalar search was calculated using 1,000 pseudo-experiments. For the maximum observed local significance of 2.3 standard deviations, the global significance was found to be -0.8 ± 0.05 standard deviations. The uncertainty on the global significance was due to the sample size of the pseudo-experiment ensemble.

The median experiment conducted under the background-only hypothesis would identify at least one signal point in the search space with a deviation from the background hypothesis greater than 2.5 standard deviations. The maximum local significance of 2.5 standard deviations in the high-mass scalar search thus represented a global downward fluctuation of the data. In other words, 79% of searches would identify a larger deviation than the one observed. The data were more consistent with the background-only hypothesis than expected.

Bibliography

[1] ATLAS Collaboration, G. Aad et al., *The ATLAS experiment at the CERN Large Hadron Collider*, JINST **3** (2008) S08003.

[2] M. Capeans, G. Darbo, K. Einsweiller, M. Elsing, T. Flick, M. Garcia-Sciveres, C. Gemme, H. Pernegger, O. Rohne, and R. Vuillermet, *ATLAS Insertable B-Layer technical design report*, Tech. Rep. CERN-LHCC-2010-013. ATLAS-TDR-19, 2010. `https://cds.cern.ch/record/1291633`.

[3] S. L. Glashow, *Partial symmetries of weak interactions*, Nucl. Phys. **22** (1961) 579–588.

[4] S. Weinberg, *A model of leptons*, Phys. Rev. Lett. **19** (1967) 1264–1266. `http://link.aps.org/doi/10.1103/PhysRevLett.19.1264`.

[5] A. Salam, *Weak and electromagnetic interactions*, Conf. Proc. **C680519** (1968) 367–377.

[6] G. 't Hooft and M. Veltman, *Regularization and renormalization of gauge fields*, Nuclear Physics B **44** (1972) no. 1, 189 – 213. `http://www.sciencedirect.com/science/article/pii/0550321372902799`.

[7] F. Englert and R. Brout, *Broken symmetry and the mass of gauge vector mesons*, Phys. Rev. Lett. **13** (1964) 321–323. http://link.aps.org/doi/10.1103/PhysRevLett.13.321.

[8] P. W. Higgs, *Broken symmetries, massless particles and gauge fields*, Physics Letters **12** (1964) no. 2, 132 – 133. http://www.sciencedirect.com/science/article/pii/0031916364911369.

[9] P. W. Higgs, *Broken symmetries and the masses of gauge bosons*, Phys. Rev. Lett. **13** (1964) 508–509. http://link.aps.org/doi/10.1103/PhysRevLett.13.508.

[10] P. W. Higgs, *Spontaneous symmetry breakdown without massless bosons*, Phys. Rev. **145** (1966) 1156–1163. http://link.aps.org/doi/10.1103/PhysRev.145.1156.

[11] G. S. Guralnik, C. R. Hagen, and T. W. B. Kibble, *Global conservation laws and massless particles*, Phys. Rev. Lett. **13** (1964) 585–587. http://link.aps.org/doi/10.1103/PhysRevLett.13.585.

[12] T. W. B. Kibble, *Symmetry breaking in non-abelian gauge theories*, Phys. Rev. **155** (1967) 1554–1561. http://link.aps.org/doi/10.1103/PhysRev.155.1554.

[13] OPAL, DELPHI, LEP Working Group for Higgs boson searches, ALEPH, L3 Collaboration, R. Barate et al., *Search for the standard model Higgs boson at LEP*, Phys. Lett. **B565** (2003) 61–75, arXiv:hep-ex/0306033 [hep-ex].

[14] CDF and D0 Collaboration, T. Aaltonen et al., *Combination of Tevatron searches for the Standard Model Higgs boson in the W^+W^- decay mode*, Phys. Rev. Lett. **104** (2010) 061802. http://link.aps.org/doi/10.1103/PhysRevLett.104.061802.

[15] Tevatron Electroweak Working Group, CDF, DELPHI, SLD Electroweak and Heavy Flavour Groups, ALEPH, LEP Electroweak Working Group, SLD, OPAL, D0, L3 Collaboration, L. E. W. Group, *Precision electroweak measurements and constraints on the Standard Model*, arXiv:1012.2367 [hep-ex].

[16] L. Evans and P. Bryant, *LHC machine*, JINST **3** (2008) S08001.

[17] CMS Collaboration, S. Chatrchyan et al., *The CMS experiment at the CERN LHC*, JINST **3** (2008) S08004.

[18] ATLAS Collaboration, G. Aad et al., *Observation of an excess of events in the search for the Standard Model Higgs boson in the gamma-gamma channel with the ATLAS detector*, Tech. Rep. ATLAS-CONF-2012-091, CERN, Geneva, 2012. https://cds.cern.ch/record/1460410.

[19] ATLAS Collaboration, G. Aad et al., *Observation of a new particle in the search for the Standard Model Higgs boson with the ATLAS detector at the LHC*, Phys. Lett. **B716** (2012) 1–29, arXiv:1207.7214 [hep-ex].

[20] CMS Collaboration, S. Chatrchyan et al., *Observation of a new boson at a mass of 125 GeV with the CMS experiment at the LHC*, Phys. Lett. **B716** (2012) 30–61, arXiv:1207.7235 [hep-ex].

[21] ATLAS, CMS Collaboration, G. Aad et al., *Combined measurement of the Higgs Boson mass in pp collisions at $\sqrt{s} = 7$ and 8 TeV with the ATLAS and CMS experiments*, Phys. Rev. Lett. **114** (2015) 191803, arXiv:1503.07589 [hep-ex].

[22] ATLAS Collaboration, G. Aad et al., *Evidence for the spin-0 nature of the Higgs boson using ATLAS data*, Phys. Lett. **B726** (2013) 120–144, arXiv:1307.1432 [hep-ex].

[23] ATLAS, CMS Collaboration, G. Aad et al., *Measurements of the Higgs boson production and decay rates and constraints on its couplings from a combined ATLAS and CMS analysis of the LHC pp collision data at $\sqrt{s} = 7$ and 8 TeV*, JHEP **08** (2016) 045, arXiv:1606.02266 [hep-ex].

[24] A. Hill and J. J. van der Bij, *Strongly interacting singlet-doublet Higgs model*, Phys. Rev. D **36** (1987) 3463–3473. http://link.aps.org/doi/10.1103/PhysRevD.36.3463.

[25] M. Veltman and F. Yndurin, *Radiative corrections to WW scattering*, Nuclear Physics B **325** (1989) no. 1, 1 – 17. http://www.sciencedirect.com/science/article/pii/0550321389903696.

[26] T. Binoth and J. van der Bij, *Influence of strongly coupled, hidden scalars on Higgs signals*, Zeitschrift für Physik C Particles and Fields **75** (1997) no. 1, 17–25. http://dx.doi.org/10.1007/s002880050442.

[27] R. Schabinger and J. D. Wells, *Minimal spontaneously broken hidden sector and its impact on Higgs boson physics at the CERN Large Hadron Collider*,

Phys. Rev. D **72** (2005) 093007.
http://link.aps.org/doi/10.1103/PhysRevD.72.093007.

[28] B. Patt and F. Wilczek, *Higgs-field portal into hidden sectors*, arXiv:hep-ph/0605188 [hep-ph].

[29] G. M. Pruna and T. Robens, *Higgs singlet extension parameter space in the light of the LHC discovery*, Phys. Rev. **D88** (2013) no. 11, 115012, arXiv:1303.1150 [hep-ph].

[30] T. D. Lee, *A theory of spontaneous T violation*, Phys. Rev. D **8** (1973) 1226–1239. http://link.aps.org/doi/10.1103/PhysRevD.8.1226.

[31] ATLAS Collaboration, M. Aaboud et al., *Search for resonances in diphoton events at $\sqrt{s}$=13 TeV with the ATLAS detector*, JHEP **09** (2016) 001, arXiv:1606.03833 [hep-ex].

[32] ATLAS Collaboration, T. A. collaboration, *Search for scalar diphoton resonances with 15.4 fb^{-1} of data collected at $\sqrt{s}$=13 TeV in 2015 and 2016 with the ATLAS detector*, .

[33] Wikipedia, *Standard Model of elementary particles*, https://upload.wikimedia.org/wikipedia/commons/0/00/Standard_Model_of_Elementary_Particles.svg, 2006. [Online; accessed 17-October-2016].

[34] C. N. Yang and R. L. Mills, *Conservation of isotopic spin and isotopic gauge invariance*, Phys. Rev. **96** (1954) 191–195. http://link.aps.org/doi/10.1103/PhysRev.96.191.

[35] M. Gell-Mann, *A schematic model of baryons and mesons*, Physics Letters **8** (1964) no. 3, 214 – 215. http://www.sciencedirect.com/science/article/pii/S0031916364920013.

[36] G. Zweig, *An SU(3) model for strong interaction symmetry and its breaking. Version 2*, in *DEVELOPMENTS IN THE QUARK THEORY OF HADRONS. VOL. 1. 1964 - 1978*, D. Lichtenberg and S. P. Rosen, eds., pp. 22–101. 1964. http://inspirehep.net/record/4674/files/cern-th-412.pdf.

[37] J. S. Schwinger, *A theory of the fundamental interactions*, Annals Phys. **2** (1957) 407–434.

[38] T. D. Lee and C. N. Yang, *Possible nonlocal effects in μ decay*, Phys. Rev. **108** (1957) 1611–1614. http://link.aps.org/doi/10.1103/PhysRev.108.1611.

[39] UA1 Collaboration, G. Arnison et al., *Experimental observation of isolated large transverse energy electrons with associated missing energy at s**(1/2) = 540-GeV*, Phys. Lett. **B122** (1983) 103–116. [,611(1983)].

[40] UA2 Collaboration, M. Banner et al., *Observation of single isolated electrons of high transverse momentum in events with missing transverse energy at the CERN anti-p p collider*, Phys. Lett. **B122** (1983) 476–485.

[41] UA1 Collaboration, G. Arnison et al., *Experimental observation of lepton pairs of invariant mass around 95-GeV/c**2 at the CERN SPS collider*, Phys. Lett. **B126** (1983) 398–410.

[42] UA2 Collaboration, P. Bagnaia et al., *Evidence for Z0 —¿ e+ e- at the CERN anti-p p collider*, Phys. Lett. **B129** (1983) 130–140.

[43] Y. Nambu, *Quasi-particles and gauge invariance in the theory of superconductivity*, Phys. Rev. **117** (1960) 648–663. http://link.aps.org/doi/10.1103/PhysRev.117.648.

[44] J. Goldstone, *Field theories with superconductor solutions*, Nuovo Cim. **19** (1961) 154–164.

[45] J. Goldstone, A. Salam, and S. Weinberg, *Broken symmetries*, Phys. Rev. **127** (1962) 965–970. http://link.aps.org/doi/10.1103/PhysRev.127.965.

[46] Particle Data Group Collaboration, K. A. Olive et al., *Review of particle physics*, Chin. Phys. **C38** (2014) 090001.

[47] LHC Higgs Cross Section Working Group, S. Dittmaier, C. Mariotti, G. Passarino, and R. Tanaka (Eds.), *Handbook of LHC Higgs cross sections: 1. Inclusive observables*, CERN-2011-002 (CERN, Geneva, 2011) , arXiv:1101.0593 [hep-ph].

[48] LHC Higgs Cross Section Working Group, S. Dittmaier, C. Mariotti, G. Passarino, and R. Tanaka (Eds.), *Handbook of LHC Higgs cross sections: 2.*

Differential distributions, CERN-2012-002 (CERN, Geneva, 2012) , arXiv:1201.3084 [hep-ph].

[49] LHC Higgs Cross Section Working Group Collaboration, J. R. Andersen et al., *Handbook of LHC Higgs cross sections: 3. Higgs properties*, arXiv:1307.1347 [hep-ph].

[50] D. E. De Florian Sabaris, C. Grojean, F. Maltoni, C. Mariotti, A. Nikitenko, M. Pieri, P. Savard, M. Schumacher, and R. Tanaka, *Handbook of LHC Higgs cross sections: 4. Deciphering the nature of the Higgs sector*, . https://cds.cern.ch/record/2215893.

[51] A. D. Martin, W. J. Stirling, R. S. Thorne, and G. Watt, *Parton distributions for the LHC*, Eur. Phys. J. **C63** (2009) 189–285, arXiv:0901.0002 [hep-ph].

[52] H. M. Georgi, S. L. Glashow, M. E. Machacek, and D. V. Nanopoulos, *Higgs bosons from two gluon annihilation in proton- proton collisions*, Phys. Rev. Lett. **40** (1978) 692.

[53] A. Djouadi, M. Spira, and P. Zerwas, *Production of Higgs bosons in proton colliders. QCD corrections*, Physics Letters B **264** (1991) no. 3, 440 – 446. http://www.sciencedirect.com/science/article/pii/037026939190375Z.

[54] S. Dawson, *Radiative corrections to Higgs boson production*, Nuclear Physics B **359** (1991) no. 2, 283 – 300. http://www.sciencedirect.com/science/article/pii/0550321391900612.

[55] M. Spira, A. Djouadi, D. Graudenz, and R. Zerwas, *Higgs boson production at the LHC*, Nuclear Physics B **453** (1995) no. 1, 17 – 82. http://www.sciencedirect.com/science/article/pii/0550321395003797.

[56] R. V. Harlander and W. B. Kilgore, *Next-to-next-to-leading order Higgs production at hadron colliders*, Phys. Rev. Lett. **88** (2002) 201801. http://link.aps.org/doi/10.1103/PhysRevLett.88.201801.

[57] C. Anastasiou and K. Melnikov, *Higgs boson production at hadron colliders in {NNLO} {QCD}*, Nuclear Physics B **646** (2002) no. 12, 220 – 256. http://www.sciencedirect.com/science/article/pii/S0550321302008374.

[58] V. Ravindran, J. Smith, and W. van Neerven, *{NNLO} corrections to the total cross section for Higgs boson production in hadronhadron collisions*, Nuclear Physics B **665** (2003) 325 – 366. http://www.sciencedirect.com/science/article/pii/S0550321303004577.

[59] U. Aglietti, R. Bonciani, G. Degrassi, and A. Vicini, *Two-loop light fermion contribution to Higgs production and decays*, Physics Letters B **595** (2004) no. 14, 432 – 441. http://www.sciencedirect.com/science/article/pii/S0370269304009268.

[60] S. Actis, G. Passarino, C. Sturm, and S. Uccirati, *{NLO} electroweak corrections to Higgs boson production at hadron colliders*, Physics Letters B **670** (2008) no. 1, 12 – 17. http://www.sciencedirect.com/science/article/pii/S0370269308012689.

[61] S. Catani, D. de Florian, M. Grazzini, and P. Nason, *Soft-gluon resummation for Higgs boson production at hadron colliders*, Journal of High Energy Physics **2003** (2003) no. 07, 028. http://stacks.iop.org/1126-6708/2003/i=07/a=028.

[62] C. Anastasiou, R. Boughezal, and F. Petriello, *Mixed QCD-electroweak corrections to Higgs boson production in gluon fusion*, Journal of High Energy Physics **2009** (2009) no. 04, 003. http://stacks.iop.org/1126-6708/2009/i=04/a=003.

[63] D. de Florian and M. Grazzini, *Higgs production at the LHC: updated cross sections at* $\sqrt{s} = 8\ TeV$, Phys. Lett. **B718** (2012) 117–120, arXiv:1206.4133 [hep-ph].

[64] C. Anastasiou, S. Buehler, F. Herzog, and A. Lazopoulos, *Inclusive Higgs boson cross-section for the LHC at 8 TeV*, Journal of High Energy Physics **2012** (2012) no. 4, 4. http://dx.doi.org/10.1007/JHEP04(2012)004.

[65] J. Baglio and A. Djouadi, *Higgs production at the LHC*, Journal of High Energy Physics **2011** (2011) no. 3, 55. http://dx.doi.org/10.1007/JHEP03(2011)055.

[66] R. Cahn and S. Dawson, *Production of very massive Higgs bosons*, Physics Letters B **136** (1984) no. 3, 196 – 200. http://www.sciencedirect.com/science/article/pii/0370269384911808.

[67] M. Ciccolini, A. Denner, and S. Dittmaier, *Strong and electroweak corrections to the production of a Higgs boson* $+ 2$ *jets via weak interactions at the Large*

Hadron Collider, Phys. Rev. Lett. **99** (2007) 161803. http://link.aps.org/doi/10.1103/PhysRevLett.99.161803.

[68] M. Ciccolini, D. A., and D. S., *Electroweak and QCD corrections to Higgs production via vector-boson fusion at the CERN LHC*, Phys. Rev. D **77** (2008) 013002. http://link.aps.org/doi/10.1103/PhysRevD.77.013002.

[69] K. Arnold, M. Bhr, G. Bozzi, F. Campanario, C. Englert, T. Figy, N. Greiner, C. Hackstein, V. Hankele, B. Jger, G. Klmke, M. Kubocz, C. Oleari, S. Pltzer, S. Prestel, M. Worek, and D. Zeppenfeld, *Vbfnlo: A parton level Monte Carlo for processes with electroweak bosons*, Computer Physics Communications **180** (2009) no. 9, 1661 – 1670. http://www.sciencedirect.com/science/article/pii/S0010465509001027.

[70] P. Bolzoni, F. Maltoni, S.-O. Moch, and M. Zaro, *Higgs boson production via vector-boson fusion at next-to-next-to-leading order in QCD*, Phys. Rev. Lett. **105** (2010) 011801. http://link.aps.org/doi/10.1103/PhysRevLett.105.011801.

[71] S. L. Glashow, D. V. Nanopoulos, and A. Yildiz, *Associated production of Higgs bosons and Z particles*, Phys. Rev. D **18** (1978) 1724–1727. http://link.aps.org/doi/10.1103/PhysRevD.18.1724.

[72] T. Han and S. Willenbrock, *QCD correction to the pp WH and ZH total cross sections*, Physics Letters B **273** (1991) no. 1, 167 – 172. http://www.sciencedirect.com/science/article/pii/0370269391905728.

[73] O. Brein, A. Djouadi, and R. Harlander, {*NNLO*} {*QCD*} *corrections to the Higgs-strahlung processes at hadron colliders*, Physics Letters B **579** (2004) no. 12, 149 – 156. http://www.sciencedirect.com/science/article/pii/S0370269303017234.

[74] M. L. Ciccolini, S. Dittmaier, and M. Krämer, *Electroweak radiative corrections to associated WH and ZH production at hadron colliders*, Phys. Rev. D **68** (2003) 073003. http://link.aps.org/doi/10.1103/PhysRevD.68.073003.

[75] Z. Kunszt, *Associated production of heavy Higgs boson with top quarks*, Nuclear Physics B **247** (1984) no. 2, 339 – 359. http://www.sciencedirect.com/science/article/pii/0550321384905534.

[76] W. Beenakker, S. Dittmaier, M. Krämer, B. Plümper, M. Spira, and P. M. Zerwas, *Higgs radiation off top quarks at the Tevatron and the LHC*, Phys. Rev. Lett. **87** (2001) 201805. http://link.aps.org/doi/10.1103/PhysRevLett.87.201805.

[77] W. Beenakker, S. Dittmaier, M. Krmer, B. Plmper, M. Spira, and P. Zerwas, {*NLO*} {*QCD*} *corrections to ttH production in hadron collisions*, Nuclear Physics B **653** (2003) no. 12, 151 – 203. http://www.sciencedirect.com/science/article/pii/S0550321303000440.

[78] S. Dawson, L. H. Orr, L. Reina, and D. Wackeroth, *Next-to-leading order QCD corrections to* $p \overrightarrow{p} \to t\bar{t}h$ *at the CERN Large Hadron Collider*, Phys. Rev. D **67** (2003) 071503. http://link.aps.org/doi/10.1103/PhysRevD.67.071503.

[79] S. Dawson, C. Jackson, L. H. Orr, L. Reina, and D. Wackeroth, *Associated Higgs boson production with top quarks at the CERN Large Hadron Collider: NLO QCD corrections*, Phys. Rev. D **68** (2003) 034022. http://link.aps.org/doi/10.1103/PhysRevD.68.034022.

[80] L. J. Dixon and M. S. Siu, *Resonance continuum interference in the diphoton Higgs signal at the LHC*, Phys. Rev. Lett. **90** (2003) 252001, arXiv:hep-ph/0302233 [hep-ph].

[81] A. Djouadi, J. Kalinowski, and M. Spira, *HDECAY: a program for Higgs boson decays in the Standard Model and its supersymmetric extension*, Computer Physics Communications **108** (1998) no. 1, 56 – 74. http://www.sciencedirect.com/science/article/pii/S0010465597001239.

[82] J. R. Ellis, M. K. Gaillard, and D. V. Nanopoulos, *A phenomenological profile of the Higgs boson*, Nucl. Phys. B **106** (1976) no. CERN-TH-2093. 2, 292–340. 64 p. https://cds.cern.ch/record/874049.

[83] B. W. Lee, C. Quigg, and H. B. Thacker, *Weak interactions at very high-energies: the role of the Higgs boson mass*, Phys. Rev. **D16** (1977) 1519.

[84] B. W. Lee, C. Quigg, and H. B. Thacker, *The strength of weak interactions at very high-energies and the Higgs boson mass*, Phys. Rev. Lett. **38** (1977) 883–885.

[85] T. Binoth, J. P. Guillet, E. Pilon, and M. Werlen, *A full next-to-leading order study of direct photon pair production in hadronic collisions*, Eur. Phys. J. **C16** (2000) 311–330, arXiv:hep-ph/9911340 [hep-ph].

[86] J. M. Campbell, R. K. Ellis, Y. Li, and C. Williams, *Predictions for diphoton production at the LHC through NNLO in QCD*, JHEP **07** (2016) 148, arXiv:1603.02663 [hep-ph].

[87] T. Binoth, J. P. Guillet, E. Pilon, and M. Werlen, *A next-to-leading order study of pion pair production and comparison with E706 data*, Eur. Phys. J. **C24** (2002) 245–260, arXiv:hep-ph/0111043 [hep-ph].

[88] T. Binoth, J. P. Guillet, E. Pilon, and M. Werlen, *A next-to-leading order study of photon pion and pion pair hadro production in the light of the Higgs boson search at the LHC*, Eur. Phys. J.direct **C4** (2002) 7, arXiv:hep-ph/0203064 [hep-ph].

[89] T. Sjostrand, S. Mrenna, and P. Z. Skands, *PYTHIA 6.4 physics and manual*, JHEP **05** (2006) 026, arXiv:hep-ph/0603175 [hep-ph].

[90] ATLAS Collaboration, *ATLAS magnet system: technical design report, 1.* Technical Design Report ATLAS. CERN, Geneva, 1997. http://cds.cern.ch/record/338080.

[91] ATLAS Collaboration, *ATLAS central solenoid: technical design report.* Technical Design Report ATLAS. CERN, Geneva, 1997. http://cds.cern.ch/record/331067. Electronic version not available.

[92] ATLAS Collaboration, J. P. Badiou, J. Beltramelli, J. M. Baze, and J. Belorgey, *ATLAS barrel toroid: technical design report.* Technical Design Report ATLAS. CERN, Geneva, 1997. http://cds.cern.ch/record/331065. Electronic version not available.

[93] ATLAS Collaboration, *ATLAS end-cap toroids: technical design report.* Technical Design Report ATLAS. CERN, Geneva, 1997. http://cds.cern.ch/record/331066. Electronic version not available.

[94] ATLAS Collaboration, G. Aad and other, *ATLAS pixel detector electronics and sensors*, Journal of Instrumentation **3** (2008) no. 07, P07007. http://stacks.iop.org/1748-0221/3/i=07/a=P07007.

[95] A. Ahmad et al., *The silicon microstrip sensors of the ATLAS semiconductor tracker*, Nuclear Instruments and Methods in Physics Research Section A: Accelerators, Spectrometers, Detectors and Associated Equipment **578** (2007) no. 1, 98 – 118. http://www.sciencedirect.com/science/article/pii/S0168900207007644.

[96] ATLAS TRT Collaboration, E. Abat et al., *The ATLAS Transition Radiation Tracker (TRT) proportional drift tube: design and performance*, Journal of Instrumentation **3** (2008) no. 02, P02013. http://stacks.iop.org/1748-0221/3/i=02/a=P02013.

[97] ATLAS Collaboration, *ATLAS liquid-argon calorimeter: technical design report.* Technical Design Report ATLAS. CERN, Geneva, 1996. http://cds.cern.ch/record/331061.

[98] ATLAS Collaboration, *ATLAS tile calorimeter: technical design report.* Technical Design Report ATLAS. CERN, Geneva, 1996. http://cds.cern.ch/record/331062.

[99] S. Palestini, *The muon spectrometer of the ATLAS experiment*, Nuclear Physics B - Proceedings Supplements **125** (2003) 337 – 345. http://www.sciencedirect.com/science/article/pii/S0920563203910139.

[100] ATLAS Collaboration, G. Aad et al., *Improved luminosity determination in pp collisions at sqrt(s) = 7 TeV using the ATLAS detector at the LHC*, Eur. Phys. J. **C73** (2013) no. 8, 2518, arXiv:1302.4393 [hep-ex].

[101] S. Alioli, P. Nason, C. Oleari, and E. Re, *NLO Higgs boson production via gluon fusion matched with shower in POWHEG*, JHEP **04** (2009) 002, arXiv:0812.0578 [hep-ph].

[102] P. Nason and C. Oleari, *NLO Higgs boson production via vector-boson fusion matched with shower in POWHEG*, JHEP **02** (2010) 037, arXiv:0911.5299 [hep-ph].

[103] T. Sjostrand, S. Mrenna, and P. Z. Skands, *A brief introduction to PYTHIA 8.1*, Comput. Phys. Commun. **178** (2008) 852–867, arXiv:0710.3820 [hep-ph].

[104] GEANT4 Collaboration, S. Agostinelli et al., *GEANT4: a simulation toolkit*, Nucl. Instrum. Meth. **A506** (2003) 250–303.

[105] ATLAS Collaboration, G. Aad et al., *The ATLAS simulation infrastructure*, Eur. Phys. J. **C70** (2010) 823–874, arXiv:1005.4568 [physics.ins-det].

[106] J. Alwall, R. Frederix, S. Frixione, V. Hirschi, F. Maltoni, O. Mattelaer, H. S. Shao, T. Stelzer, P. Torrielli, and M. Zaro, *The automated computation of*

tree-level and next-to-leading order differential cross sections, and their matching to parton shower simulations, JHEP **07** (2014) 079, arXiv:1405.0301 [hep-ph].

[107] NNPDF Collaboration, R. D. Ball et al., *Parton distributions for the LHC Run II*, JHEP **04** (2015) 040, arXiv:1410.8849 [hep-ph].

[108] *ATLAS Run 1 Pythia8 tunes*, Tech. Rep. ATL-PHYS-PUB-2014-021, CERN, Geneva, 2014. http://cds.cern.ch/record/1966419.

[109] T. Gleisberg, S. Hoeche, F. Krauss, M. Schonherr, S. Schumann, F. Siegert, and J. Winter, *Event generation with SHERPA 1.1*, JHEP **02** (2009) 007, arXiv:0811.4622 [hep-ph].

[110] C. Balazs, E. L. Berger, P. M. Nadolsky, and C. P. Yuan, *Calculation of prompt diphoton production cross-sections at Tevatron and LHC energies*, Phys. Rev. **D76** (2007) 013009, arXiv:0704.0001 [hep-ph].

[111] M. L. Mangano, M. Moretti, F. Piccinini, R. Pittau, and A. D. Polosa, *ALPGEN, a generator for hard multiparton processes in hadronic collisions*, JHEP **07** (2003) 001, arXiv:hep-ph/0206293 [hep-ph].

[112] S. Schumann and F. Krauss, *A Parton shower algorithm based on Catani-Seymour dipole factorisation*, JHEP **03** (2008) 038, arXiv:0709.1027 [hep-ph].

[113] S. Hoeche, F. Krauss, S. Schumann, and F. Siegert, *QCD matrix elements and truncated showers*, JHEP **05** (2009) 053, arXiv:0903.1219 [hep-ph].

[114] H.-L. Lai, M. Guzzi, J. Huston, Z. Li, P. M. Nadolsky, J. Pumplin, and C. P. Yuan, *New parton distributions for collider physics*, Phys. Rev. **D82** (2010) 074024, arXiv:1007.2241 [hep-ph].

[115] ATLAS Collaboration, G. Aad et al., *Electron reconstruction and identification efficiency measurements with the ATLAS detector using the 2011 LHC proton-proton collision data*, Eur. Phys. J. **C74** (2014) no. 7, 2941, arXiv:1404.2240 [hep-ex].

[116] ATLAS Collaboration, G. Aad et al., *Measurement of the muon reconstruction performance of the ATLAS detector using 2011 and 2012 LHC protonproton collision data*, Eur. Phys. J. **C74** (2014) no. 11, 3130, arXiv:1407.3935 [hep-ex].

[117] ATLAS Collaboration, *Commissioning of the ATLAS high-performance b-tagging algorithms in the 7 TeV collision data*, Tech. Rep. ATLAS-CONF-2011-102, CERN, Geneva, 2011. http://cds.cern.ch/record/1369219.

[118] ATLAS Collaboration, *Calibration of the performance of b-tagging for c and light-flavour jets in the 2012 ATLAS data*, Tech. Rep. ATLAS-CONF-2014-046, CERN, Geneva, 2014. http://cds.cern.ch/record/1741020.

[119] ATLAS Collaboration, *Performance of missing transverse momentum reconstruction in ATLAS with 2011 proton-proton collisions at sqrts = 7 TeV*, Tech. Rep. ATLAS-CONF-2012-101, CERN, Geneva, 2012. http://cds.cern.ch/record/1463915.

[120] ATLAS Collaboration, *Performance of missing transverse momentum reconstruction in ATLAS studied in proton-proton collisions recorded in 2012 at 8 TeV*, Tech. Rep. ATLAS-CONF-2013-082, CERN, Geneva, 2013. http://cds.cern.ch/record/1570993.

[121] W. Lampl, S. Laplace, D. Lelas, P. Loch, H. Ma, S. Menke, S. Rajagopalan, D. Rousseau, S. Snyder, and G. Unal, *Calorimeter clustering algorithms: description and performance*, Tech. Rep. ATL-LARG-PUB-2008-002. ATL-COM-LARG-2008-003, CERN, Geneva, 2008. http://cds.cern.ch/record/1099735.

[122] *Expected photon performance in the ATLAS experiment*, Tech. Rep. ATL-PHYS-PUB-2011-007, CERN, Geneva, 2011. https://cds.cern.ch/record/1345329.

[123] ATLAS Collaboration, M. Aaboud et al., *Measurement of the photon identification efficiencies with the ATLAS detector using LHC Run-1 data*, arXiv:1606.01813 [hep-ex].

[124] ATLAS Collaboration, G. Aad et al., *Electron and photon energy calibration with the ATLAS detector using LHC Run 1 data*, Eur. Phys. J. **C74** (2014) no. 10, 3071, arXiv:1407.5063 [hep-ex].

[125] ATLAS Collaboration, *Electron and photon energy calibration with the ATLAS detector using data collected in 2015 at* $\sqrt{s} = 13$ TeV, Tech. Rep. ATL-PHYS-PUB-2016-015, CERN, Geneva, 2016. http://cds.cern.ch/record/2203514.

[126] ATLAS Collaboration, G. Aad et al., *Electron performance measurements with the ATLAS detector using the 2010 LHC proton-proton collision data*, Eur. Phys. J. **C72** (2012) 1909, arXiv:1110.3174 [hep-ex].

[127] ATLAS Collaboration, *Photon identification in 2015 ATLAS data*, Tech. Rep. ATL-PHYS-PUB-2016-014, CERN, Geneva, 2016. http://cds.cern.ch/record/2203125.

[128] ATLAS Collaboration, G. Aad et al., *Expected performance of the ATLAS experiment - detector, trigger and physics*, arXiv:0901.0512 [hep-ex].

[129] S. D. Ellis and D. E. Soper, *Successive combination jet algorithm for hadron collisions*, Phys. Rev. **D48** (1993) 3160–3166, arXiv:hep-ph/9305266 [hep-ph].

[130] S. Catani, Y. L. Dokshitzer, M. H. Seymour, and B. R. Webber, *Longitudinally invariant K_t clustering algorithms for hadron hadron collisions*, Nucl. Phys. **B406** (1993) 187–224.

[131] ATLAS Collaboration, G. Aad et al., *Measurement of the inclusive isolated prompt photon cross section in pp collisions at $\sqrt{s} = 7$ TeV with the ATLAS detector*, Phys. Rev. **D83** (2011) 052005, arXiv:1012.4389 [hep-ex].

[132] M. Cacciari, G. P. Salam, and G. Soyez, *The anti-k(t) jet clustering algorithm*, JHEP **04** (2008) 063, arXiv:0802.1189 [hep-ph].

[133] ATLAS Liquid Argon EMEC/HEC Collaboration, C. Cojocaru et al., *Hadronic calibration of the ATLAS liquid argon end-cap calorimeter in the*

pseudorapidity region 1.6 ¡ —η— ¡ 1.8 in beam tests, Nucl. Instrum. Meth. **A531** (2004) 481–514, arXiv:physics/0407009 [physics].

[134] ATLAS Collaboration, G. Aad et al., *Jet energy measurement with the ATLAS detector in proton-proton collisions at* $\sqrt{s} = 7$ *TeV*, Eur. Phys. J. **C73** (2013) no. 3, 2304, arXiv:1112.6426 [hep-ex].

[135] ATLAS Collaboration, *Pile-up corrections for jets from proton-proton collisions at* $\sqrt{s} = 7$ *TeV in ATLAS in 2011*, Tech. Rep. ATLAS-CONF-2012-064, CERN, Geneva, 2012. https://cds.cern.ch/record/1459529.

[136] *Pile-up subtraction and suppression for jets in ATLAS*, Tech. Rep. ATLAS-CONF-2013-083, CERN, Geneva, 2013. http://cds.cern.ch/record/1570994.

[137] ATLAS Collaboration, G. Aad et al., *Performance of the ATLAS trigger system in 2010*, Eur. Phys. J. **C72** (2012) 1849, arXiv:1110.1530 [hep-ex].

[138] H. Wang, *Discovery of a new boson in the search for a Standard Model Higgs boson in the diphoton final state with the ATLAS detector*. PhD thesis, Wisconsin U., Madison, 2013-07-31. http://inspirehep.net/record/1296455/files/113883825_CERN-THESIS-2013-201.pdf.

[139] G. Cowan, K. Cranmer, E. Gross, and O. Vitells, *Asymptotic formulae for likelihood-based tests of new physics*, Eur. Phys. J. **C71** (2011) 1554, arXiv:1007.1727 [physics.data-an]. [Erratum: Eur. Phys. J.C73,2501(2013)].

[140] M. Vesterinen and T. R. Wyatt, *A novel technique for studying the Z boson transverse momentum distribution at hadron colliders*, Nucl. Instrum. Meth. **A602** (2009) 432–437, arXiv:0807.4956 [hep-ex].

[141] M. Oreglia, *A study of the reactions* $\psi' \to \gamma\gamma\psi$. PhD thesis, SLAC, 1980. http://www-public.slac.stanford.edu/sciDoc/docMeta.aspx?slacPubNumber=slac-r-236.html.

[142] ATLAS Collaboration, G. Aad et al., *Search for scalar diphoton resonances in the mass range* $65 - 600$ *GeV with the ATLAS detector in pp collision data at* $\sqrt{s} = 8\,TeV$, Phys. Rev. Lett. **113** (2014) no. 17, 171801, arXiv:1407.6583 [hep-ex].

[143] P. Artoisenet et al., *A framework for Higgs characterisation*, JHEP **11** (2013) 043, arXiv:1306.6464 [hep-ph].

[144] R. D. Ball, V. Bertone, F. Cerutti, L. Del Debbio, S. Forte, A. Guffanti, J. I. Latorre, J. Rojo, and M. Ubiali, *Impact of heavy quark masses on parton distributions and LHC phenomenology*, Nucl. Phys. **B849** (2011) 296–363, arXiv:1101.1300 [hep-ph].

[145] A. Denner, S. Heinemeyer, I. Puljak, D. Rebuzzi, and M. Spira, *Standard Model Higgs-boson branching ratios with uncertainties*, Eur. Phys. J. **C71** (2011) 1753, arXiv:1107.5909 [hep-ph].

[146] I. W. Stewart and F. J. Tackmann, *Theory uncertainties for Higgs and other searches using jet bins*, Phys. Rev. **D85** (2012) 034011, arXiv:1107.2117 [hep-ph].

[147] J. M. Campbell, R. K. Ellis, and C. Williams, *Hadronic production of a Higgs boson and two jets at next-to-leading order*, Phys. Rev. **D81** (2010) 074023, arXiv:1001.4495 [hep-ph].

[148] ATLAS Collaboration, *ATLAS tunes of PYTHIA 6 and Pythia 8 for MC11*, .

[149] ATLAS Collaboration, G. Aad et al., *Search for the Standard Model Higgs boson in the two photon decay channel with the ATLAS detector at the LHC*, Phys. Lett. **B705** (2011) 452–470, arXiv:1108.5895 [hep-ex].

[150] ATLAS Collaboration, G. Aad et al., *Measurement of the isolated di-photon cross-section in pp collisions at $\sqrt{s} = 7$ TeV with the ATLAS detector*, Phys. Rev. **D85** (2012) 012003, arXiv:1107.0581 [hep-ex].

[151] ATLAS Collaboration, G. Aad et al., *Measurement of isolated-photon pair production in pp collisions at $\sqrt{s} = 7$ TeV with the ATLAS detector*, JHEP **01** (2013) 086, arXiv:1211.1913 [hep-ex].

[152] CDF Collaboration, T. Aaltonen et al., *Search for new particles decaying into dijets in proton-antiproton collisions at s**(1/2) = 1.96-TeV*, Phys. Rev. **D79** (2009) 112002, arXiv:0812.4036 [hep-ex].

[153] *Procedure for the LHC Higgs boson search combination in summer 2011*, Tech. Rep. ATL-PHYS-PUB-2011-011, CERN, Geneva, 2011. https://cds.cern.ch/record/1375842.

[154] W. Verkerke and D. P. Kirkby, *The RooFit toolkit for data modeling*, eConf **C0303241** (2003) MOLT007, arXiv:physics/0306116 [physics]. [,186(2003)].

[155] R. Brun and F. Rademakers, $\{ROOT\}$ *An object oriented data analysis framework*, Nuclear Instruments and Methods in Physics Research Section A: Accelerators, Spectrometers, Detectors and Associated Equipment **389** (1997) no. 12, 81 – 86. http://www.sciencedirect.com/science/article/pii/S016890029700048X. New Computing Techniques in Physics Research V.

[156] L. Moneta, K. Belasco, K. S. Cranmer, S. Kreiss, A. Lazzaro, D. Piparo, G. Schott, W. Verkerke, and M. Wolf, *The RooStats project*, PoS **ACAT2010** (2010) 057, arXiv:1009.1003 [physics.data-an].

[157] A. L. Read, *Modified frequentist analysis of search results (the CL_s method)*, . https://cds.cern.ch/record/451614.

[158] A. L. Read, *Presentation of search results: the CL(s) technique*, J. Phys. **G28** (2002) 2693–2704. [,11(2002)].

[159] ATLAS Collaboration, G. Aad et al., *Combined search for the Standard Model Higgs boson in pp collisions at $\sqrt{s}$=7 TeV with the ATLAS detector*, Phys. Rev. D **86** (2012) 032003. http://link.aps.org/doi/10.1103/PhysRevD.86.032003.

[160] S. S. Wilks, *The large-sample distribution of the likelihood ratio for testing composite hypotheses*, Annals Math. Statist. **9** (1938) no. 1, 60–62.

[161] A. Wald, *Tests of statistical hypotheses concerning several parameters when the number of observations is large*, Transactions of the American Mathematical Society **54** (1943) no. 3, 426–482. http://www.jstor.org/stable/1990256.

[162] E. Gross and O. Vitells, *Trial factors for the look elsewhere effect in high energy physics*, Eur. Phys. J. **C70** (2010) 525–530, arXiv:1005.1891 [physics.data-an].

[163] O. Vitells and E. Gross, *Estimating the significance of a signal in a multi-dimensional search*, Astroparticle Physics **35** (2011) 230–234, arXiv:1105.4355 [astro-ph.IM].